On the Dynamics of Flat Plates in a Fluid Environment: A Study of Inverted Flag Flapping and Caudal Fin Maneuvering

Thesis by

Cecilia Huertas-Cerdeira

In Partial Fulfillment of the Requirements for the
Degree of
Doctor of Philosophy

Caltech

CALIFORNIA INSTITUTE OF TECHNOLOGY
Pasadena, California

2019
Defended May 31, 2019

Cecilia Huertas-Cerdeira
ORCID: 0000-0003-4553-0470

ACKNOWLEDGEMENTS

The completion of this thesis would not have been possible without the help and support of many individuals. I am indebted to my advisor, Prof. Mory Gharib, for providing invaluable guidance, direction and encouragement throughout my years at the Institute. I am extremely thankful to Prof. John Sader for his enthusiastic collaboration in Part I of this thesis as well as for the many enlightening discussions that have resulted. I would like to extend my gratitude to the members of my thesis committee, Prof. Tim Colonius, Prof. Beverley McKeon and Prof. Dale Pullin for their careful review and feedback of this work.

The Gharib group members, past and present, have been a constant source of assistance and advice, be it in aiding with my experimental setups, offering their diverse expertise or sharing their scientific perspective. I would like to especially acknowledge Julia Cossé, who mentored my first experience at Caltech as a summer undergraduate researcher, and Nathan Martin, who developed the experimental setup that was employed in Part II of this thesis.

I would like to thank those past mentors and teachers who introduced me to the world of scientific research and encouraged me to advance my scientific career. I am grateful for having enjoyed my time at Caltech with a fantastic group of colleagues and friends that have shared problem sets and adventures alike. The fond memories of the past years will last a lifetime.

Finally, I would not have been able to accomplish this work without the unwavering support from family and friends, who have encouraged me throughout this enterprise and brightened even the most challenging of my days. To all of you who have been by my side despite the thousands of miles between us, thank you.

The author of this thesis has received financial support from the La Caixa Fellowship Grant for Post-graduate Studies and the Victoria Alegria Tracy Scholarship. Funding for this research was provided through the Moore Foundation, the National Science Foundation and the Center for Autonomous Systems and Technologies at Caltech.

ABSTRACT

Despite serving analogous functions, the mechanical designs conceived by human engineering and those that result from natural evolution often possess fundamentally differing properties. This thesis explores the use of principles that stem from natural evolution to improve the performance of engineered mechanisms, focusing on systems whose role is to interact with a fluid environment. Two different principles are considered: the use of compliance, abundant in nature's structures, and the use of flapping propulsion, prevalent among nature's swimmers.

The first part of this thesis is dedicated to investigating the physics that govern the behavior of an inverted-flag energy harvester; an unactuated flexible cantilever plate that is clamped at its trailing edge and submerged in a flow. The resonance between solid motion and fluid forcing generates large-amplitude unsteady deformations of the structure that may be used for energy harvesting purposes. The effect of the flag's aspect ratio on its stability is first evaluated. Flags of very small aspect ratio are demonstrated to undergo a saddle-node bifurcation instead of a divergence instability. The angle of attack of the flag is then modified to reveal the existence of dynamical regimes additional to those present at zero angle of attack. A side-by-side flag configuration is finally explored, highlighting the presence of an energetically favorable symmetric flapping mode among other coupled dynamics.

The second part of this thesis delves into the analysis of underwater flapping propellers and the optimization of their three-dimensional motion to generate desired maneuvering forces, with the objective of obtaining an appendage for use in autonomous underwater vehicles that can perform both fast maneuvering and efficient propulsion. An experimental optimization procedure is employed to obtain the most efficient trajectory that generates a specified side force. The effect of increasing the fin's aspect ratio is examined, and a highly efficient trajectory, that makes use of high three-dimensionality and rotation angles, is obtained for a fin of AR=4. The use of a flexible fin is then analyzed and shown to be detrimental to the maneuvering efficiency of the system.

PUBLISHED CONTENT AND CONTRIBUTIONS

John E Sader, Cecilia Huertas-Cerdeira, and Morteza Gharib. Stability of slender inverted flags and rods in a uniform steady flow. *Journal of Fluid Mechanics* 809:873–894, 2016. DOI: 10.1017/jfm.2016.691
C.H.C. Designed and performed the experimental measurements, analyzed the data and wrote the corresponding section.

Cecilia Huertas-Cerdeira, Boyu Fan, and Morteza Gharib. Coupled motion of two side-by-side inverted flags. *Journal of Fluids and Structures* 46:527–535, 2018. DOI: 10.1016/j.jfluidstructs.2017.11.005
C.H.C Performed the experimental measurements, analyzed the data and wrote the manuscript.

Boyu Fan, Cecilia Huertas-Cerdeira, Julia Cossé, John E. Sader, and Morteza Gharib. Effect of morphology on the large-amplitude flapping dynamics of an inverted flag in a uniform flow. *Journal of Fluid Mechanics* Accepted for publication.
C.H.C performed the vortex lattice method simulations and participated in the discussion.

TABLE OF CONTENTS

LIST OF ILLUSTRATIONS

LIST OF TABLES

PREFACE

> *"Natural and human technologies differ extensively and pervasively. We build dry and stiff structures; nature mostly makes hers wet and flexible. We build of metals; nature never does. Our hinges mainly slide; hers mostly bend. We do wonders with wheels and rotary motion; nature makes fully competent boats, aircraft and terrestrial vehicles that lack them entirely."*
>
> — Steven Vogel, *Cat's Paws and Catapults*

As has been eloquently highlighted by Vogel, the mechanical and structural designs conceived by human engineering and those that result from natural evolution possess, more often than not, fundamentally differing properties. Throughout millions of years of evolution, nature has selected exceptionally efficient tools for an equally extraordinary diversity of requirements; a natural equivalent can be found for almost every human necessity. The aim of this thesis is to explore the use of principles that stem from natural evolution to enhance the performance of engineered mechanisms, focusing on systems whose role is to interact with a fluid environment. The contrast between bio-inspired and bio-mimetic approaches should be emphasized; the purpose of this work is not to merely replicate nature's mechanisms, nor are they considered as an optimized unimprovable solution. Rather, its intent is to combine principles from nature's operation with an engineering foundation to ideate an overall improved design.

Among the differences between natural and human designs, perhaps the most remarkable lies in the disparate use of materials. Engineers commonly employ metals and other stiff constituents, which are difficult to deform and simpler to design. Nature, on the other hand, tends to fashion more flexible materials, using the added complexity to its advantage. Flexibility plays an important role in practically every natural design and is the primary driving principle in countless of its mechanisms. The effect of compliance on a structure is particularly notable when it is subjected to fluid forces from its environment. The aero- and hydrodynamic forces that act on a body submerged in a fluid are dependent both on the body's shape and its motion. In the case of a flexible structure both of these properties are a function of its deformation, which is, in turn, dependent on the fluid forces that are exerted on the structure. This interdependence results in coupled physics between solid deformation and fluid mechanics, which can no longer be considered separately. The field concerned with the study of this coupled behavior is aptly called the field of solid-fluid interactions, and will be the subject of Part I of this thesis. The interactions between solid and fluid add a level of complexity that may be detrimental to the mechanical system, increasing the number of possible failure modes of the structure. They also provide, however, additional degrees of freedom to tinker with that may be exploited to our advantage with careful design. Inspired by the flutter of leaves in the wind, Part I of this thesis is dedicated to the analysis of an inverted flag, a flexible cantilevered plate clamped at its trailing edge that is unactuated but subjected to a uniform flow. The resonance between solid motion and fluid forcing generates large amplitude unsteady deformations that may be used for energy harvesting purposes.

Part II of this thesis draws inspiration from a different natural design. Due to the suitability of metallic components and electromagnetic motors, engineered propellers for aquatic locomotion generally make use of continuous rotational motions. Nature, however, generates propulsive forces through flapping, paddling and jetting. Flapping propulsion is achieved through periodic motions of a plate-type propeller and commonly entails the coupling of lift and thrust forces. This coupling results in complex physics, but eliminates the need of multiple force-generating surfaces. Based on the caudal fin of fish, Part II of this thesis aims to combine both flapping propulsion and the large, although not continuous, rotations of human propellers. A fin capable of generating rotations in three degrees of freedom is proposed as a combined propulsive and maneuvering system for use in autonomous underwater vehicles. The analysis delves into the optimization of the three-dimensional motion to be followed by the fin in order to generate desired maneuvering forces.

In accordance with these two distinct topics, this thesis is divided into two independent parts, with this preface serving as a reminder of the underlying encompassing topic and the origin of the principles at hand.

Part I

Inverted Flags

Chapter 1

INTRODUCTION

The past decades have seen enormous advances in the fields of microelectronics, micro mechanics and wireless communications. With these advances have emerged a new array of low-power devices that function in hard-to-reach locations; examples are remote sensors and monitors, medical implants and wireless actuators. Due to the difficulty of accessing these devices' location, introducing power cables is impractical and periodically replacing their batteries poses significant challenges. A strong emphasis has been put into the development of systems that can harvest small amounts of energy from on-site natural resources (Elvin and Erturk, 2013; Lee et al., 2015; Mateu and Moll, 2005; Paradiso and Starner, 2005; Park and Chou, 2006; Weimer et al., 2006). These systems would allow the devices' continuous operation without the need of accessing their location. A promising line of work is the exploitation of ambient vibrations to generate strains in a piezoelectric material, which can, in turn, convert these strains into electric energy (Ahmed et al., 2017; Liu et al., 2018; Priya, 2007; Sodano et al., 2004). In many cases, a reliable source of vibrations is a surrounding flow. Since the early work of Allen and Smits (2001) and Taylor et al. (2001), substantial amounts of research have focused on the flapping motion of flags as a source of vibration for piezoelectric energy harvesters.

The study of the solid-fluid interactions that develop when a flag is immersed in a uniform wind dates back to the work of Rayleigh (1878). Although many theoretical analyses shortly followed, the first experimental investigation of a flapping flag was performed by Taneda (1968). The problem was revisited by Zhang et al. (2000), and many more studies — theoretical, numerical and experimental — have emerged in recent years. Comprehensive reviews of the recent developments can be found at Yu et al. (2019), Shelley and Zhang (2011), Eloy et al. (2008) and Païdoussis (1998). The dynamics of a flag immersed in a uniform flow can be divided into three separate regimes. At low flow speeds, the flag remains at rest and aligned with the flow in what has been denominated the stretched-straight state. In this state, a thin vortex street of alternating signs trails the flag's trailing edge. At a critical velocity, the stability of the stretched-straight mode is lost through flutter and the flag enters a periodic flapping mode. In this regime, the vortex sheet that is shed is comprised of vortices of a single sign, with the sign alternating each half stroke of the flag.

A bi-stable region has been reported, where both stretched-straight and periodic flapping regimes co-exist. As wind speed is further increased the power spectrum of the flag's motion becomes broadband and the flag enters a chaotic flapping mode.

Because the bending stiffness of piezoelectric panels is substantially larger than that of a cloth flag, the piezoelectric flag is analogous to a cantilever plate, and the critical velocity at which the flapping motion is onset is relatively high. One common remedy to this problem is the placement of an upstream bluff body whose vortex street induces vibrations on the flag (Taylor et al., 2001). In Kim et al. (2013) we followed a different approach and proposed an alternate configuration, the inverted flag, where the leading edge of the cantilever is free to move and the trailing edge is clamped. This configuration is unstable at low flow velocities, making it a good candidate for piezoelectric energy harvesters. Additionally, the maximum flapping amplitude of the inverted flag is approximately 1.7 times its length, which is several times higher than the maximum flapping amplitude reported for regular flags. The higher amplitudes impose significantly higher strains on the piezoelectric material, which may increase up to ten times the energy harvesting efficiency of the system (Gurugubelli and Jaiman, 2015).

The inverted flag presents three main dynamical regimes as a function of free stream velocity. They are represented in figure 1.1, where each image has been obtained by superimposing snapshots of the flag's motion. At low velocities, the flag undergoes small amplitude oscillations around the undeflected position in the denominated straight regime. During these oscillations the flow remains attached (Goza et al., 2018; Gurugubelli and Jaiman, 2015). As the flow speed is increased, it reaches a critical value at which the flag becomes unstable, undergoing a large amplitude flapping motion. The shedding frequency of vortex structures is correlated to this flapping motion, with a variety of vortex patterns occurring for different velocities (Goza et al., 2018; Gurugubelli and Jaiman, 2015; Kim et al., 2013; Ryu et al., 2015; Shoele and Mittal, 2016). If the wind speed is further increased, the inverted flag enters the deflected regime, where it oscillates with small amplitude around a high deflection equilibrium. Bi-stable regions are present both in the transition from straight to flapping and from flapping to deflected regimes.

In addition to these three main regimes, Sader et al. (2016a) reported the existence of a chaotic mode, where the flag flaps aperiodically with a broad frequency spectrum, between the periodic flapping and deflected regimes. Numerical studies, which correspond to low Reynolds number flows, have reported additional dynamical

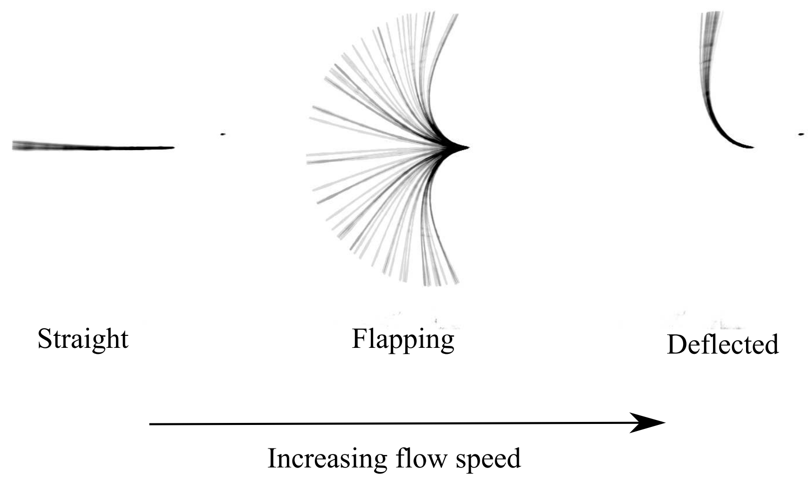

Figure 1.1: Superimposed images of the motion of the inverted flag for the three main dynamical regimes. The flow is left to right and the flags are clamped at their trailing edge.

modes. Ryu et al. (2015) observed the existence of both a small-deflection steady state and a small-deflection small-amplitude flapping regime at flow speeds between those corresponding to the straight and large amplitude flapping regimes. Similar observations have been made by Gurugubelli and Jaiman (2015) and Goza et al. (2018). Gurugubelli and Jaiman (2015) additionally observed a flipped flapping regime at wind speeds higher than those of the deflected regime. In this mode, that has also been observed by Shoele and Mittal (2016) and Tang et al. (2015), the flag bends 180° such that the leading edge is parallel to the flow, recovering a motion similar to that of the conventional flag. Overall, the regimes of motion that have been reported for the inverted flag are, ordered from lowest to highest corresponding flow velocity: straight, small-deflection steady, small-deflection small-amplitude flapping, large amplitude flapping, chaotic, deflected and flipped flapping.

In an attempt to understand the onset of the large amplitude flapping motion, several studies have investigated the loss of stability of the straight regime. While the existence of a divergence instability was hinted by Kim et al. (2013), Gurugubelli and Jaiman (2015) was the first to numerically demonstrate its presence. Sader et al. (2016a) theoretically corroborated the loss of stability of the straight regime through divergence, and provided a simplified analytic formula that reasonably predicts the onset of flapping for inverted flags of aspect ratios higher than 1.

Using a scaling analysis, Sader et al. (2016a) further proved that the flag's flapping motion constitutes a vortex induced vibration. Goza et al. (2018) associated this classic vortex induced vibration with the 2P vortex shedding mode, and linked the appearance of additional shedding modes at higher flow velocities with the breakdown of the VIV and appearance of chaos. The cessation of flapping has received comparably little attention, and is not yet fully understood. Goza et al. (2018) suggested the mechanism behind this transition to be a disruption of lock-on caused by the increased disparity between natural and shedding frequencies of the flag. While the transition velocity from straight to flapping regimes is independent of mass ratio, as defined in Section 1.2, the transition velocity from flapping to deflected regimes decreases as the fluid loading, and therefore damping, increases (Kim et al., 2013), consistent with the lock-off theory.

The results summarized in this section have been obtained for flags with relatively heavy fluid loading; a distinction should be made for flags with light fluid loading. Although these flags still present a flapping mode, this motion does not constitute a vortex induced vibration (Goza et al., 2018). Due to the small thickness of the flag, however, inverted flags are subject to heavy fluid loading for all practical cases.

1.1 Objectives

As has been highlighted above, since it was first introduced in Kim et al. (2013), many advances have been made towards the understanding of the inverted flag's mechanics. However, several aspects that are fundamental for its full characterization are yet to be investigated. The objective of this thesis is to address the most salient of these topics. In many cases, the field has evolved in parallel to the development of this work; recent advances have been addressed in the concluding section of each chapter. This study is predominantly experimental, with some theory being presented to complement the results. Part I of this thesis is organized as follows

- The remainder of Chapter 1 is dedicated to clarifying relevant parameters and definitions and describing the experimental setup employed.
- Chapter 2 researches the dynamics of inverted flags in the limit of very small aspect ratio, which are markedly different to those of the large-aspect-ratio case.
- Chapter 3 addresses the dynamics of inverted flags that are placed at moderate angles of attack to the flow and the modified behavior that arises as this angle

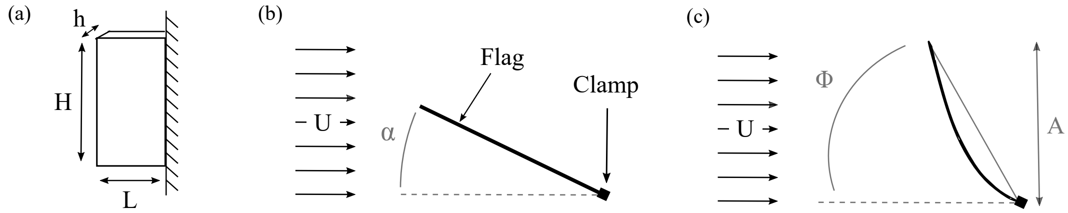

Figure 1.2: Side and top view of the inverted flag with parameters employed to characterize (a) dimensions (H, L and h), (b) angle of attack, α, and (c) deflection, Φ, and amplitude, A

is increased.

- Chapter 4 delves into the behavior of two inverted flags when they are placed in a side-by-side configuration and the interactions and coupling that ensue.
- Chapter 5 concludes the investigation on inverted flags and highlights the most imperative avenues for future work.

1.2 Parameters and definitions

The mathematical description of the inverted flag presented in the literature closely follows that developed for the more general case of an elastic plate with arbitrary boundary conditions (Argentina and Mahadevan, 2005; Kornecki et al., 1976). Accordingly, similar variables and parameters have been introduced to define the inverted flag's behavior. The nomenclature used throughout this thesis is presented hereafter.

The flag's dimensions — length, L, width, H, and thickness, h — have been represented in figure 1.2a. The non-dimensional parameters that determine the behavior of the inverted flag are the angle of attack, α, the non-dimensional velocity, κ, the mass ratio, μ, the aspect ratio, AR, and the Reynolds number, Re. The angle of attack, α, corresponds to the fixed angle of the trailing-edge clamp with respect to the free-stream velocity and is represented in figure 1.2b. The remaining parameters are defined as follows

$$\kappa = \frac{\rho_f U^2 L^3}{D}, \qquad \mu = \frac{\rho_s h}{\rho_f L}, \qquad AR = \frac{H}{L}, \qquad Re = \frac{\rho U L}{\mu_f},$$

where U is the free-stream velocity, ρ_f is the density of the fluid, D the flexural stiffness of the flag ($D = Eh^3/(12(1-\nu^2))$ with ν the Poisson ratio), ρ_s the density of the flag and μ_f the viscosity of the fluid. The non-dimensional velocity, κ, represents the ratio of fluid inertial to solid elastic forces, while the Reynolds number, Re, corresponds to the ratio of fluid inertial to fluid viscous forces. The mass ratio, μ, on the other hand, is representative of the relative mass of the flag to that of the fluid it displaces.

The resulting flag's motion is characterized throughout this text using two main parameters, the flag's deflection angle, Φ, and the Strouhal number, St. The deflection angle, Φ, is represented in figure 1.2c and corresponds to the instantaneous angle between the line that joins the flag's leading and trailing edges and the free-stream velocity. Its use differs from previous studies such as Kim et al. (2013) that utilize the amplitude of motion (A, figure 1.2c) as the defining parameter. The choice stems from the non-injectivity of the amplitude of motion: for a given amplitude there are two possible flag positions, one with $\Phi < 90$ and one with $\Phi > 90$. Because a flag can deform under different modes, the deflection angle is not strictly injective either. However, it was experimentally observed that for a given flag at specified flow conditions each deflection angle corresponds to a unique flag position. Variables derived from this parameter, such as the angular amplitude $\Delta\Phi = \Phi_{max} - \Phi_{min}$ and the mean deflection angle, $\bar{\Phi}$, will be employed occasionally. The Strouhal number is defined as follows

$$St = \frac{fA'}{U}$$

where f is the frequency of oscillation and U the free-stream velocity. The cross section A' is calculated as the maximum between $A_{max} - A_{min}$ and $|A_{max}|$, where A_{max} is the maximum amplitude, A_{min} the minimum amplitude and the clamping point is located at A=0. This amplitude corresponds to the cross-flow distance between the shed vortices.

The value of the Reynolds number varies between 10^3 and 10^5 in the experiments presented. The characteristic features of the inverted-flag dynamics and vortex wake have been shown to be fairly insensitive to Reynolds number for $Re > 100$ (Shoele and Mittal, 2016; Tang et al., 2015). For these large Re, the characteristic curves of the flag's motion collapse when represented as a function of κ, independently of flag dimensions, showing that variations with free-stream velocity are a result of the changing behavior with κ and not a Reynolds number effect. For this reason, the effect of Reynolds number has not been analyzed in this study. Similarly, all experiments were performed in air, and although the mass ratio varied due to the varying flag dimensions its order of magnitude was always $O(1)$. Because such small variations in μ have a negligible effect on the flag's dynamics, the effect of the varying mass ratio has not been considered in this study.

1.3 Experimental setup

The experimental measurements of inverted flags presented in this thesis were performed in an open-loop gust-and-shear wind tunnel constructed at Caltech. A photograph of the experimental setup can be viewed in figure 1.3. The tunnel, similar in design to that of Johnson and Jacob (2009), generates the flow through an array of 10×10 small computer fans. Each row of fans can be controlled individually, allowing for the generation of shear flows, and the fast response of the small fans further allows for the generation of gusts. In this thesis, however, the only flow employed was a uniform steady flow. The tunnel is capable of generating flow speeds between 2.2m/s and 8.5m/s. The variation in the generated free-stream velocity across the tunnel's cross section, caused by the multiplicity of fans, is under 2.7%.

The turbulence intensity at different flow speeds, measured using a hotwire system, is shown in figure 1.4. These intensities are significantly higher than those present in traditional wind tunnels and result in large perturbations to the flag. It is particularly important to consider these perturbations when performing stability analyses; corresponding remarks have been made in the relevant sections of chapters 2 and 3. The control of the individual computer fans is achieved using a pulse-width-modulated signal, resulting in an overshoot of the fan velocity before the steady state is reached. The measurements presented in this manuscript correspond to steady state results — a stabilizing period of at least 30 s was allowed between tunnel velocity modification and recording of data. It is important to note that the inverted flag's motion presents bi-stable regions for certain ranges of the flow velocity. Due to the overshoot when modifying the tunnel's flow velocity, the presence of these regions must be assessed in this setup by modifying the initial conditions of the flag.

The test section of the wind tunnel has a length of 1.9m and a square cross section of $1.2\text{m} \times 1.2\text{m}$. The largest flag tested had dimensions of $0.2\text{m} \times 0.4\text{m}$, resulting in a maximum blockage ratio of 4.7%. No blockage effects were observed in any of the tests performed. The flags were clamped at their trailing edge using two aluminum bars of dimensions $12\text{mm} \times 6\text{mm} \times 1.2\text{m}$. For the study presented in Chapter 4, where a side-by-side flag arrangement is analyzed, two sets of clamping bars were

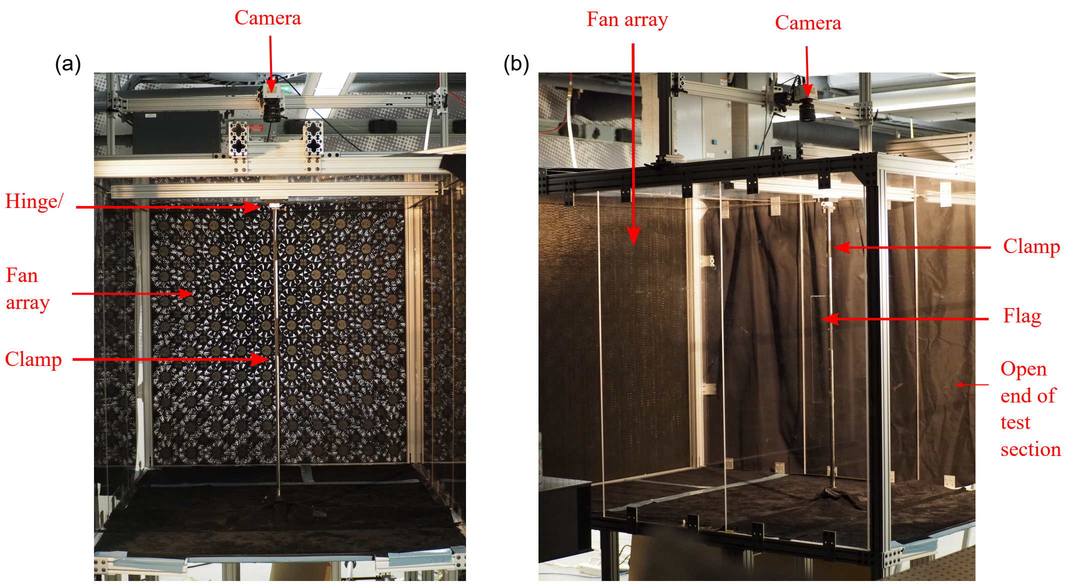

Figure 1.3: Experimental setup from (a) end of test section and (b) side of test section

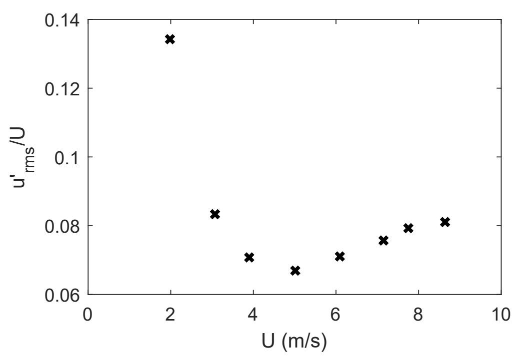

Figure 1.4: Turbulence intensity of the fan array wind tunnel for varying wind speeds

positioned side-by-side and on a rail, such that the distance between flags could be varied. The clamping bars are positioned vertically in the test section to minimize the effect of gravity on the flag dynamics. The deformation of the flag was observed to be two-dimensional in the horizontal plane for the majority of test cases, with the lowest aspect ratio flags being the exception. A discussion of the twisting and the effect of gravity on these flags is presented in Section 2.2. In order to set the desired flag angle of attack, the clamping bars were attached to a hinge that allows rotation around the vertical axis. It is equipped with a dial that shows angles in two-degree increments, resulting in an error in the angle of attack of $\pm 1°$.

Test	Flag number	Dimensions (mm)			AR	μ
		Length	Width	Thickness		
Aspect ratio	1	300	10	0.76	0.033	2.49
	2	300	20	0.76	0.067	2.49
	3	300	30	0.76	0.1	2.49
	4	300	40	0.76	0.13	2.49
	5	195	195	0.51	1	2.55
	6	195	97.5	0.51	0.5	2.55
Angle of attack	7	82	410	0.25	5	3.03
	8	160	320	0.51	2	3.11
	9	180	360	0.51	2	2.76
	10	190	380	0.51	2	2.62
	11	200	400	0.51	2	2.49
Coupling	12	100	150	0.25	1.5	2.48
	13	85	150	0.25	1.76	2.93
	14	90	150	0.25	1.67	2.76
	15	93	150	0.25	1.61	2.68
	16	95	150	0.25	1.58	2.62
	17	98	150	0.25	1.53	2.54
	18	102	150	0.25	1.47	2.44
	19	105	150	0.25	1.73	2.37
	20	107	150	0.25	1.4	2.33
	21	110	150	0.25	1.36	2.26
	22	115	150	0.25	1.3	2.16

Table 1.1: Numbering, dimensions and properties of the inverted flags tested

The motion of the flags was filmed using a high-speed camera (Imperx IPX-VGA210-L or Dantec Dynamics Nanosense MKIII) located above the test section. Images were acquired at frame rates between 20 frames per second and 100 frames per second in sets between 200 and 8,100 frames long. The position of the top edge of the flag, marked with white paint, was tracked in the acquired frames using a MATLAB script. The minimum edge to clamp distance in the acquired images is of 60 pixels and the tracking script was observed to detect the flag edge within four pixels, resulting in errors in the measurement of ϕ smaller than 4°. The dominant frequency of motion of the flag can be subsequently determined making use of the fast Fourier transform of the deflection angle's time series. Measurements of the local deflection angle at the plate's free end were required for a comparison with theoretical results in Chapter 2. They were obtained by fitting a third-order polynomial to the deflected flag shape over the last 20% of the flag length.

The flags consisted of polycarbonate plates with a density of $\rho_s = 1200\text{kg/m}^3$, Young's modulus of $E = 2.41\text{GPa}$ and Poisson ratio of $\nu = 0.38$. A small initial curvature of up to 5° was present in the plates due to fabrication and material defects. This curvature was measured experimentally by clamping the flags in the wind tunnel and acquiring images with the fan array turned off. It corresponds to a single mode of deformation; the flags were observed to present similar curvatures in both streamwise and cross-stream directions. Viscoelastic effects in the flag's deformation were only observed for the smallest aspect ratio flags, analyzed in Chapter 2. No time dependence was observed in the deflected stable equilibrium shapes of these flags, confirming that any viscoelastic properties exert a weak effect. Each of the flags used has been assigned a flag number to facilitate identification throughout this text. They are presented, together with their dimensions, aspect ratio and mass ratio, in table 1.1.

Chapter 2

STABILITY OF SLENDER INVERTED FLAGS

John E Sader, Cecilia Huertas-Cerdeira, and Morteza Gharib. Stability of slender inverted flags and rods in a uniform steady flow. *Journal of Fluid Mechanics* 809:873–894,2016.

The main findings highlighted in Chapter 1 correspond to inverted flags of relatively high aspect ratios (AR>1). Above that threshold, the general features of the flag's behavior are consistent independently of this parameter. Variations with aspect ratio have been reported, however, in the values of the critical velocities, as well as the amplitudes and frequencies of flapping. Preliminary experimental results by Cossé et al. (2014) and a more detailed follow-up in Sader et al. (2016a) indicated that the critical value of the non-dimensional velocity, κ, at which the flag enters the flapping regime increases as aspect ratio is decreased, while the value of κ at which the flapping motion disappears remains constant for all aspect ratios. Similar results were numerically obtained at Re=200 by Tang et al. (2009), who observed, nonetheless, a small variation in the values of κ at which flapping ceases. Tang et al. (2015) reported an approximately constant overall maximum flapping amplitude, A, although the velocity at which higher aspect ratios reached this value was lower, showing a wider maximum-amplitude plateau. A substantial decrease in Strouhal number was additionally reported as aspect ratio decreased.

As was highlighted in Chapter 1, the onset of flapping of high-aspect-ratio inverted flags is caused by a divergence instability. Sader et al. (2016a) presented a theoretical analysis that is able to predict the onset of flapping for flags of aspect ratio AR>1. Their model followed the steady version of the theory developed by Kornecki et al. (1976) which considers two-dimensional, inviscid, incompressible flow combined with the equilibrium equation of an elastic plate and the corresponding boundary conditions. The divergence velocity is then computed making use of the Rayleigh quotient. The analytic formula, valid for varying aspect ratios, was obtained by correcting this infinite aspect ratio value with a factor of $1 + \frac{2}{AR}$, as derived from Prandtl's lifting line theory making the assumption of a negligible Glauert coefficient (Anderson Jr, 2010; Glauert, 1983). The formula obtained reasonable agreement with experiments for aspect ratios up to 1. Formally, Prandtl's lifting line theory is an asymptotic formula for high aspect ratios. It is generally considered to hold closely for AR>4 (Bollay, 1939), with vortex lattice methods being used for AR>1. At smaller aspect ratios the edge vortices produce non-linear effects that cannot be captured by this linear theory. The formula obtained by Sader et al. (2016a) strongly overpredicts the transition velocity of inverted flags of these small aspect ratios, consistent with a vortex lift mechanism that enhances the lift on the flag, therefore reducing the critical velocity.

The objective of this chapter is to characterize the behavior of slender inverted flags (AR<1). It is important to note that the experimental results by Cossé et al. (2014) and Sader et al. (2016a) established the existence of a flapping regime for AR>0.2 only. Under that threshold, the flag transitions directly from oscillating around a small deflection position to oscillating around a large deflection equilibrium. Consequently, the theoretical analysis presented in Section 2.1, developed by collaborators at the University of Melbourne for the limit of AR$\rightarrow 0$, addresses the existence and stability of steady state equilibria only. The experiments presented in Section 2.2, give further insights into the effect of a finite, but small, aspect ratio and the system's dynamics.

2.1 Theory

A theoretical framework for the stability of inverted flags in the limit of zero aspect ratio was developed by Prof. John Sader and is summarized below. A more extensive description can be found in Sader et al. (2016b). The theory is based on the result by Bollay (1939), who considered the effect of edge vortices that trail at an angle to the free-stream velocity, obtaining a non-linear theory for the lift of flat plates of AR<1. In the limit of zero aspect ratio, the normal force coefficient becomes

$$C_N = 2\pi \sin^2 \alpha \tag{2.1}$$

with α the angle of attack of the plate. The equilibrium equation for a beam undergoing large-deformation pure bending (Landau and Lifshitz, 1970) is given by

$$EI\frac{d^2\theta(s_*)}{ds_*^2} = -\mathbf{n}(s_*) \cdot \int_{s_*}^{L} \mathbf{F}(l_*)\, dl_*, \tag{2.2}$$

where $\theta(s_*)$ is the local rotation angle of the beam, s_* (and the equivalent integration variable l_*) is the dimensional arc-length along the beam ($s_* = 0$ at the clamped end) as defined in figure 2.1. E is the Young's modulus of the beam, I is its areal

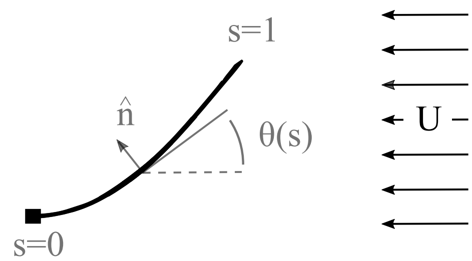

Figure 2.1: Definition of local rotation angle of the beam, $\theta(s)$, and arc-length along the beam, s.

moment of inertia, **F** is the local applied force per unit length and **n** is the local unit normal to the beam's axis at position l_*. Equation (2.2) satisfies the required zero force condition at the free end of the cantilever($s_* = L$).

Combining equations 2.1 and 2.2, the equilibrium equation for the slender inverted flag becomes

$$\frac{d^2\theta}{ds^2} = -\kappa' \int_s^1 |\sin\theta(l)| \sin\theta(l) \cos(\theta(s) - \theta(l))\, dl, \tag{2.3}$$

where the dimensionless arc-length, $s \equiv s_*/L$ (and $l \equiv l_*/L$), is now used. The dimensionless velocity κ' is the beam equivalent of κ as defined in Section 1.2, where the flexural rigidity has been substituted by that of a beam of rectangular cross section $D' = Eh^3/12$. The absolute value in the right-hand side is included to account for the inherent symmetry in the flag's deflection. The corresponding boundary conditions are

$$\theta(0) = \left.\frac{d\theta}{ds}\right|_{s=1} = 0, \tag{2.4}$$

Equation 2.3 can be solved numerically, using a finite difference discretization combined with a shooting method, where the angle at the free end of the cantilever, $\theta_{end} = \theta(1)$, is adjusted to match the required clamp condition, $\theta_{clamp} = \theta(0) = 0$ (Luhar and Nepf, 2011). The obtained results are represented in figure 2.2 and show the existence of a saddle-node bifurcation, in contrast to the divergence instability present in the large-aspect-ratio case. The variable employed is θ_{end}, which is equivalent but not equal to the deflection angle, θ. For small values of κ', a single solution to equation 2.3 exists. It corresponds to the zero deflection equilibrium ($\theta_{\text{end}} = \theta_{\text{clamp}} = 0$). As κ' is increased, a second solution, corresponding to the deflected equilibrium $\theta_{end} = 66.7°$, appears and further divides into two distinct

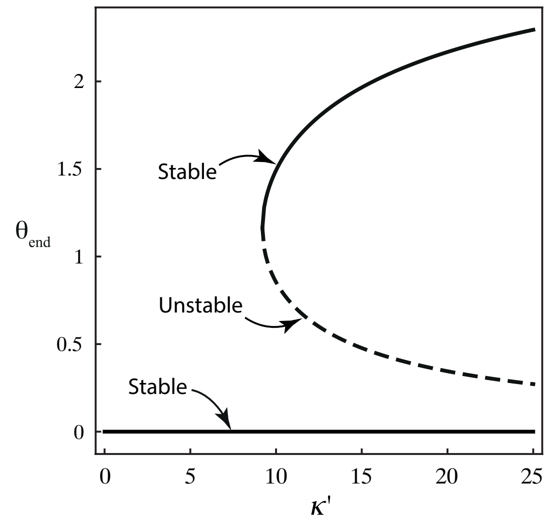

Figure 2.2: Theoretical bifurcation diagram of the inverted flag's free end angle θ_{end} vs. normalized flow speed κ' in the limit AR $\rightarrow$ 0. Solid curves correspond to stable equilibria, dashed curves correspond to unstable equilibria. Only positive angles are shown – negative angles have symmetric behavior.

equilibria for higher values of κ'. The critical κ' at which this saddle-node bifurcation occurs is $\kappa'_{crit} = 9.205$. The stability of these equilibria can be deduced from the fact that the aerodynamic force does not present a linear term (equation 2.1), and therefore the zero-deflection equilibrium must necessarily be linearly stable.

The results in figure 2.2 have been obtained using a steady aerodynamic force and do not account for the unsteadiness of the separated flow. Inverted flags of AR<0.2 do not present large-amplitude flapping, and therefore, as will be shown experimentally in Section 2.2, the unsteady effects are limited to generating small amplitude oscillations around the equilibria. In order to gain some intuition on the system's stability and dynamics, a simplified rigid flag model, that reduces the flag motion to a single degree of freedom, can be employed. The equation of motion of a rigid beam that is mounted on a torsional spring at its trailing edge is given by

$$\frac{d^2\bar{\theta}}{dt^2} + \frac{1}{Q}\frac{d\bar{\theta}}{dt} + \bar{\theta} - \bar{\kappa}\left|\sin\bar{\theta}\right|\sin\bar{\theta} = F(\bar{\theta}, t), \tag{2.5}$$

where $\bar{\theta}$ is the beam's rotation angle, $\bar{\kappa}$ is analogous to the non-dimensional flow speed and accounts for the spring's constant, Q is the quality factor, t is scaled time and $F(\bar{\theta}, t)$ is an unspecified external applied force due to the unsteady hydrodynamic force arising from vortex shedding and any turbulence in the impinging flow. The potential energy of the steady system (third and fourth terms) can be calculated and provides insight into the competing elastic and steady aerodynamic forces. It is given by

$$V(\bar{\theta}) = \frac{1}{2}\bar{\theta}^2 - \frac{\bar{\kappa}}{2}\left|\bar{\theta} - \frac{1}{2}\sin 2\bar{\theta}\right|, \tag{2.6}$$

and is plotted in figure 2.3. In this figure, the stationary points correspond to equilibrium solutions and agree with the bifurcation diagram presented in figure 2.2. For small values of $\bar{\kappa}$, the zero deflection equilibrium is solely present. As $\bar{\kappa}$ is increased a saddle-node bifurcation occurs and an unstable (potential maximum) and stable (potential minimum) equilibria appear. This simplified model notably shows the basins of attraction of the equilibria. At $\bar{\kappa}$ slightly above the bifurcation velocity, the potential well of the stable deflected equilibrium is shallow and the energy required to reach the unstable equilibrium from it is small; any small perturbation will lead the flag back to the stable zero-deflection equilibrium. In contrast, at high values of $\bar{\kappa}$ the potential well of the deflected equilibrium is steep and the energy required to exit the zero-deflection equilibrium is small; perturbations will lead the flag towards the deflected equilibrium. This explains why, despite the zero-deflection equilibrium being always stable, all experimental investigations up to date have reported that increasing wind speed results in the flag transitioning from the zero-deflection state to the deflected state. The intermittency inherent to low aspect ratio inverted flags is further analyzed in Section 2.2.

The normalized velocity κ' at which inverted flags in the AR $\rightarrow 0$ limit undergo a saddle-node bifurcation can be translated to the large aspect ratio variable κ as follows

$$\kappa_{small} = 9.205(1 - \nu^2) \tag{2.7}$$

with ν the Poisson ratio of the flag. The theory presented by Sader et al. (2016a) for the AR $\rightarrow \infty$ limit predicted a divergence instability at a value of

$$\kappa = \kappa_{large}\left(1 + \frac{2L}{H}\right) \tag{2.8}$$

where

$$\kappa_{\text{large}} = 1.85. \tag{2.9}$$

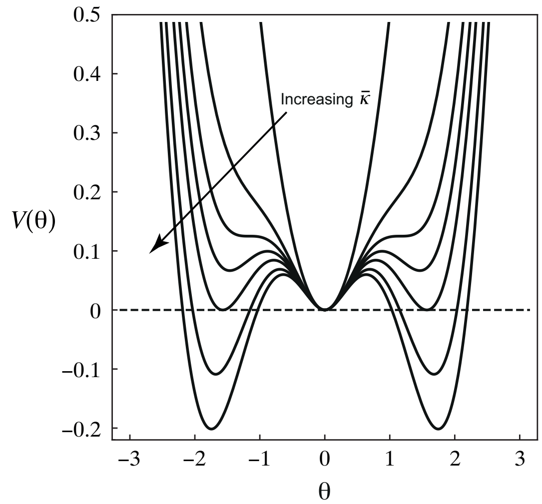

Figure 2.3: Potential energy function, $V(\bar{\theta})$, of the rigid beam model system for $\bar{\kappa} = 0, 1.2, 1.38, 1.48, \pi/2, 1.7, 1.8$ (increasing from center outwards); saddle-node bifurcation occurs at $\bar{\kappa} = 1.38$. Both positive and negative angles are given.

These two equations for the asymptotic limits can be combined using a Padé approximant to obtain a formula that can predict the end of the straight regime for flags of all aspect ratios

$$\kappa \approx \kappa_{\text{large}} \frac{\kappa_{\text{small}} + \left(\kappa_{\text{small}} - \kappa_{\text{large}}\right) \frac{H}{2L}}{\kappa_{\text{large}} + \left(\kappa_{\text{small}} - \kappa_{\text{large}}\right) \frac{H}{2L}}, \tag{2.10}$$

Because the zero-deflection regime of the low aspect ratio limit is always stable, and the flag only deflects as its basin of attraction becomes sufficiently small, formula 2.10 should be taken as a lower bound. It is plotted, together with both asymptotic theories and experimental results by Sader et al. (2016a) in figure 2.4 and shows good agreement throughout.

The possible existence of multiple equilibria, as predicted theoretically in this section, was explored experimentally. These measurements aim to test for the presence of these equilibria, as well as give insight into the flag's dynamics and the behavior of flags of small but finite aspect ratios.

2.2 Results

Multiple equilibrium states of the flag

The new measurements verify the existence of multiple equilibrium states, as predicted theoretically in Section 2.1. This theory does not, however, account for

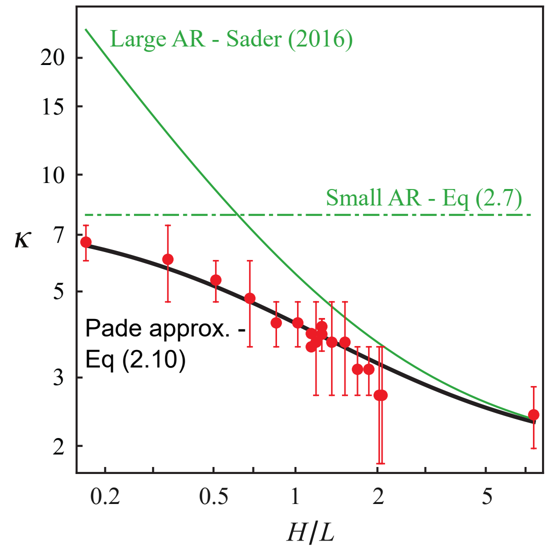

Figure 2.4: Comparison of measurements and theoretical predictions for the critical normalized flow speed at bifurcation, as a function of aspect ratio, H/L. Equation (2.8) [upper curve, large aspect ratio solution], (2.7) [horizontal line, small aspect ratio solution] and (2.10) [lower curve, globally valid Padé approximant].

dynamic effects, which modify the behavior of the flag. For the smallest aspect ratios, $H/L < 0.2$, the flag was experimentally observed to oscillate with small amplitude around the stable equilibrium positions. In those cases, the deflected stable equilibrium position, presented in figure 2.5, was measured by taking the average of a 30 s time series. Large-amplitude flapping occurs for aspect ratios $H/L > 0.2$ (Sader et al., 2016a). In these cases, the flag was damped to observe a deflected equilibrium; this was achieved by lightly touching the flag with a thin rigid pole.

Existence of an unstable deflected equilibrium was assessed as follows. The initial position of the flag was adjusted by quasi-statically pushing it from the stable deflected equilibrium position towards the zero-deflection position using a thin and rigid pole. Presence of an unstable deflected equilibrium must then lead to rapid and unassisted movement of the flag from the deflected initial condition towards the zero-deflection equilibrium. The deflected shape of the sheet at the time of loss of contact with the pole is taken to be the unstable deflected equilibrium.

Figure 2.5 shows the measured angle of the cantilevered sheet's free end at the stable and unstable deflected equilibria. Measurements from several flags of varying small aspect ratios are presented, together with the theoretical predictions of Section 2.1. As the aspect ratio is reduced (left-to-right and top-to-bottom in figure 2.5), both the measured critical bifurcation flow speed κ'_{small} and the free end angle θ_{end} increase,

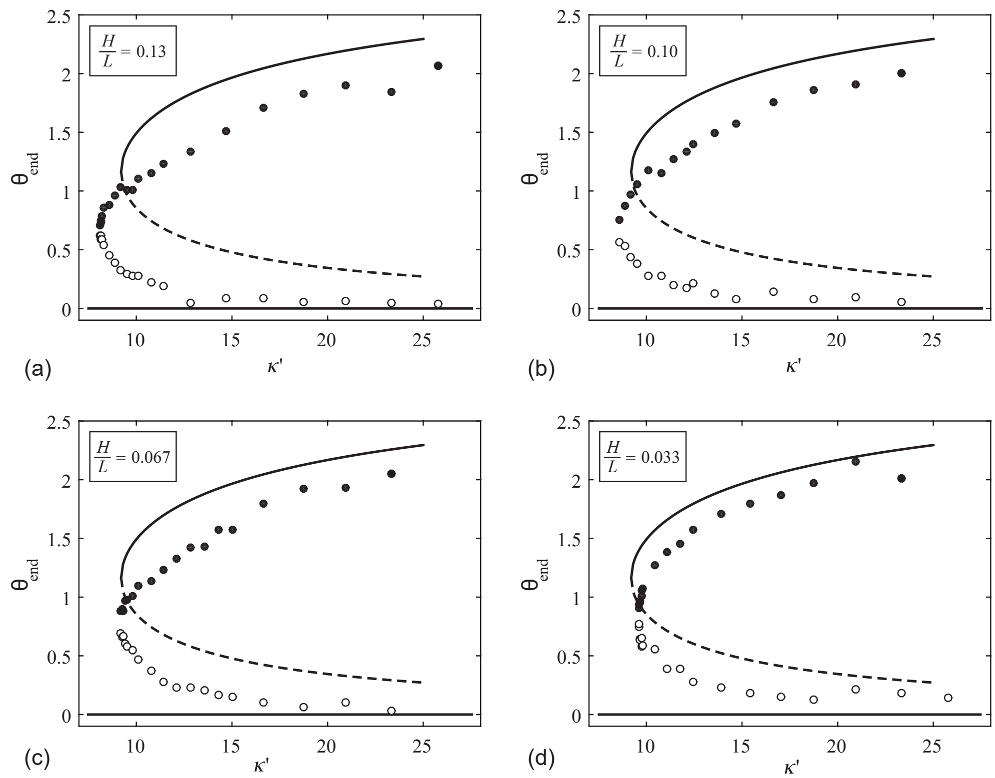

Figure 2.5: Measured free end angle, θ_{end}, at the stable (●) and unstable (○) deflected equilibria for aspect ratios of (a) $H/L = 0.13$, (b) $H/L = 0.10$, (c) $H/L = 0.067$, (d) $H/L = 0.033$. Theoretical prediction using the $H/L \to 0$ asymptotic theory of Section 2.1 is given for stable (upper solid curve) and unstable (dashed curve) equilibria. Zero-deflection equilibrium position is shown for reference (horizontal solid line).

shifting towards the theoretical ($H/L \to 0$) curve of Section 2.1. While there are some differences, even at the smaller aspect ratios, the measurements clearly approach the theoretical asymptotic solution as H/L is reduced.

Interestingly, the measurements reported in figure 2.5 systematically underestimate the $H/L \to 0$ asymptotic theory. This may be due, in part, to twisting of the flag which is observed to always occur when the flag deflects from its zero-deflection equilibrium. This twisting deformation is shown in figure 2.6 and exhibits a commensurate downward displacement of the flag. Large deformation of elastic beams inevitably results in coupling between bending and torsion, if the load or beam is not perfectly symmetric about the beam's major axis (Landau and Lifshitz, 1970). Strikingly, every inverted flag studied here deforms in precisely the same manner — with the free end deflecting vertically downward in the gravity direction — demonstrating that gravity provides a symmetry break. When the flags are deflected sideways by applying a horizontal force with a stiff thin pole and the bank of fans are turned off, i.e., no flow, the large amplitude twisting shown in figure 2.6 is not observed, suggesting that the initial break in symmetry is small. The resulting small twist, however, appears sufficient to modify the aerodynamics of the flag such that an additional torsional aerodynamic force is generated, resulting in a large twisting deformation. This coupled bending/twisting deformation is expected to reduce the drag experienced by the inverted flag because the flag now presents an angled face to the incoming flow. Such drag reduction reduces the maximum deflection angle of the inverted flag for a given flow speed, consistent with the observations reported in figure 2.5. While non-linear coupling between bending and twisting under a gravitational load can be calculated, this complexity detracts from the principal aim of this study which is to describe the dominant stability mechanisms of slender inverted flags. The experimental angles reported in figure 2.5 are measured by observing the flag from above, and as such, they correspond to the projection of the deflection angle on the horizontal plane.

Bollay's 1939 calculations indicate that the normal force experienced by a rigid and flat blade of small but finite aspect ratio contains a term proportional to $\sin^2\theta$ and one proportional to $\sin 2\theta$. As such, a small but measurable linear lift component is expected, which may contribute to the observed differences between measurement and theory in figure 2.5. This mechanism acts in addition to the reduction in drag due to twisting, and its presence and strength are explored using independent measurements in Section 2.2.

Measurements by Sader et al. (2016a) found no evidence for the existence of the multiple equilibria reported in figure 2.5. However, their study focused primarily on flags of large aspect ratio, H/L. It is therefore important to determine the aspect ratio at which the multiple equilibria emerge. A systematic experimental investigation using the present setup reveals that these multiple equilibria occur only for $H/L < 1.7$. Figure 2.7 gives the measured bifurcation diagram, i.e., the stable and unstable equilibrium end angles, θ_{end}, as a function of the normalized flow speed, κ', for several aspect ratios, H/L, in this range.

The linear component of the hydrodynamic force described above, i.e., the $\sin 2\theta$ term, is expected to increase in strength with increasing aspect ratio. Unlike the limiting case of $H/L \to 0$ where the zero-deflection equilibrium is always linearly stable, this additional linear component will cause the zero-deflection equilibrium of finite aspect ratio flags to become linearly unstable at finite flow speed. This behavior

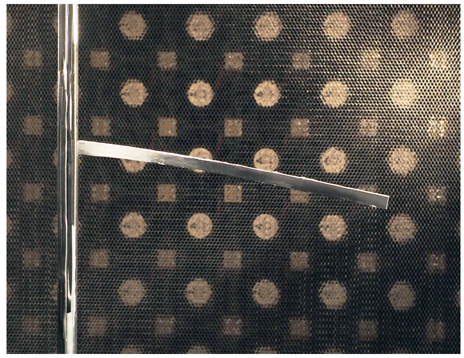

Figure 2.6: Photograph of slender inverted flag showing the combined flexural bending and twisting at large flow speeds, under the influence of gravitational and hydrodynamic loading; $H/L = 0.033$, $\kappa' = 16.6$. The bank of computer fans is visible with the flow direction out of the page. The flag is deflected strongly to the right relative to the flow direction, exhibiting a twist about its major axis together with commensurate bending in both the horizontal and vertical directions. The supporting aluminum bar is oriented in the vertical direction.

is evident in figure 2.7, where the unstable deflected equilibrium branch (dashed curves) crosses the zero axis, causing the zero-deflection equilibrium to become linearly unstable. The critical κ'-value at which this crossing occurs decreases as H/L is increased, as would be expected for an increasing linear component of the normal force. Indeed, this observed decrease in the unstable equilibrium's free end angle θ_{end} at bifurcation, with increasing H/L (see figure 2.7), is consistent with the large aspect ratio theory of Sader et al. (2016a): for large H/L, the deflected unstable equilibrium does not exist and a divergence instability of the zero-deflection equilibrium occurs.

Intermittent dynamics at moderate flow speeds

The rigid sheet model described by equation (2.5) does not explicitly account for the effects of nonlinear damping or unsteady hydrodynamic forces, such as those produced by vortex shedding and turbulence in the flow; these are lumped into the unspecified forcing term $F(\bar{\theta}, t)$. Therefore, it does not completely model the dynamics of the inverted flag. However, (2.5) does prove useful in gaining a qualitative understanding of the inverted flag's stability and dynamics. For small values of $\bar{\kappa}$, the secondary potential well at finite $\bar{\theta}$ (corresponding to the stable deflected equilibrium) is shallow; see figure 2.3. This suggests that residence at this minimum is energetically unfavorable and small fluctuations in the flow will drive the flag away from the stable deflected equilibrium. This behavior is now

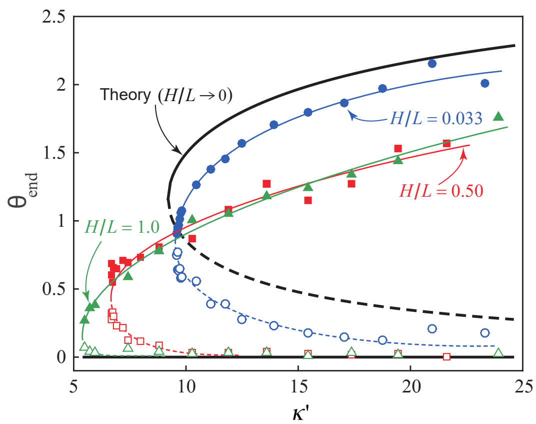

Figure 2.7: Measured free end angle, θ_{end}, of inverted flags at their stable (•) and unstable (∘) deflected equilibria as a function of the normalized flow speed, κ'. Measurements shown for flags of aspect ratios of $H/L = 0.033$ (blue circle), $H/L = 0.50$ (red square) and $H/L = 1.0$ (green triangle). To guide the eye, fit curves to these measured data points are provided for each aspect ratio. Theoretical prediction is given for the limiting case of $H/L \to 0$ (solid black curves: stable equilibria; dashed black curve: unstable equilibrium). Undeflected shape (zero angle) is the horizontal black line.

investigated experimentally.

Figure 2.8(a) shows the variation in time of the non-dimensional displacement of the flag's free end, A/L, for $\kappa' = 9.2$. This flow speed is just above the bifurcation point where the two deflected equilibria emerge in measurements. Initially, the flag fluctuates around the zero-deflection equilibrium. Using a thin and rigid pole, the flag is pushed (dashed red curve) to the stable deflected equilibrium position where it is released. The flag then resides at that position for finite time (≈ 25 s) until it abruptly, and of its own accord, falls back into the zero-deflection position. This observation is consistent with the energetic picture in figure 2.3 where fluctuations in the flow are expected to result in intermittent dynamics.

As $\bar{\kappa}$ is increased in the model system, its deflected energy minimum depresses below the zero-deflection energy minimum; see figure 2.3. Physically, this lets small fluctuations drive the flag from the zero-deflection equilibrium towards the more energetically favorable deflected equilibrium. A measurement under this scenario is shown in figure 2.8(b), corresponding to a normalized flow speed of $\kappa' = 14.3$. The flag, initially oscillating around the deflected equilibrium, is forced (dashed red curve) with the thin pole to the zero-deflection position where it is again released. The flag then resides briefly (≈ 3 s) at the zero-deflection position before returning suddenly and unaided to the deflected equilibrium position. The above-reported intermittency is expected to depend on fluctuations due to unsteady vortex shedding and on the level of turbulence in the impinging flow, with increased movement between multiple equilibrium states as the turbulence level is raised.

As mentioned above, the flag exhibits oscillations about both the zero-deflection ($A/L = 0$) and deflected ($A/L > 0$) equilibria in these measurements. The deflected equilibrium's oscillation amplitude is different in figures 2.8(a) and (b), with larger oscillations occurring at the lower flow speed (in figure 2.8(a)). This is expected because the energy minimum at the deflected equilibrium is shallower at the lower flow speed, as discussed above, allowing time-dependent fluctuations in the flow to more strongly perturb the sheet from this equilibrium position. The zero-deflection equilibrium exhibits reversed behavior, with larger oscillations being observed at the higher flow speed in figure 2.8(b). This is again explained by the energy landscape in figure 2.3, as the zero-deflection equilibrium's energy minimum is shallower at higher flow speeds — behavior opposite to that of the deflected equilibrium's energy minimum. Therefore, the observed oscillation amplitudes of the zero-deflection and deflected equilibria are entirely consistent with their intermittent dynamics discussed above.

Presence of a linear hydrodynamic lift force at finite aspect ratio

We now examine whether a linear lift force indeed exists for inverted flags of small but finite aspect ratio, as suggested by the results of Section 2.2. This is achieved by performing independent measurements of the natural resonant frequency of the inverted flags at their zero-deflection equilibrium positions, as a function of aspect ratio.

When a slender inverted flag is placed at its zero-deflection equilibrium at finite flow speed, it is observed to resonate with small amplitude; see figure 2.8. For such small amplitudes, the quadratic (fourth) term on the left hand side of the rigid sheet model system (2.5) — which holds formally in the limit $H/L \to 0$ — is small relative to the linear (third) term, provided $\bar{\kappa}$ is not large. The equation of motion for a damped harmonic resonator is then recovered. This equation depends on $\bar{\kappa}$ only through variations in the normalized damping coefficient, $1/Q$, and the external applied (hydrodynamic) force, $F(\bar{\theta}, t)$. These variations can both generally be considered small for small oscillation amplitudes. The resonant frequency of the flag is therefore weakly dependent on $\bar{\kappa}$ in this zero-aspect-ratio limit.

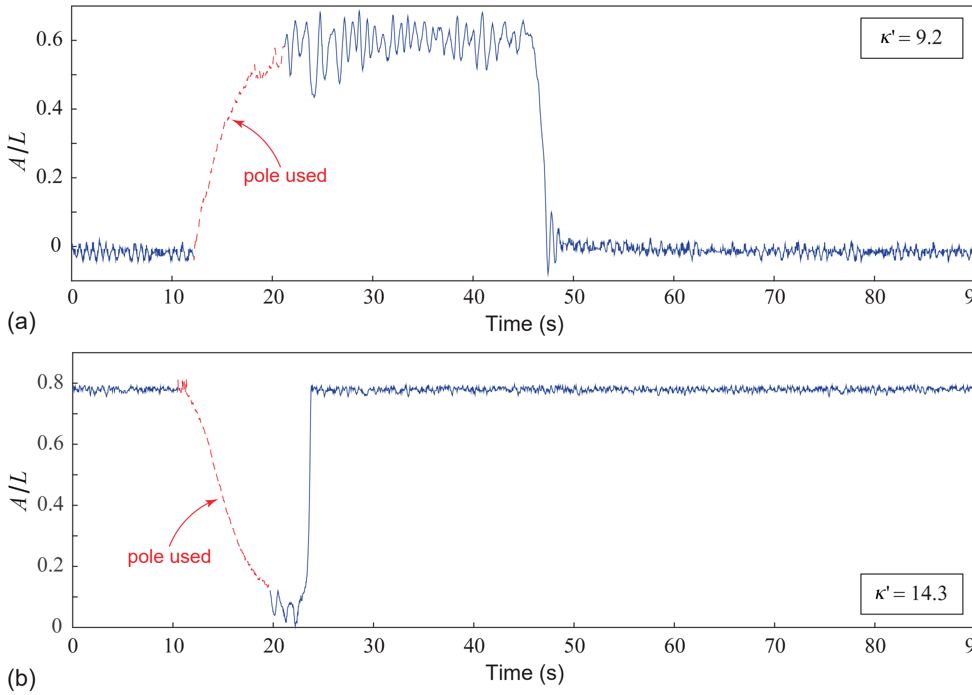

Figure 2.8: Measured dimensionless free end displacement A/L of an inverted flag as a function of time, for normalized flow speeds of (a) $\kappa' = 9.2$ and (b) $\kappa' = 14.3$. Aspect ratio $H/L = 0.067$. The flag is shifted to a different equilibrium using a thin rigid pole (red dashed curve) and then released.

For small but finite aspect ratio ($H/L \ll 1$), however, the hydrodynamic force on the rigid sheet includes a linear term, as discussed above (Bollay, 1939). In addition to the non-linear lift specified by Eq. (2.1) for a rigid slender blade, a linear normal lift force coefficient per unit length of the form $C_N = 2c \sin\theta \cos\theta$ arises, as discussed in Section 2.2. Here, $c = 0$ in the zero aspect ratio limit ($H/L \to 0$) and is an increasing function of aspect ratio. Equation (2.5) thus takes the modified form,

$$\frac{d^2\bar{\theta}}{dt^2} + \frac{1}{Q}\frac{d\bar{\theta}}{dt} + \bar{\theta} - c\bar{\kappa}\sin\bar{\theta}\cos\bar{\theta} - \bar{\kappa}\left|\sin\bar{\theta}\right|\sin\bar{\theta} = F(\bar{\theta}, t). \tag{2.11}$$

For small oscillations around the zero-deflection equilibrium, this equation can be linearized to give

$$\frac{d^2\bar{\theta}}{dt^2} + \frac{1}{Q}\frac{d\bar{\theta}}{dt} + (1 - c\bar{\kappa})\bar{\theta} = F(\bar{\theta}, t). \tag{2.12}$$

This shows that the resonant frequency of the rigid sheet system (and an inverted flag) of small but finite aspect ratio, H/L, varies as a function of the square root of $1 - c\bar{\kappa}$ and Q, which is weakly dependent on $\bar{\kappa}$. Since c increases with increasing aspect ratio, larger aspect ratio sheets are expected to display a more significant reduction in their resonant frequency with increasing $\bar{\kappa}$.

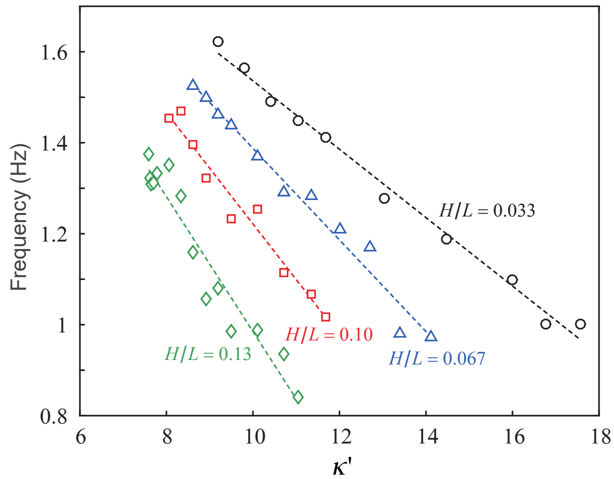

Figure 2.9: Natural frequency of oscillation of the zero-deflection equilibrium for inverted flags with aspect ratios of $H/L = 0.033$ (○), $H/L = 0.067$ (△), $H/L = 0.10$ (□) and $H/L = 0.13$ (◇). Linear fits to each data set are provided (dashed lines).

Figure 2.9 gives the measured oscillation frequency of the zero-deflection equilibrium for several flags, as a function of the normalized flow speed κ' and aspect ratio H/L. Although the dependence on κ' is not necessarily linear, a linear fit is provided to facilitate comparison. The measured rates of decrease in frequency are -0.15, -0.12, -0.10 and -0.075 Hz for aspect ratios of $H/L = 0.13$, 0.10, 0.067 and 0.033, respectively. This verifies the above physical picture: a linear lift force exists for finite aspect ratio and its magnitude increases with increasing aspect ratio.

A significant reduction in frequency as flow speed increases is observed even for the smallest aspect ratio of $H/L = 0.033$. This indicates that linear lift affects the flag's dynamics at this small aspect ratio. This finding is consistent with figure 2.7, where a difference is always observed between the $H/L \to 0$ theory of Section 2.1 and measurements at finite aspect ratio — even for the smallest aspect ratio of $H/L = 0.033$. As discussed, this mechanism acts in addition to twisting of the flag due to the combined effects of gravity and hydrodynamic loading, which leads to a reduction in deflection.

2.3 Conclusions

This chapter has addressed the behavior of slender (AR<1) inverted flags. Their stability has been shown to be remarkably different from that of their high aspect ratio counterpart. While the latter exhibits a divergence instability as flow speed increases, the undeformed state of an infinitely slender inverted flag is always locally stable. A saddle-node bifurcation emerges at finite flow speed, giving rise to two equilibrium states, with the more strongly deflected one being stable and the weakly deflected one unstable. The unstable equilibrium defines the boundary of the basin of attraction for the undeflected flag, which vanishes in the limit of high flow speed. The slender inverted-flag theory can be combined with that for large aspect ratio (Sader et al., 2016a), to yield a single formula for stability of the zero-deflection equilibrium, (2.10), that is valid for all aspect ratios.

Experimental measurements of inverted flags were performed and compared to theory, confirming he existence of multiple stable and unstable equilibria and the presence of intermittent dynamics. The experiments saw a significant twisting deformation that modified the position of the equilibria, as well as oscillations around the equilibrium positions. The presence of a saddle-node bifurcation was observed for aspect ratios up to 1.7. Inverted flags of small but finite aspect ratio were shown to present a combination of characteristics of both linear and quadratic fluid force dynamics.

The behavior of inverted flags of small but finite aspect ratios has been addressed in detail in a follow-up theoretical investigation by Tavallaeinejad et al. (2018), who solved the beam equation in combination with the full potential flow theory of Bollay (1939) (without taking the AR $\to 0$ limit) using a Hamiltonian framework. Their results show good agreement with the experimental measurements reported in Section 2.2. Interestingly, they studied the effect of a small non-zero initial curvature of the plate, which is applicable to all experimental measurements, and highlighted that the zero deflection equilibrium of those plates becomes unstable at finite velocity even for the AR$\to 0$ limit.

Chapter 3

EFFECT OF ANGLE-OF-ATTACK ON THE DYNAMICS OF AN INVERTED FLAG

Laboratory and numerical studies have highlighted the potential of exploiting the flapping motion of inverted flags for energy harvesting purposes (Kim et al., 2013; Ryu et al., 2015; Shoele and Mittal, 2016; Silva-Leon et al., 2019). Field realizations of the inverted flag energy harvester, however, have shown that frequent changes in flow direction, characteristic of atmospheric winds, result in reduced harvesting performance (Orrego et al., 2017). Changes in flow direction correspond to variations in the angle of attack of the undeflected flag, which modify its flapping dynamics. This undeflected angle of attack is equal to the angle between the clamping direction of the trailing edge and the direction of the flow and will be referred to as angle of attack for simplicity throughout this text, despite the fact that the instantaneous angle of attack of the flag changes constantly as it deflects. The dynamics of the inverted flag are very susceptible to changes in this angle, as can be deduced from the very different behaviors in the 90- and 180-degree limits. When the flow impinges perpendicularly to the plate, the plate behaves as a bluff body and the main force acting on it is drag, together with any unsteady forces that may arise. These forces can produce large bending deformations that often result in a more streamlined shape, reducing in turn the drag force that the flow exerts on the plate (Vogel, 1994). This phenomenon, named reconfiguration, has been widely studied and is commonly seen in vegetation, preventing breakage and uprooting among other things (De Langre, 2008). Conversely, in the case of a regular flag the flow remains attached and the force that acts perpendicularly to the plate, which is responsible for its bending, is due to lift. The resulting deflection of the plate can subsequently generate flow detachment and unsteady forces. Initially straight, the flag becomes unstable at flow speeds higher than a critical value that is a function of the flag's mass and flexibility (Shelley and Zhang, 2011).

Although these two limit cases have been studied thoroughly, very little information is known about the behavior of cantilever plates at intermediate angles of attack. Preliminary wind tunnel tests have been performed by Cossé et al. (2014) on an inverted flag of aspect ratio 2 at angles of attack of 0, 10 and 20 degrees. At finite α, the flag presented a gradual increase in the amplitude of motion as κ was increased, as opposed to the zero angle-of-attack case where the flag presents an abrupt increase in amplitude at a single value of κ. The critical κ at which the flag transitioned from the flapping to the deflected regime was found to be different for the three angles. Additionally, the flag at an angle of 20 degrees showed smaller maximum flapping amplitudes than those at smaller angles. This has been corroborated by brief computational studies by Shoele and Mittal (2016) and Tang et al. (2015), who observed the maximum flapping amplitude to decrease abruptly for angles larger than 15 degrees. Interestingly, Tavallaeinejad et al. (2018) studied the related problem of the presence of a small initial zero-stress deflection on the behavior of a small aspect ratio inverted flag clamped at zero degrees. The initial deflection causes the subcritical pitchfork bifurcation to be substituted by a saddle-node bifurcation. This results in the existence of a small deflection steady equilibrium.

While these results highlight some basic changes in the flag's dynamics, the literature lacks a more thorough characterization of the inverted flag's behavior at moderate angles of attack. The purpose of this study is to fully characterize the dynamics of an inverted flag for angles of attack between 0° and 28°, as well as to generate a more comprehensive experimental dataset of the phenomenon. Angles up to 28° have been considered because, as will be shown, the large-amplitude flapping regime disappears beyond that value for a plate of large aspect ratio. The main analysis is performed on a flag of aspect ratio 5 (flag 7, table 1.3). A flag of aspect ratio 2 (flag 8, table 1.3) is subsequently investigated to account for the variability of the results with aspect ratio. Additional measurements on flags of AR=2 and varying mass ratios were performed, but due to limitations in tunnel wind speed and dimensions the variation in μ is quite small. No significant changes were observed in the flag behavior with these small changes in mass ratio and, therefore, no detailed analysis of those flags is presented. Because experimental results on the inverted flag are limited in the literature and the problem has been used in the past as a benchmark for the validation of numerical codes, the obtained data is included in Appendix A as a reference.

3.1 Results

Behavior at zero angle of attack

The results obtained at zero angle of attack are consistent with the existing literature, with the three main dynamical regimes being clearly visible (Kim et al., 2013). Figure 3.1a shows the maximum, minimum and average deflection angle, Φ, for an inverted flag of AR=5 as a function of the square root of the non-dimensional

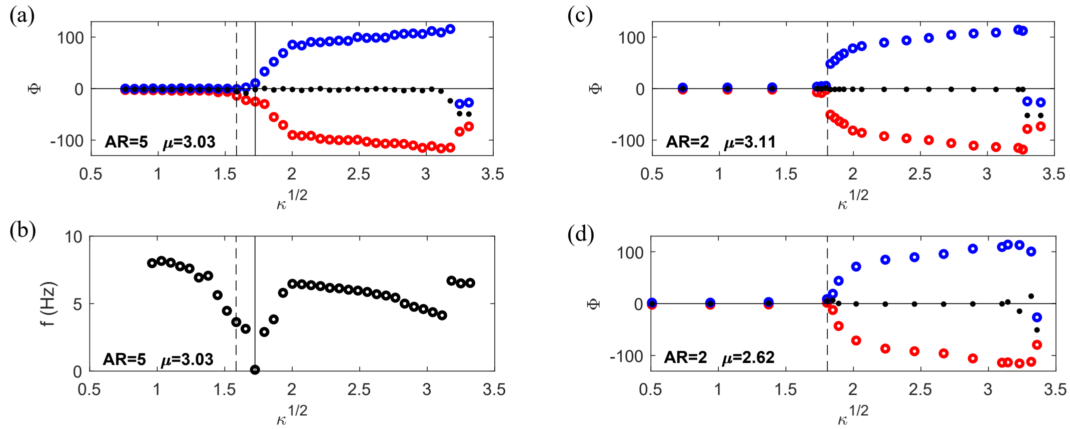

Figure 3.1: Behavior of an inverted flag at zero angle of attack. Maximum (○), minimum (○) and mean (●) deflection angle, Φ, for a flag of (a) AR=5 and $\mu = 3.03$, (c) AR=2 and $\mu = 3.11$ and (d) AR=2 and $\mu = 2.62$. (b) Frequency of motion of the flag of AR=5 and $\mu = 3.03$.

velocity, $\kappa^{1/2}$. At low flow speeds, the flag remains undeflected, undergoing a small amplitude oscillation. As wind speed is increased, it enters the flapping regime, exhibiting a symmetric large-amplitude flapping motion. For the highest values of κ, the flag flexes to the side, oscillating with relatively small amplitude around the deflected position.

As detailed in chapters 1 and 2, the transition from straight to flapping regimes has been proven numerically (Gurugubelli and Jaiman, 2015) and theoretically (Sader et al., 2016a) to be caused by a divergence instability of the zero deflection equilibrium. Figure 3.1b constitutes experimental proof of the existence of this divergence. It displays the frequency of motion of the flag examined in figure 3.1a as a function of non-dimensional wind speed. In the case of the small amplitude oscillations around the zero-deflection equilibrium characteristic of the straight regime, this frequency can be considered to be equal to the flag's natural frequency. In the presence of a divergence instability, the effective stiffness of the flag should asymptote to zero, with the natural frequency thus following the same trend. This is an argument equivalent to that used in Section 2.2. The trend can be clearly observed in figure 3.1b. The value of the oscillation frequency at $\kappa^{1/2} = 1.724$ is equal to $f = 0.1$Hz, indicating the proximity of the divergence point. This experimental value of the divergence velocity has been marked with a solid line in figures 3.1a and 3.1b. The theoretical value obtained using formula (2.10), $\kappa^{1/2} = 1.584$, is in reasonable agreement and is represented for reference with a dashed line.

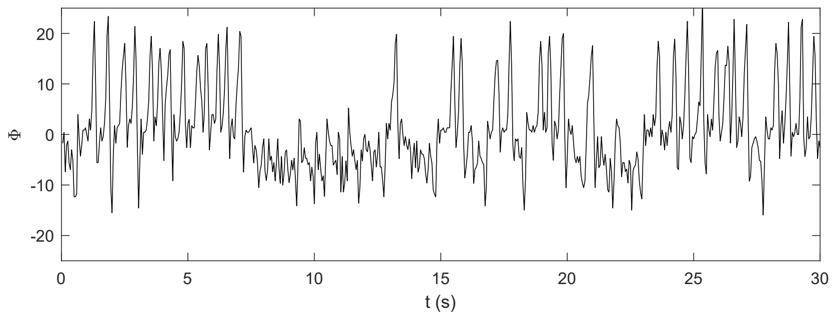

Figure 3.2: Time trace of the deflection angle for an inverted flag of AR=5 in the vicinity of its divergence instability ($\kappa^{1/2} = 1.724$, $f = 0.01$Hz).

As opposed to the results presented in previous experimental studies (Cossé et al., 2014; Huertas-Cerdeira et al., 2018; Kim et al., 2013), the amplitude of motion in figure 3.1a does not increase abruptly after the divergence instability. This discrepancy in post-bifurcation behavior is most likely due to small experimental differences, such as variations in the initial curvature of the flag and states of pre-stress that dampen the flag's motion and reduce its flapping amplitude for the lower velocities. To demonstrate that the discrepancy in post-critical behavior is neither caused by variations in aspect ratio or by variations in mass ratio with respect to the results of Kim et al. (2013), Huertas-Cerdeira et al. (2018) and Cossé et al. (2014), the maximum, minimum and average deflection angles for flags of $\mu = 3.11$ and $\mu = 2.62$ and AR=2 are presented in figures 3.1c and 3.1d, respectively. The experimental divergence velocity, $\kappa^{1/2} = 1.795$, and theoretical divergence velocity, $\kappa^{1/2} = 1.807$, of these flags are almost identical and are represented with a dashed line. Figure 3.1c exhibits a discontinuous jump in amplitude of motion after the divergence, while 3.1d exhibits a gradual increase. Because both flags correspond to the same aspect ratio, the differing behaviors cannot be caused by aspect ratio effects. Additionally, the mass ratio of all three flags is very similar, with the flag of AR=5 (figure 3.1a, $\mu = 3.03$) possessing a mass ratio that is closer to that of the flag presenting an abrupt transition (figure 3.1c, $\mu = 3.11$) than to that of the flag presenting a smooth transition (figure 3.1d, $\mu = 2.62$). It is therefore extremely unlikely that the discrepancy is caused by a mass ratio effect.

It is interesting to note that the amplitude of motion of the flag increases visibly as it approaches the divergence point from the lower velocities (figure 3.1a). This increase does not constitute an increase in oscillation amplitude but rather an increase in perturbation amplitude. As the divergence velocity is approached, the effective stiffness of the flag becomes lower, and therefore any perturbation will generate larger amplitude deviations. This is demonstrated in figure 3.2, where the time history of the deflection angle at $\kappa^{1/2} = 1.724$, corresponding to the measured velocity closest to the divergence, is plotted. The underlying small-amplitude low-frequency motion is visible. Superimposed are a number of peaks that correspond to the deviations caused by perturbations. They do not possess an inherent frequency and result in broadband noise in the FFT of the signal.

Behavior at finite angle of attack for AR=5

The experimental results obtained for an inverted flag of AR=5 at finite angles of attack are presented in figures 3.3, 3.4, 3.5 and 3.6. Figure 3.3 displays the maximum, minimum and average deflection angle as a function of non-dimensional velocity. Each subfigure corresponds to a different angle of attack, in 2° increments. The value of these angles is specified in the top left corner of each subfigure. Figure 3.4 follows a similar organization and shows the values of the amplitude A', which, as specified in Section 1.2, is calculated as the maximum between $A_{max} - A_{min}$ and $|A_{max}|$ and corresponds to the maximum cross-sectional area of the flag or distance between shed vortices. This parameter offers a reasonable comparison with the amplitude, A, employed in many existing studies, while adding information about the vortex street that is shed. Figure 3.5 shows, in a similar manner, the dimensional dominant frequency of the flag's motion, while figure 3.6 shows the Strouhal number $St = fA'/U$. The frequencies in these last two cases are calculated as the peak of the FFT of the deflection angle's time history. Data is presented only for velocities at which the FFT presented a clear peak. In certain cases, two distinct peaks are present; the largest peak was taken as the dominant frequency. Because the amplitude of these peaks is similar, small changes result in the switching of the dominant peak. This is reflected as a jump in the represented frequency. An example are the last four points of figure 3.5 at $\alpha = 6°$, whose FFTs are represented in the last four plots of figure 3.7.

The characteristics of the AR=5 flag's dynamics at these moderate angles of attack will be analyzed in the following sections. The case of the flag at an angle of attack $\alpha = 6°$ will be used as an example throughout, with similar general characteristics being present for all angles. The evolution of the flag's behavior with angle of attack will then be discussed in Section 3.1.

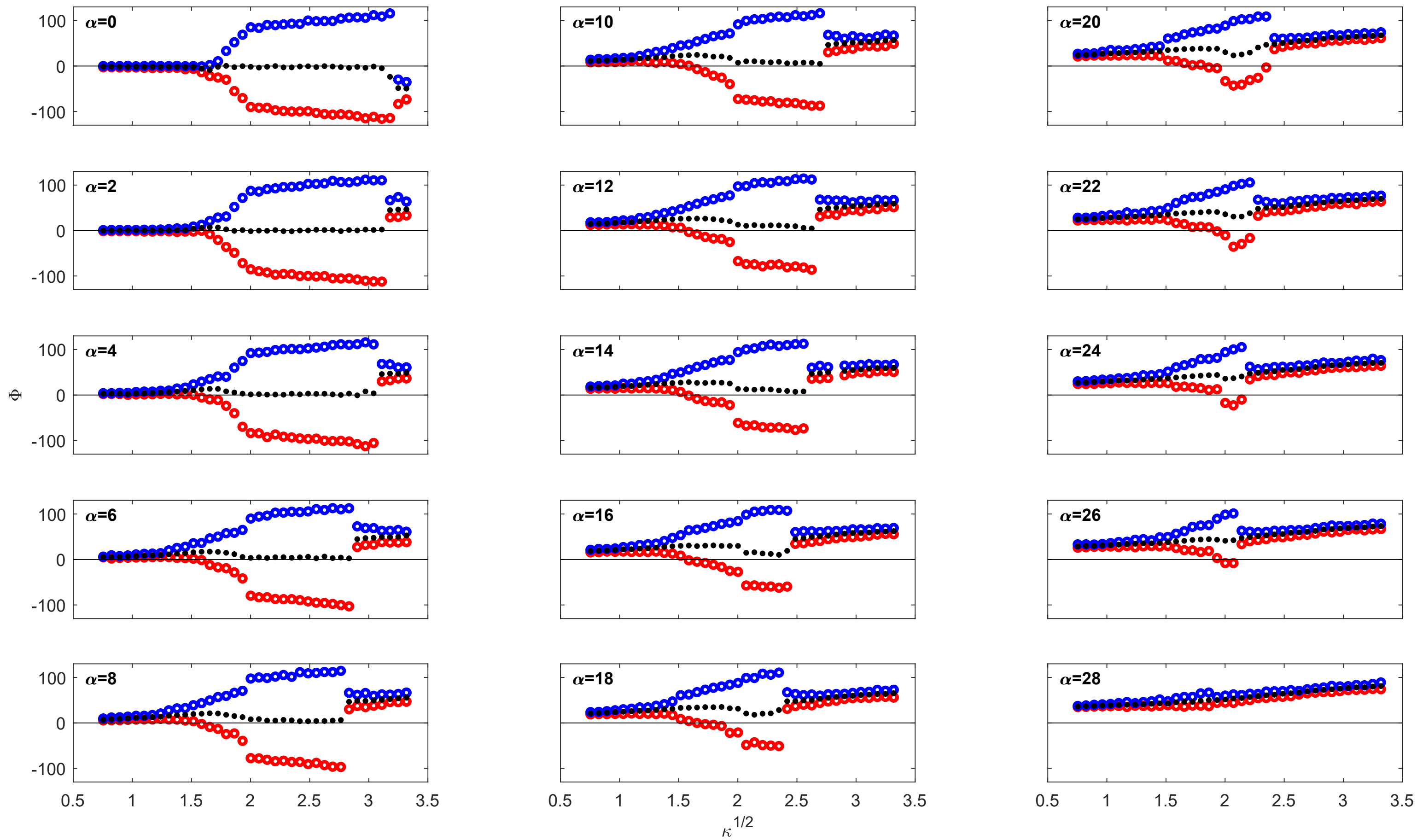

Figure 3.3: Maximum (○), minimum (○) and mean (●) deflection angle, Φ, for an inverted flag of AR=5 and $\mu = 3.03$ as a function of non-dimensional flow velocity, κ, and angle of attack, α

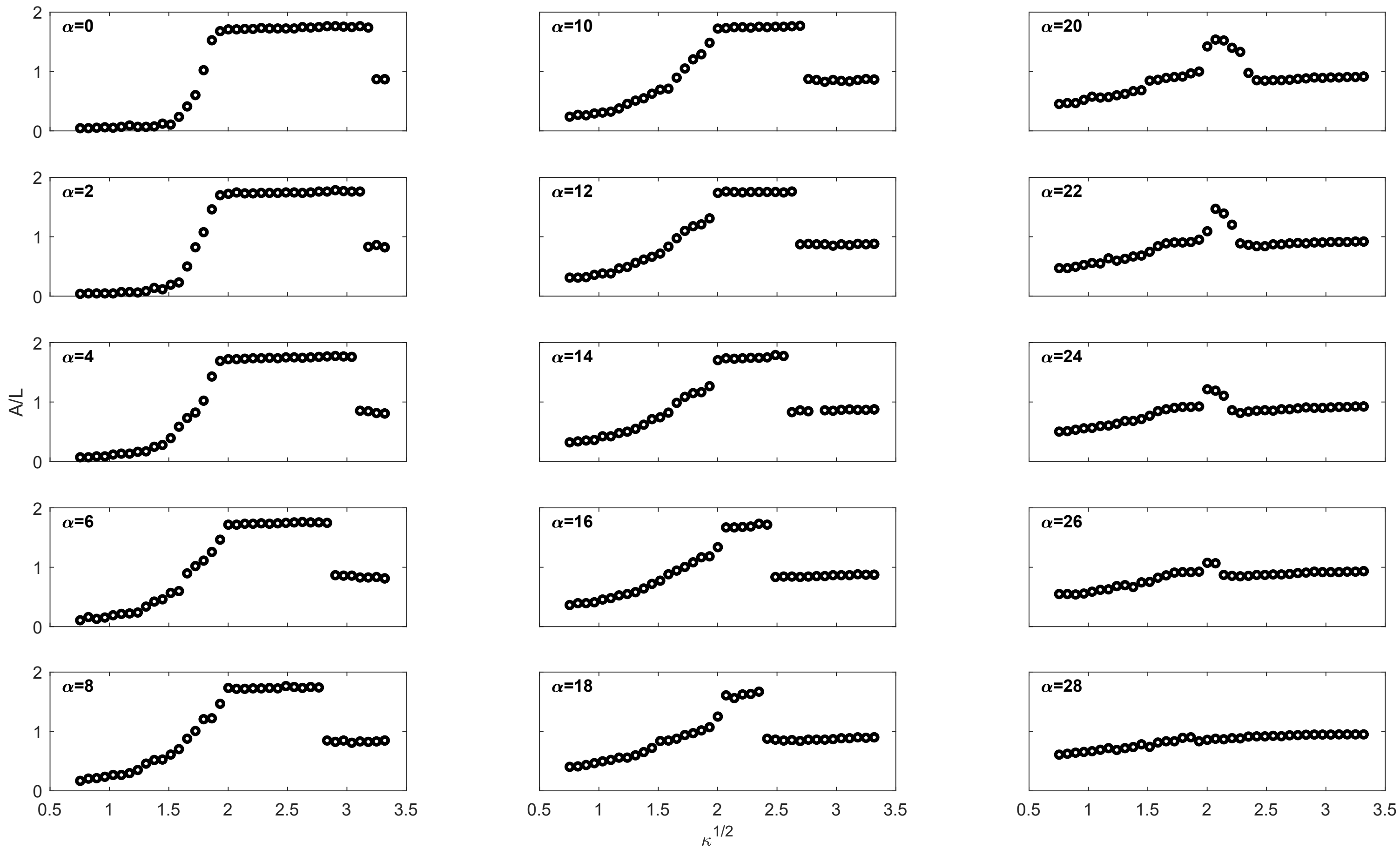

Figure 3.4: Maximum cross section, A', for an inverted flag of AR=5 and μ = 3.03 as a function of non-dimensional flow velocity, κ, and angle of attack, α

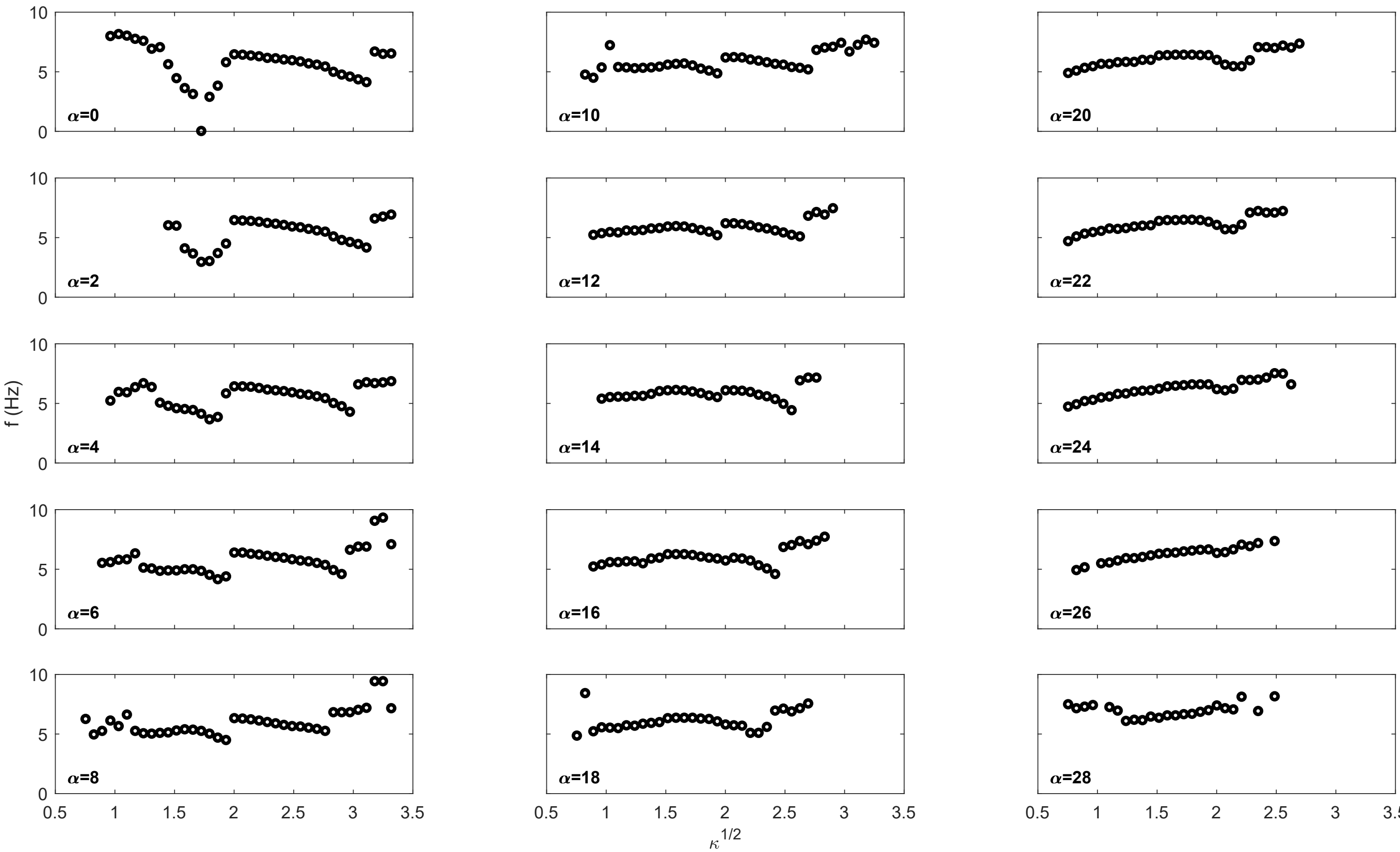

Figure 3.5: Frequency of motion, f, for an inverted flag of AR=5 and $\mu = 3.03$ as a function of non-dimensional flow velocity, κ, and angle of attack, α

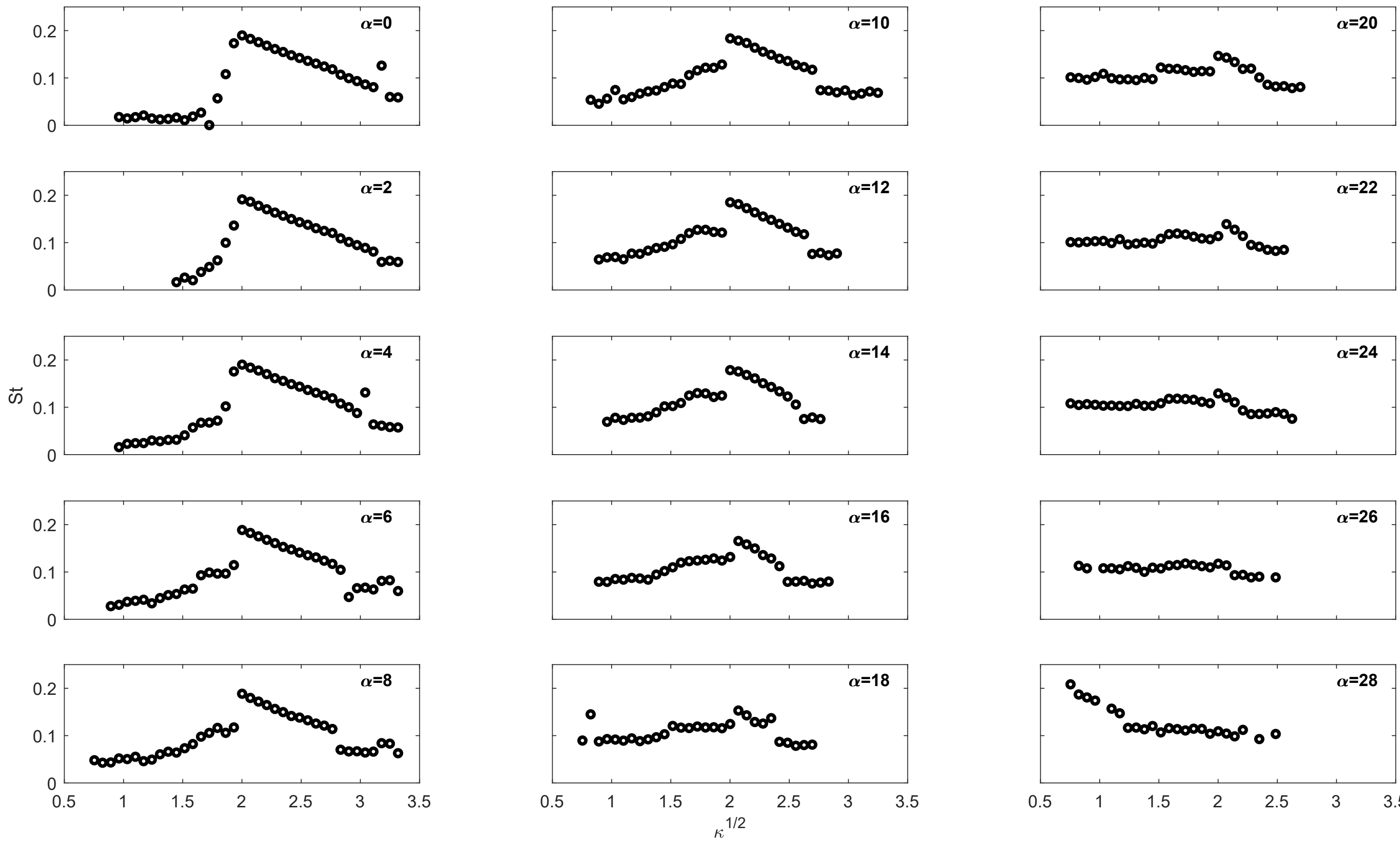

Figure 3.6: Strouhal number, $St = fA'/U$, for an inverted flag of AR=5 and $\mu = 3.03$ as a function of non-dimensional flow velocity, κ, and angle of attack, α

Deformed regime

As is expected, inverted flags clamped at finite angles of attack do not present a straight regime. For small values of κ, these flags undergo a small-amplitude oscillation around a small-deformation deflected equilibrium (figure 3.3). This regime will be denominated deformed in this text to make a distinction from the larger-deformation deflected regime. It is similar to the biased regime, that has been reported under several denominations in computational studies at zero angle of attack (Goza et al., 2018; Gurugubelli and Jaiman, 2015; Ryu et al., 2015) but is absent in the experimental literature. The lack of experimental observations may be due, however, to the difficulty of experimentally distinguishing between strictly zero and very small deflections as well as to the presence of small initial plate curvatures. The fundamental difference between deformed and straight regimes lies in the response to flow velocity of the equilibrium position around which the flag oscillates. In the case of the deformed regime, the deflection of this equilibrium increases with κ, remaining constant at $\Phi = 0°$ for all κ in the case of the straight regime. While inverted flags clamped at $\alpha = 0°$ transition from straight to deformed modes at a finite flow velocity (Gurugubelli and Jaiman, 2015; Ryu et al., 2015), flags at an angle of attack are inherently deformed for all flow speeds.

Although the dynamics of the inverted flag in the deformed regime are similar for all angles of attack, i.e., small oscillations around the deflected position (figure 3.3), the flow behavior exhibits significant changes. For small angles of attack ($\alpha \lesssim 10$) and low wind speeds, the deflection of the flag is small, and the flow remains attached. As wind speed is increased the deflection increases accordingly, reaching a critical value at which the flow separates. For the larger angles of attack ($\alpha \gtrsim 12$), the flow is separated for all wind speeds within the studied range. Flow separation results in modified lift and drag forces on the flag, modifying the equilibrium position around which the flag oscillates. The unsteadiness of the deflected flow, however, does not present a frequency similar to the natural frequency of the flag, and no large flapping is induced. The flow velocity, κ, at which the flow separates can be identified in figure 3.5. The small oscillations present in the deformed regime are caused by the flow unsteadiness from both turbulence and vortex shedding and occur at the effective natural frequency of the flag. This natural frequency is dependent on the damping produced by the flow. Because the aerodynamic forces are modified when flow separation occurs, the effective natural frequency, and consequently oscillation frequency, should present an abrupt change at the separation velocities. This jump can, effectively, be observed in figure 3.5 for $\alpha = 2° - 10°$ at low values of κ. The maximum deflection angle of the flag's oscillation for the flow speeds at which this jump occurs, κ_{sep}, is $\Phi = 8.8°,\ 9.8°,\ 13.0°,\ 12.4°$ and $15.1°$ at the angles of attack $\alpha = 2°,\ 4°,\ 6°,\ 8°$ and $10°$, respectively. These deflection angles are within the range expected for separation to occur. Variations in the separation deflection angle for different angles of attack may be caused by several factors, including the varying flow velocity and corresponding turbulence intensity at separation, the varying flag geometry resulting from the differing angle of attack and deformation mode shape, and experimental errors in both deflection angle and non-dimensional flow velocity.

The presence of a divergence instability, associated to the cessation of the straight regime, is no longer observed at finite angle of attack. As can be corroborated in figure 3.5, no decay to $f = 0$ of the oscillation frequency occurs. Instead, as κ is increased the amplitude of the flag oscillations begins to grow, and a large amplitude flapping motion develops. The nature of this flapping motion is analyzed in Section 3.1.

Flapping regime

The lack of a divergence instability and the gradual increase of the flag's oscillation amplitude pose a challenge in defining a critical transition velocity, κ_{lower}, from deformed to flapping regimes. The method proposed by Cossé et al. (2014) defines κ_{lower} as the speed at which the flag reaches an amplitude of motion that is a specified fraction of the maximum flapping amplitude. The selection of this fraction, however, is arbitrary, and variations in fraction result in significant changes in the value of the critical velocity. An alternate approach, based on the FFT of the flag's deflection angle, is suggested here. As an example, the FFTs of the motion of a flag at $\alpha = 6°$ and varying κ are shown in figure 3.7. The difference between flapping motions, where the FFT shows a crisp peak, and motions with no resonance, where the FFT appears noisy even if a peak is present, is distinguishable by eye. The flapping regime is therefore defined as the range of wind speeds at which these FFTs present a crisp peak. In order to mathematically define this region, a bi-Gaussian function is fitted to each FFT, normalized such that its maximum value is equal to one, and the sum of squares error (SSE) is calculated

$$SSE = \sum_{1}^{n} (y_i - \psi(f_i))^2 \tag{3.1}$$

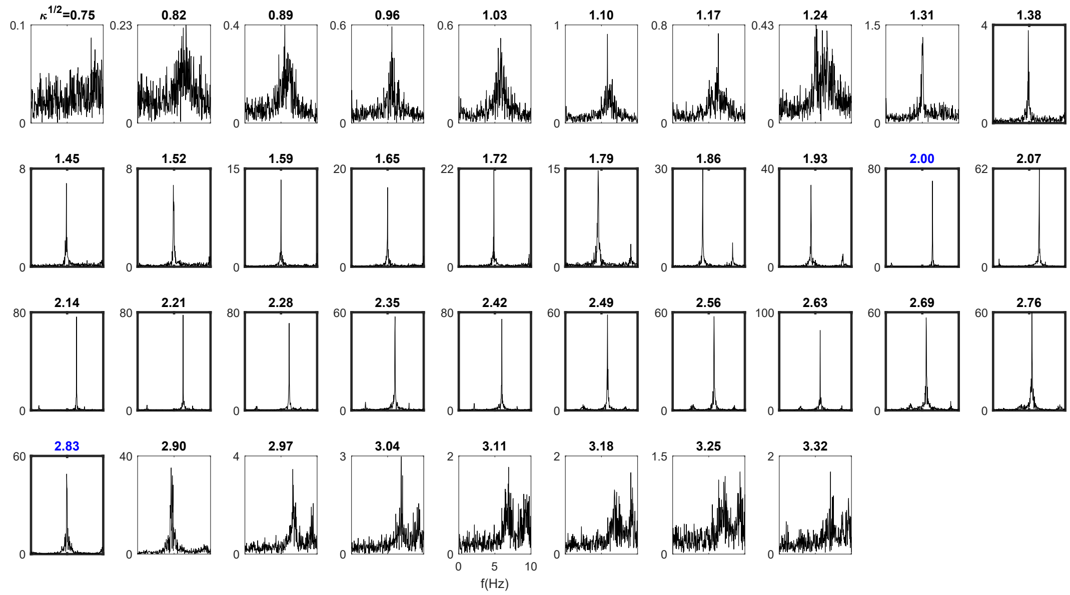

Figure 3.7: Power spectra of the inverted flag's motion for $\alpha = 6°$ and varying flow velocities. The velocities highlighted in blue correspond to the beginning and end of the upper branch large amplitude flapping motion. The velocities highlighted with a bold frame correspond to the flapping regime as defined by equation (3.2).

where n is the number of points in the FFT, y_i is the value of the FFT at the frequency f_i and $\psi(f_i)$ is the value of the fit at f_i. The SSE provides a measure of the dispersion of the function around the fit, which in this case is correlated to the dispersion or "noisiness" of the FFT. The value of the SSE obtained for the fits in the $\alpha = 6°$ case is plotted in figure 3.8a. The SSE displays a low-value plateau at the flapping velocities, with its value increasing in the deformed and deflected regimes. Consequently, the flapping regime has been defined as the range of κ at which

$$SSE\left(\frac{FFT}{max(FFT)}\right) < 1 \tag{3.2}$$

The FFTs corresponding to the flapping regime, as defined by equation (3.2), have been identified with a bold frame in figure 3.7. The limits of this flapping region are marked with black vertical lines in figure 3.8b, that illustrates the maximum, minimum and average deflection angle for the motion of the $\alpha = 6°$ flag. While the transition from deformed to flapping regimes is smooth, the transition from flapping to deflected regimes is well defined and corresponds to an abrupt decrease in the amplitude of motion. The limits defined by equation (3.2) capture this transition and the overall flapping region reasonably well. A single data point is present in figure

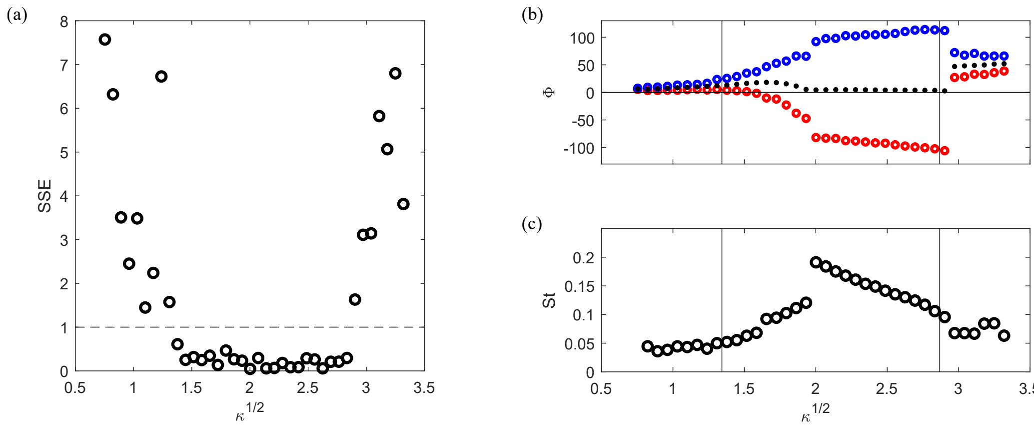

Figure 3.8: Definition of the flapping region for an inverted flag at $\alpha = 6°$ (a) SSE for a bi-Gaussian fit to the power spectra of the flag's motion (○) and threshold defining the flapping regime (-) (b) maximum (○), minimum (○) and mean (●) deflection angle, Φ, with limiting flow velocities for the flapping region (black lines) and (c) Strouhal number with limiting flow velocities for the flapping region (black line)

3.8b that shows a large-amplitude motion and is located beyond the limit established for the flapping range. This point corresponds to a bi-stable region, where both flapping and deflected motions are possible. This region will be studied in more detail in Section 3.1. The disparity in figure 3.8b is not coincidental; it stems from utilizing different data sets for the calculation of the SSE and the deflection angle and highlights the slight mobility of the defined upper critical velocity κ_{upper}. It is important to note that the threshold specified in equation (3.2) is relevant for the data employed in this chapter, but may need to be adjusted for different data sets depending on the noise level, frame rate employed and total number of frames acquired. It is, however, not arbitrary, unlike the maximum-amplitude fraction employed by Cossé et al. (2014), and is chosen such as to separate the existing plateau. Alternative approaches to identifying this flapping region are certainly possible, and a more rigorous approach may be developed as our knowledge of the underlying physics expands. The outlined procedure produces, however, reasonable results with the available data and large discrepancies should not be expected when utilizing alternative criteria.

The existence of two distinct regions within the flapping regime is easily recognizable from figure 3.8b and figure 3.8c, which displays the Strouhal number of the flag's motion for the same $\alpha = 6°$ flag. The first region will be denominated lower branch and is present between $\kappa_{lower}^{1/2} < \kappa^{1/2} < 2$ in figures 3.8b and 3.8c. The second region, which will be denominated upper branch, lies between $2 < \kappa^{1/2} < \kappa_{upper}^{1/2}$. The two regions are separated by an abrupt shift in amplitude and Strouhal number.

The upper branch corresponds to the large-amplitude flapping motion present at zero angle of attack and thoroughly described in the inverted-flag literature. It possesses all of the traits characteristic of a vortex-induced vibration, as established by Sader et al. (2016a). The peak Strouhal number occurs at $\kappa^{1/2} = 2$ and is between St=0.19–0.18 for angles up to $\alpha \approx 15°$, decreasing rapidly for larger angles of attack (figure 3.6). These values are characteristic of lock-on in VIVs, marking the synchronization of vortex shedding, oscillation frequency and natural frequency. In this upper branch the angular deflection, $\Delta\Phi$, increases with flow speed, but the amplitude A' is roughly constant as a result of the problem's geometry (figure 3.4), with increased deflections resulting in the flag bending backwards. The frequency decreases slightly as flow speed is increased, as is characteristic of vortex-induced vibrations in heavy fluid loading. As a result the Strouhal number decreases practically linearly as wind speed is increased, until the shedding frequency reaches values disparate enough from the flag's natural frequency that the lock-on is lost (Goza et al., 2018).

The lower branch, on the other hand, exhibits notably different features. The Strouhal numbers within this branch vary between St=0.02 and St=0.13. They show a significant increase as flow speed is raised as a result of the comparably rapid increase in amplitude. Neither of these characteristics are indicative of a vortex-induced vibration. A different resonant phenomenon must therefore be the underlying cause of the large-amplitude flapping motion. The FFTs of the flag's motion for velocities in the deformed regime, leading to the appearance of the lower branch, are visible in figure 3.7 for the $\alpha = 6°$ case. They present a single peak that increases in amplitude as the critical velocity κ_{lower} is approached. For the highest angles of attack ($\alpha > 20$), two peaks are present (not pictured here), however, they do not approach each other, with a single peak increasing in amplitude as the lower branch is neared. The lack of a second coalescing peak makes the presence of a coupled-mode flutter instability unlikely. Additionally, it is interesting to note the behavior of the minimum deflection angle throughout the velocity range corresponding to this branch (figures 3.8b and 3.3). At the lower velocities, the minimum deflection is positive, albeit small, and the flag does not surpass the zero deflection position. For the larger velocities, on the other hand, the minimum deflection reaches relatively large negative values. As an example, the highest and lowest minimum deflections at $\alpha = 6°$ are $\Phi = 3°$ and $\Phi = -50°$, respectively. It therefore seems reasonable to assume that the shedding of vorticity and resulting wake are qualitatively very different for different velocities within the lower-branch range. This would eliminate the synchronization between the flag's natural frequency and the frequency of the unsteady fluid forcing as a probable driving mechanism. These observations point in the direction of a single-mode galloping instability. Figure 3.9a shows the lower critical velocity at which the lower branch develops (green triangle) together with the separation velocity (black triangle) for all angles of attack. It demonstrates that at the emergence of the lower branch the inverted flag always sees separated flow and thus the quasi-steady forcing on the flag is non-linear. It is therefore possible that the lower branch is the result of a stall-flutter mechanism. Further investigations, however, are necessary to unequivocally characterize the nature of this instability. It should be highlighted that the flags at high angles of attack ($\alpha > 16$) present a discontinuity in flapping amplitude and frequency at a constant value of $\kappa^{1/2} \approx 1.5$, which may indicative of a transition to a different driving mechanism within the lower branch.

Deflected regime

The fluid damping on an inverted flag that is flapping within the upper branch grows with increasing flow speed, reducing the flag's effective natural frequency. When the value of this natural frequency is disparate enough from the vortex shedding frequency, the flag's motion ceases to lock-on to the vortex shedding frequency and the large-amplitude flapping motion disappears, giving rise to the deflected regime. This lock-off occurs at $St \simeq 0.08$ for the smallest angles of attack ($\alpha \leqslant 4$) and at $St \simeq 0.11$ for the larger angles (figure 3.6). Between flapping and deflected regimes, a bi-stable region, where either regime is possible, was observed. In certain cases, the position of the flag was either flapping or deflected depending on initial conditions, while in other cases the flag switched randomly from one mode to the other, resulting in the chaotic regime that has been reported for inverted flags at zero angle of attack (Goza et al., 2018; Sader et al., 2016a). This bi-stable region was only observed to exist at small angles of attack $\alpha \lesssim 8°$ and occurred for a narrow band of flow velocities.

The critical velocity, κ_{upper}, at which the flag enters the deflected regime, decreases with angle of attack (figure 3.3). An interesting observation was made by Cossé (2014): independently of angle of attack, the inverted flag shows a similar shape at the emergence of the deflected regime. This is quantitatively corroborated in

α (°)	$\bar{\Phi}_{def}$ (°)
0	48.5
2	44.8
4	46.0
6	44.8
8	46.6

α (°)	$\bar{\Phi}_{def}$ (°)
10	46.6
12	46.2
14	46.8
16	45.3
18	47.7

α (°)	$\bar{\Phi}_{def}$ (°)
20	48.5
22	47.9
24	47.3
26	47.1
Mean	46.7 ± 1.2

Table 3.1: Mean deformation angle of the inverted flag at the emergence of the deflected regime

the present measurements. Table 3.1 shows the average deflection angle, $\bar{\Phi}$ at the wind speed at which the flag first enters the deflected regime. The value of this average deflection is virtually constant, with an average of $\bar{\Phi} = 46.7°$ and a standard deviation of $\sigma = 1.2°$. No trend is visible within these small variations.

The velocity, κ_{def} at which the flapping regime ends is plotted in figure 3.9a together with the velocity at which the synchronized motion ceases, κ_{upper}, as defined by equation (3.2). In this case both velocities correspond to the same dataset, eliminating any disparities due to the bi-stable nature of the flag in this region. For most angles of attack, both velocities coincide; within the region $\alpha = 15° - 20°$ synchronization is lost before the flag enters the deflected regime. This is reminiscent of the result obtained by Goza et al. (2018), who reported large-amplitude flapping without classical VIV for the highest velocities within the flapping range for the zero angle-of-attack case. Interestingly, the FFT of the flag's motion (figure 3.7) transitions from presenting a single dominant peak in the deformed and flapping regimes to presenting two clear peaks in the deflected regime. The frequency of the second peak, however, is too low to correspond to the vortex shedding frequency, but may correspond to subharmonics of the unsteady fluid forces.

Evolution with angle of attack

The three main dynamical regimes present in the motion of inverted flags at moderate angles of attack (deformed, flapping and deflected) have been analyzed in detail in the previous sections. Figure 3.9a displays the range of flow velocities at which each regime occurs for the different angles of attack, with κ_{lower} (green triangle) marking the transition from deformed to flapping regime and κ_{def} (black rhombus) marking the transition from flapping to deflected regime.

For angles of attack up to $\alpha = 14°$ the lower critical velocity decreases practically linearly as α is increased. Between $14° < \alpha < 22°$ this velocity remains mostly

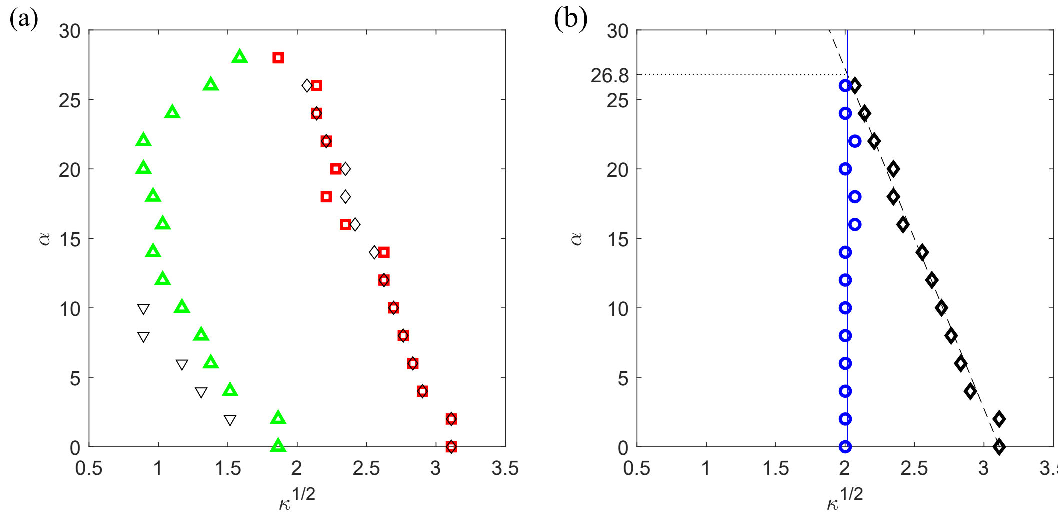

Figure 3.9: Critical non-dimensional flow velocities as a function of angle of attack (a) Separation velocity, κ_{sep} (∇), beginning of resonance, as defined by equation (3.2), and flapping regime, κ_{upper} ($\triangle$), end of resonance, κ_{lower} ($\square$), and deflection velocity, κ_{def} ($\diamond$). (b) Beginning of upper branch (VIV) flapping ($\circ$) and deflection velocity ($\diamond$) with linear fits.

constant to subsequently rapidly increase for angles $\alpha > 22°$. This variation in trend may be caused by changes in the underlying mechanisms behind the flapping motion for varying angles of attack. Further understanding of these underlying mechanisms, however, is required to clarify this behavior. The deflection velocity, κ_{def}, decreases with angle of attack, most likely due to the increased flow damping exerted when flags are at larger angles to the flow. This decrease is surprisingly linear with angle of attack. Even more surprisingly, the velocity at which the flag enters the upper branch of the flapping regime (VIV) is constant for all α, at a value of $\kappa^{1/2} = 2$.

The flow velocities at which the upper-branch vortex induced vibration is initiated and terminated are plotted in figure 3.9b, together with linear fits to the data. Because the starting velocity is constant and the ending velocity decreases with angle, at a specific angle of attack both velocities become equal and the upper-branch disappears. The value of this angle, calculated utilizing the linear fits, is $\alpha = 26.8°$ for the flag studied. Effectively, at angles larger than this value, such as $\alpha = 28°$ represented in figures 3.3, 3.4, 3.5 and 3.6, this motion is no longer present. The lower-branch flapping motion is present at angles beyond this value, but not significantly higher. For $\alpha \approx 28°$ the lower and upper critical velocities meet, and the flapping regime ceases to exist overall (figure 3.9a). At these angles the deformed and deflected regimes merge into a single common regime, where the flag flexes with continuously increasing deflection angle and oscillates with small amplitude around this position.

At any given free-stream velocity within the upper branch, the angular amplitude of motion of the flag remains approximately constant with angle of attack for angles $\alpha \leqslant 14°$, with the amplitude decreasing rapidly for angles beyond that value (figure 3.3). This result is in agreement with the threshold obtained by Shoele and Mittal (2016), who observed the amplitude of motion to notably decline for angles beyond $\alpha = 15°$. Because the maximum angular amplitude occurs at the highest flow velocity before deflection and the value of this velocity decreases with angle of attack, the overall maximum angular amplitude decreases with angle of attack for all angles. The Strouhal number follows a similar trend, diminishing rapidly for angles beyond $\alpha = 14°$ (figure 3.6). The energy harvesting performance of the inverted flag is therefore severely limited beyond this value, both due to the decrease in the flapping amplitude and the decrease in range of velocities at which flapping occurs.

Behavior at finite angle of attack for AR=2

The experimental measurements performed in Section 3.1 for an inverted flag of aspect ratio AR=5 were reproduced for a flag of AR=2. The results are presented here, with the objective of highlighting the most prominent differences. The obtained data is presented in a similar manner: the maximum, minimum and mean deflection angle, Φ, is shown in figure 3.10, the cross section amplitude, A’ , in figure 3.11, the frequency, f, in figure 3.12 and the Strouhal number, St, in figure 3.12. The corresponding values for the AR=5 flag are included for comparison in these figures.

The three main dynamical regimes present in the motion of the flag of AR=5 (deformed, flapping and deflected) can be recognized in the motion of the AR=2 flag. At low flow velocities, the flag oscillates around a small deflection equilibrium. In this case, the power spectra of the motion present two clear peaks, that may be indicative of the effect of the second length scale (height, H). These two frequencies are visible, for example, at the lower velocities of the $\alpha = 2°$ case in figure 3.12, where the jump between two frequency levels corresponds to the switching of the dominant peak. The flow detachment velocity is no longer visible at small angles of attack, which suggests lower detachment velocities that are not within the evaluated range. The transition to the flapping regime occurs in a similar manner to the higher aspect ratio case, with the lower of the two frequency peaks growing in amplitude and no coalescence of peaks being observed.

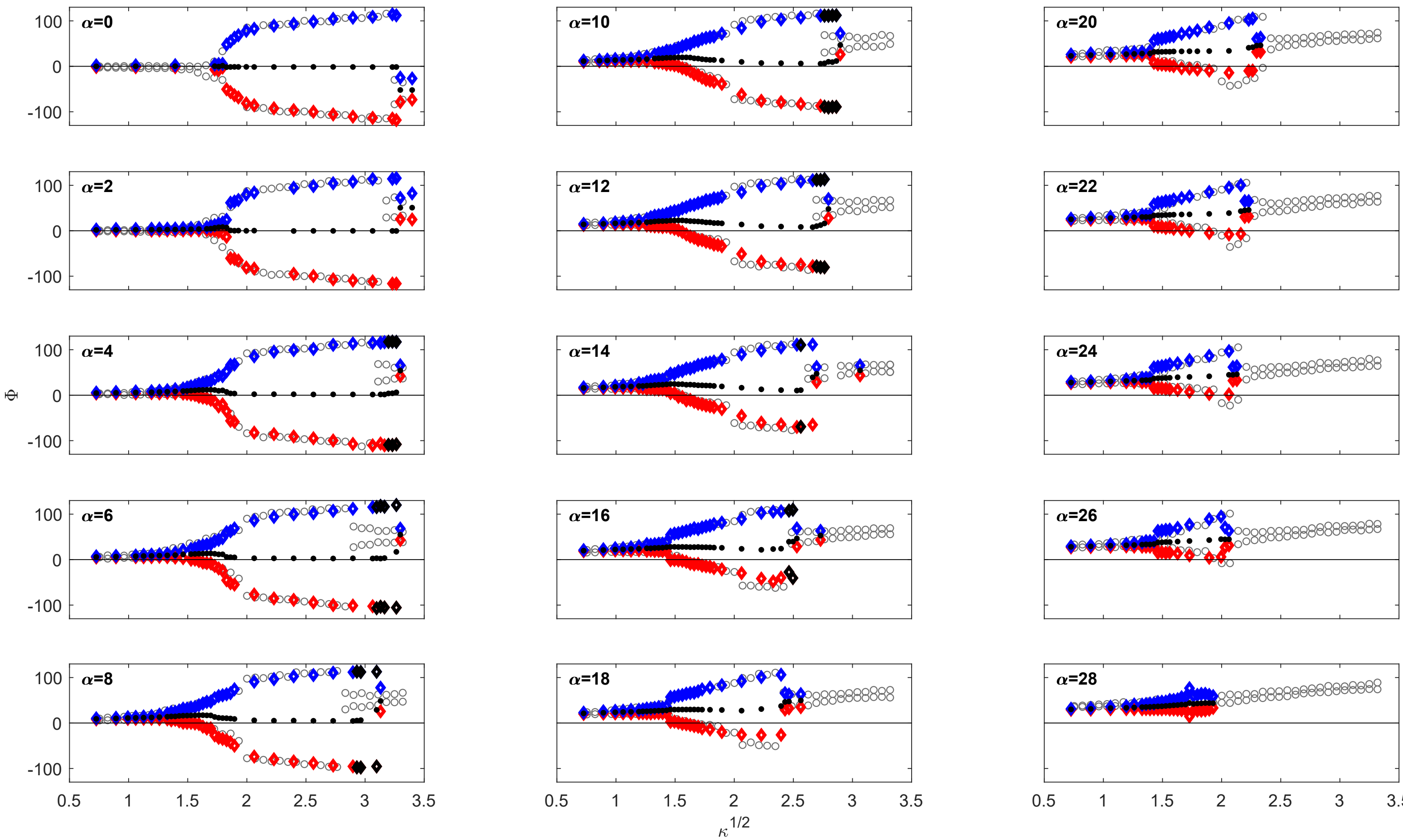

Figure 3.10: Maximum (◇), minimum (◇) and mean (●) deflection angle, Φ, for an inverted flag of AR=2 and $\mu = 3.11$ as a function of non-dimensional flow velocity, κ, and angle of attack, α. Maximum and minimum deflection angle for an inverted flag of AR=5 (○).

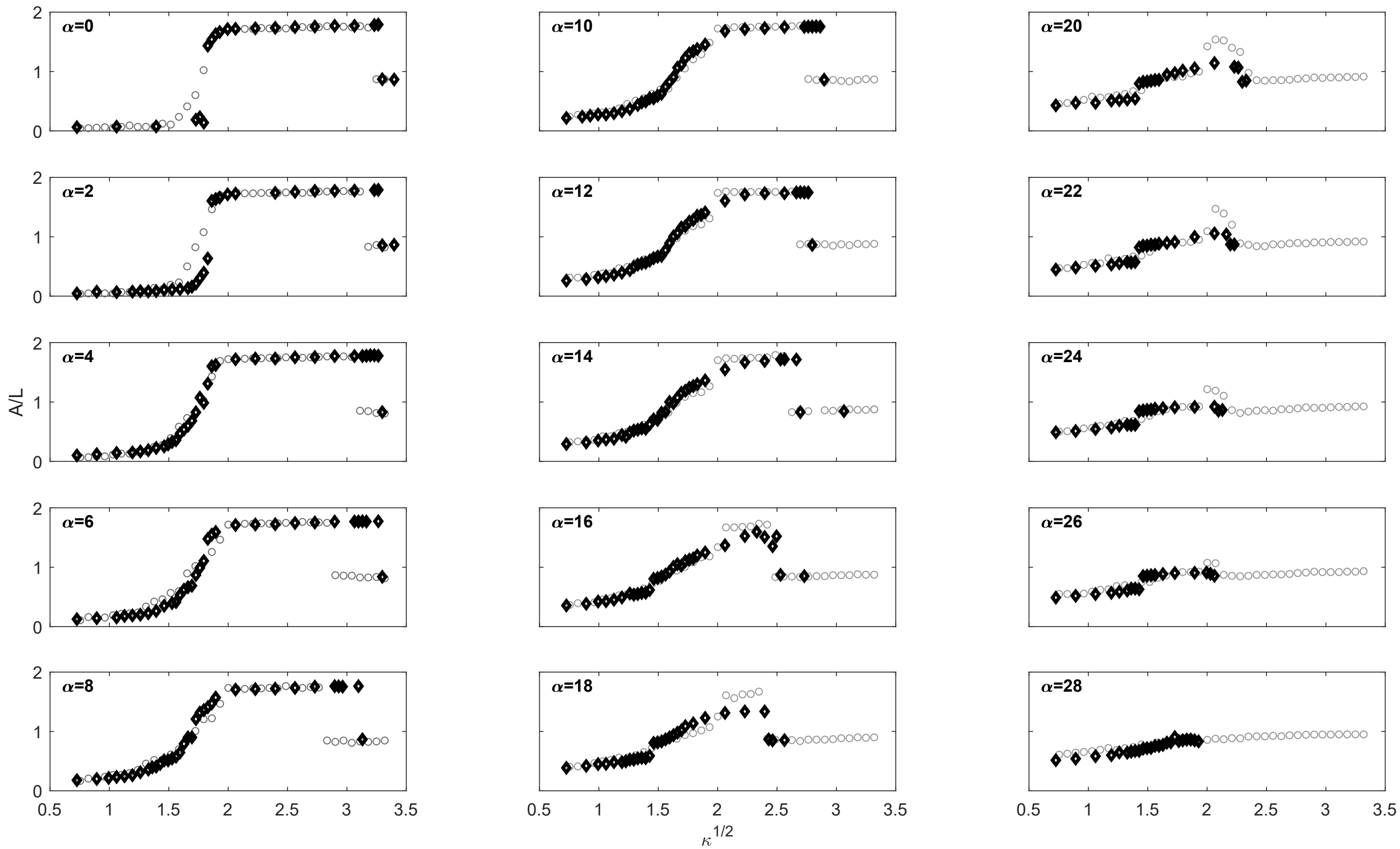

Figure 3.11: Maximum cross section, A'(◇), for an inverted flag of AR=2 and μ = 3.11 as a function of non-dimensional flow velocity, κ, and angle of attack, α. Maximum cross section for an inverted flag of AR=5 (○) for reference.

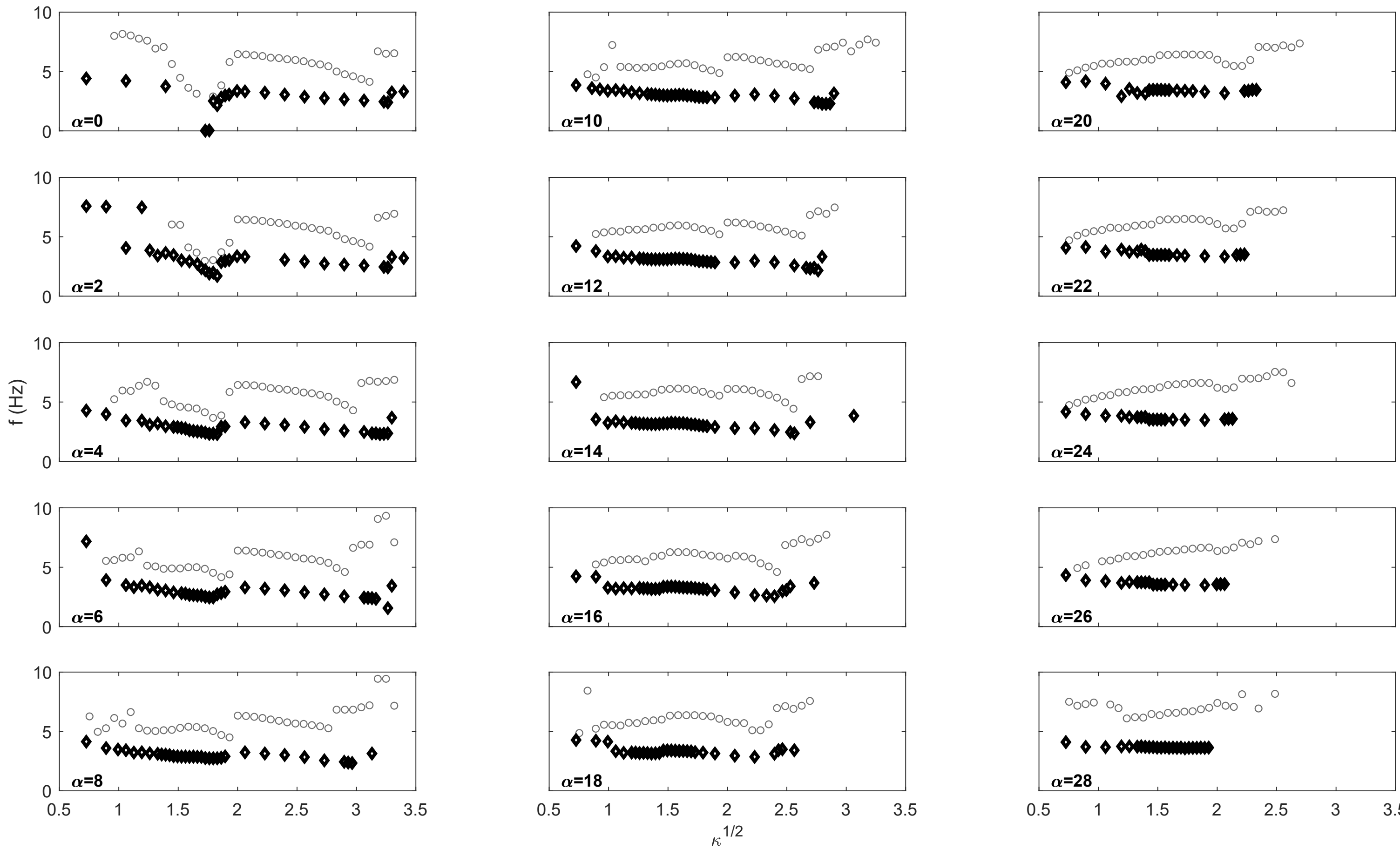

Figure 3.12: Frequency of motion, f (◇), for an inverted flag of AR=2 and μ = 3.11 as a function of non-dimensional flow velocity, κ, and angle of attack, α. Frequency of motion for an inverted flag of AR=5 (○) for reference

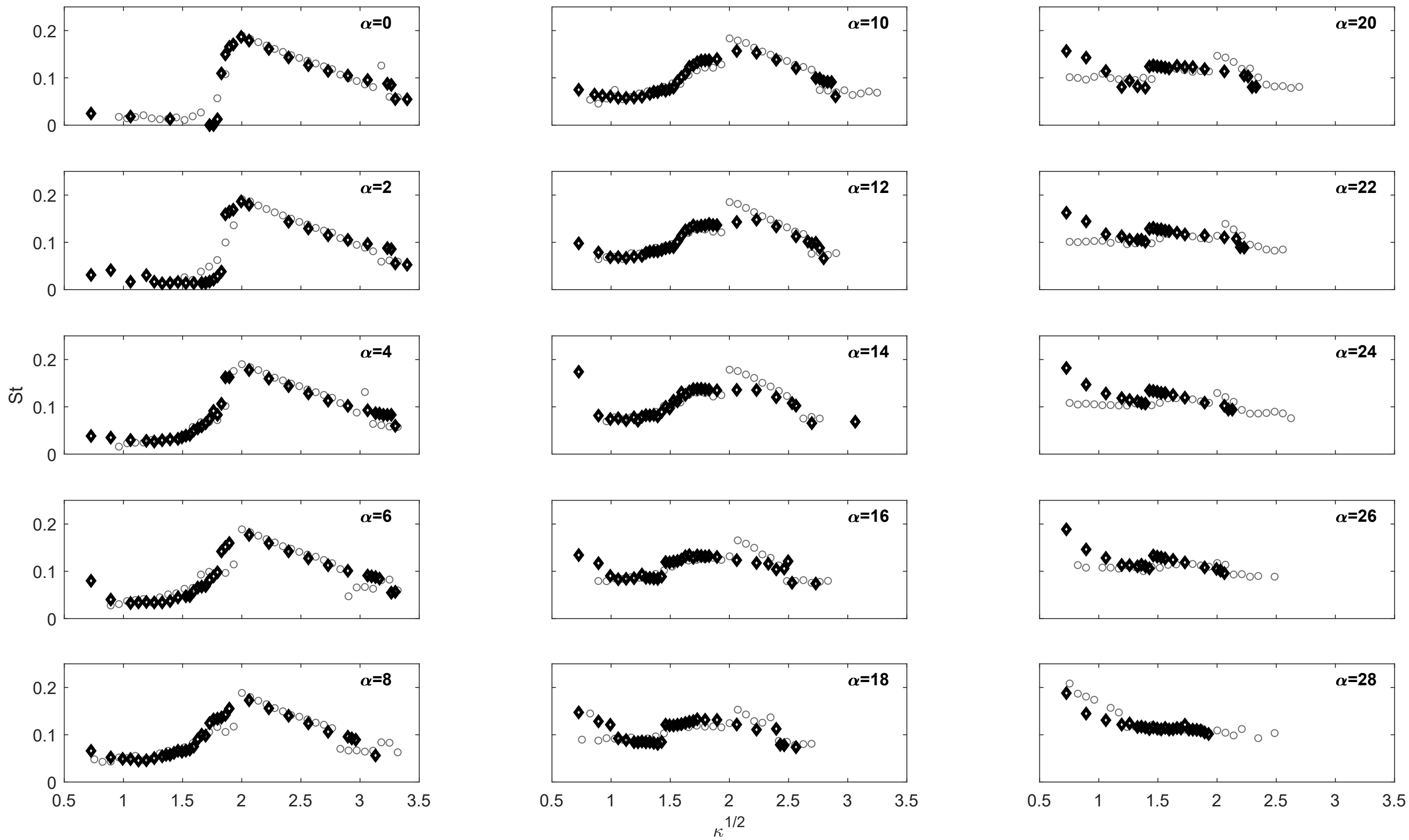

Figure 3.13: Strouhal number, $St = fA'/U$ ($\diamond$), for an inverted flag of AR=2 and $\mu = 3.11$ as a function of non-dimensional flow velocity, κ, and angle of attack, α. Strouhal number for an inverted flag of AR=5 ($\circ$) for reference.

The behavior of the flag in the flapping regime presents notable differences, with the existence of two distinct branches being no longer evident at most angles of attack. An abrupt increase in amplitude of motion and Strouhal number is present for the lower angles of attack ($\alpha \leqslant 6$), but no longer occurs at the flow speed at which the St value is maximum (figures 3.10 and 3.13). The Strouhal number slightly increases to then decrease linearly within the upper branch, with the flow velocity at which the Strouhal peaks being surprisingly equal for both aspect ratios ($\kappa^{1/2} \approx 2$). For higher α, however, all variables vary smoothly within the flapping regime, eliminating the distinction between the two branches. The absence of a marked upper branch results in lower amplitudes in the flapping motion for $\alpha > 8°$, with the difference in minimum deflection angle being particularly significant. The discrepancy initially occurs at the lower flow velocities exclusively, but extends to the full range for $\alpha > 14°$. The lowered amplitude of motion results in lower Strouhal numbers, making the underlying mechanism behind the flag's motion uncertain. Further investigation of this motion is necessary to clarify the flag's behavior and may reveal the existence of different branches that cannot be distinguished in the current data. The flag of AR=5 presented an additional discontinuity at a flow velocity of $\kappa^{1/2} \approx 1.5$ for angles $\alpha > 16$. Remarkably, this discontinuity is present at the same threshold and flow velocity in the AR=2 case.

The presence of a chaotic regime was also observed in the motion of the AR=2 flag, occurring at a larger range of flow velocities than the higher aspect ratio case. The data points corresponding to the chaotic region have been highlighted in black in figure 3.10. The velocity at which the flapping regime ceases to be present follows a linear trend with angle of attack, with, however, a more pronounced slope, that may be a result of variations in flow damping with aspect ratio. In this AR=2 case, the disappearance of the upper branch is associated to the decreasing deflection velocity, and therefore cannot be calculated in a similar manner. The full flapping motion, however, is practically non-existent at an angle of attack of $\alpha = 28°$.

An angle of attack of $\alpha = 30°$ was investigated in addition to those present in figures 3.10–3.13 and is presented in figure 3.14. Interestingly, a new resonant motion is clearly present. At the lower flow velocities, the power spectra of the motion show the existence of two peaks, which approximate each other as the large-amplitude motion is onset. This suggests the presence of a coupled-mode flutter mechanism. The nature of this motion is therefore distinct from that of the flapping motion analyzed throughout this chapter, and lies beyond the scope of this text. It

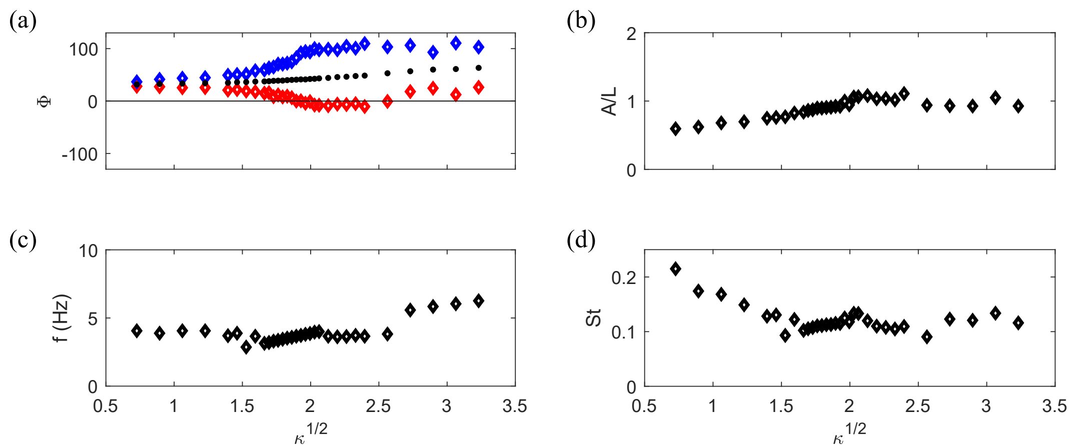

Figure 3.14: Behavior of an inverted flag of AR=2 at $\alpha = 30°$. Maximum (◇), minimum (◇) and mean (●) deflection angle, Φ, (b) maximum cross-section, A', (c) frequency of motion, f, and (d) Strouhal number, St

highlights, however, the variety of phenomena that may arise at angles of attack intermediate to the typically studied $\alpha = 0°,\ 90°$ and $180°$, that may be of interest in future investigations.

3.2 Conclusions

This chapter has analyzed the effect of moderate angles of attack on the dynamics of an inverted flag. A flag of AR=5 was first investigated and showed results consistent with the existing literature at zero-angle-of attack, where the presence of a divergence instability was established experimentally for the first time. Three distinct dynamical regimes were identified at finite angles of attack: deformed, flapping and deflected. These correspond to small oscillations around a small deflection equilibrium, large-amplitude oscillations and small oscillations around a large deflection equilibrium, respectively. A new method that determines regions of resonance based on the power spectra of the motion was proposed as a means of identifying the initiation and cessation velocities of the flapping regime.

Unlike in the zero angle-of-attack case, the deformed state does not lose its stability through divergence. Instead, it was hypothesized that a galloping type instability gives rise to what has been denominated the lower branch of the flapping regime. At a constant non-dimensional flow velocity $\kappa^{1/2} = 2$ a second distinct branch within the flapping regime develops. This upper branch corresponds to the large-amplitude flapping motion that has been observed for the inverted flag at zero angle of attack and has been determined to be a vortex-induced vibration. As flow speed is increased, the flag transitions to the deflected regime. The velocity at which this transition occurs decreases linearly with angle of attack, while the velocity at which the upper branch flapping is onset remains constant. This results in both velocities coinciding at an angle of attack of $\alpha = 26.8°$, beyond which the upper flapping branch ceases to exist. The entirety of the flapping motion further disappears at angles beyond $\alpha \approx 28°$.

A subsequent set of tests was performed on a flag of aspect ratio AR=2 and revealed contrasting dynamics. Although the three main dynamic regimes are still present, the distinction between lower and upper flapping branches is no longer evident. As a result, the angular amplitude of motion in the flapping regime is fairly decreased for angles of attack above $\alpha = 8°$.

Chapter 4

COUPLED DYNAMICS OF TWO SIDE-BY-SIDE INVERTED FLAGS

Cecilia Huertas-Cerdeira, Boyu Fan, and Morteza Gharib. Coupled motion of two side-by-side inverted flags. *Journal of Fluids and Structures* 46:527–535,2018.

While chapters 2 and 3 aim to improve our understanding of the dynamics of a single inverted flag, energy harvesting devices do not typically consist of an isolated flag, but of an array of them. Understanding the interaction between flags is essential to predicting the energy harvesting performance of the system. Indeed, arrangement optimization is a full field of study in the development of traditional turbine wind farms (Samorani, 2013). It is particularly relevant, however, in turbines that rely on vortex dynamics to function, such as the inverted flag, because vortex wakes can interact strongly when in proximity.

The canonical problem studied in the fields of vortex shedding and vortex induced vibrations is that of a circular cylinder (for a review, see Williamson and Govardhan (2004)). The interaction between multiple cylinders placed in different arrangements has been reported extensively in the literature. In particular, interesting wake dynamics have been shown to arise when two fixed stationary cylinders are immersed side-by-side in a flow (Zdravkovich (2003) and references therein). Depending on the separation between them, they have been shown to generate either a single vortex street, two wakes of different widths that present a bi-stable gap flow, two equal and synchronized wakes or two completely uncoupled wakes. In the case of cylinders that are flexible or allowed to move the coupling of the wakes can result in the coupling of the motion of the cylinders (Huera-Huarte and Gharib, 2011; Liu et al., 2001; Zdravkovich, 1985; Zhou et al., 2001).

Similarly, two conventional flags placed side-by-side in a flow have been shown to interact. Zhang et al. (2000) experimentally studied the motion of two side-by-side filaments immersed in a soap film and observed both an in-phase flapping mode for small flag separations and an anti-phase flapping mode for larger flag distances. The anti-phase mode was observed to oscillate with frequencies 35% higher than those of the in-phase mode. As the distance was further increased, the interaction weakened and the flags moved independently. Analogous results were obtained in numerical simulations by Zhu and Peskin (2003) and Farnell et al. (2004). Farnell et al. (2004), Si-Ying et al. (2013) and Sun et al. (2016) observed, in addition to the in-phase and out of phase modes, the existence of a transition mode where the frequencies of both motions co-exist. A different transition mode was reported by Jia et al. (2007), who observed a region where in-phase and out-of phase flapping alternate randomly. In addition to two equal filaments, Jia et al. (2007) studied the motion of two side-by-side filaments whose length varied by a factor of two and observed synchronization with a scattering of the phase around the 0 and π values.

These interactions with neighboring flags and their vortex streets can cause variations in the forces experienced by the flags. Many natural organisms exploit the vortex street of neighboring bodies to enhance their performance; an example is schooling fish. Changes in position and phase between the swimming motion of adjacent fish can drastically change the effect of schooling (Weihs, 1973). Inspired by this behavior, optimal arrangements of vertical axis wind turbines have been shown to increase energy extraction in wind farms (Whittlesey et al., 2010). Dong et al. (2016) showed that placing two flags side-by-side can produce increased energy extraction efficiency in a potential energy harvesting mechanism. It is expected that inverted flags will show a similar behavior, and placing several flags in close proximity may enhance their energy harvesting capabilities.

In this chapter, the coupling of the motion of two inverted flags in a side-by-side arrangement is investigated experimentally. Because the amplitudes of oscillation of the inverted flag vary greatly between the different regimes of motion (straight, flapping and deflected), the effective cross-sectional area of the flag undergoes significant changes between them. This causes the synchronization in the motion of the flags to occur at very different flag separations for the different regimes. In this study we have focused on distances at which the flags never collide ($1.7 < T/L < 5.4$), which are pertinent to the coupling of the vortex induced vibrations of the flags in the flapping and deflected regimes. Here, T corresponds to the cross-flow distance between flags and L the flag length (figure 4.1). The non-dimensional parameter $\widetilde{T}$ will be used throughout this chapter and is defined by

$$\widetilde{T} = \frac{T}{L}$$

The flags will be labeled left flag and right flag, corresponding to their position

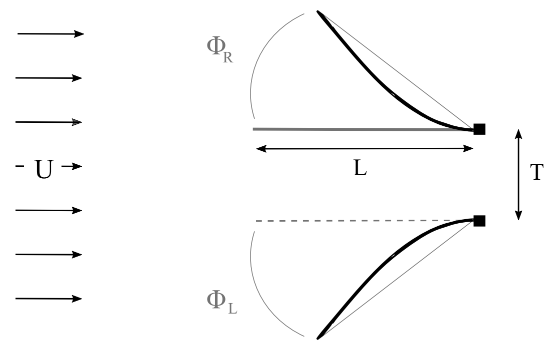

Figure 4.1: Top view of the side-by-side inverted flag arrangement and parameters employed for its characterization.

when the observer is located downstream of the flags and looking upstream, as represented in figure 4.1. The first series of experiments was conducted with two flags that had equal height (H, out of the paper) and length, L (flag 12 in table 1.3). In the second series, the height of both flags, H, and the length of one of the flags, L_0, were maintained constant, while the length of the second flag, L, was varied (flags 13 - 22 in table 1.3).

4.1 Results

Flags of equal dimensions

The three main dynamic regimes present in the motion of a single flag (straight, flapping and deflected) as well as the chaotic motion described by Sader et al. (2016a) persist in the two flag system. For the distances $\widetilde{T}$ considered in this study and at low flow speeds (straight regime, figure 4.2a), the flags oscillate with small amplitude relative to the flag separation and no coupling occurs. As the wind speed is increased, the flag motion reaches angular amplitudes greater than 10 degrees, giving rise to periodic vortex shedding and flapping (Sader et al., 2016a). The lower critical wind speed, κ_{lower}, at which the flapping motion is onset was not observed to vary with the presence of the second flag. This is consistent with the onset of flapping occurring through an initial divergence instability that is dependent on the aerodynamic lift coefficient at small angles (Sader et al., 2016a). It is to be expected, however, that variations in the critical wind speed as well as synchronization in the straight regime will occur at flag separations smaller than those considered in this study.

In the flapping regime (figure 4.2b) the flags interact strongly. An increase in the angular amplitude of flapping of up to 36% was observed for the two-flag system with

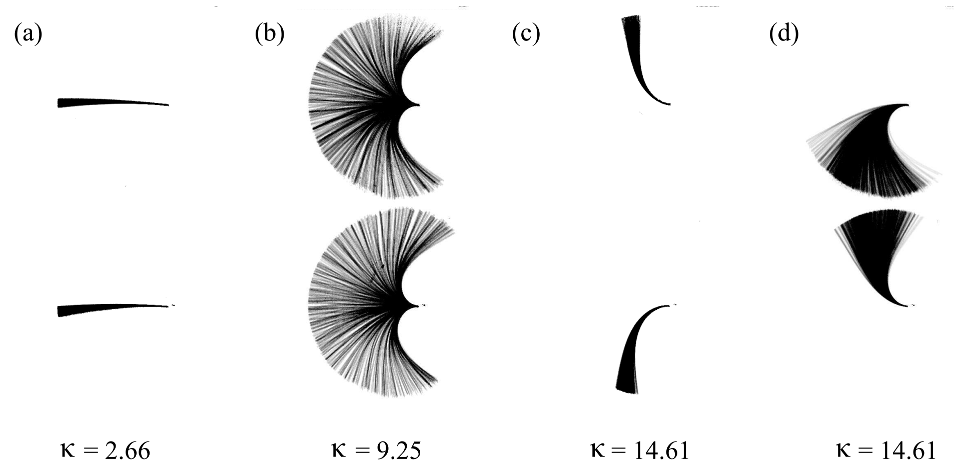

Figure 4.2: Stroboscopic progressions of the motion of the two-flag system showing the (a) straight regime, (b) flapping regime, (c) deflected regime in the outside-deflected configuration and (d) deflected regime in the inside-deflected configuration

respect to the single flag. Figure 4.3 shows the peak-to-peak amplitude of motion, averaged between the right and left flags, for varying separation distances. As the distance between flags is increased the gain in amplitude becomes less prominent, saturating at the single flag value for $\widetilde{T} > 3.2$. This increase in amplitude is asymmetrical; as is evident from the stroboscopic progressions in figure 4.2b, the flags sweep a larger angle towards the interior (center) of the system. Small increases in frequency, up to 13%, were also observed at the smallest separations for the initial stages of the flapping regime. Increases both in the amplitude and frequency of flapping suggest that the energy available for harvesting in the two flag system is higher than that of the single flag.

Five different modes of flapping are present in the side-by-side inverted flag system. The angle ϕ of both flags as a function of time and the corresponding phase diagrams have been plotted in figure 4.4 for each of the modes. The phase diagrams have been colored to represent time: initially the curve is red and turns into blue as time advances. The modes include both an anti-phase regime (figure 4.4a) , where the flags flap symmetrically, and an in-phase regime (figure 4.4b), where the flags flap anti-symmetrically. Staggered flapping, where the phase between flags is constant and between 0 and π, can also occur (figure 4.4c). In the alternating mode (figure 4.4d) the flags switch intermittently between two or more of the in-phase, anti-phase and staggered motions. This mode differs from the decoupled mode (figure 4.4e), where no coupling occurs, in the fact that the flags spend significantly more time

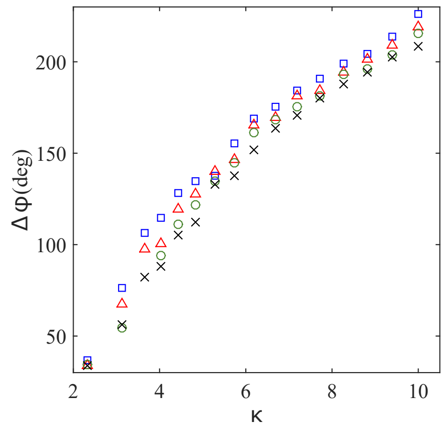

Figure 4.3: Peak-to-peak angular amplitude of motion, $\Delta\phi$, in the flapping regime for a single flag (×) and two flags separated by $\widetilde{T} = 2(\square)$, $\widetilde{T} = 2.4(\triangle)$ and $\widetilde{T} = 2.8(\circ)$. Represented values are the average of left and right flags.

in-phase, anti-phase and staggered than they do transitioning between the motions.

Because two identical flags have equal flapping frequency, they may appear to be flapping in-phase, anti-phase or staggered even if they are not interacting with each other. Therefore, in-phase, anti-phase or staggered modes have only been considered here when they constitute a steady state after starting from a different initial condition (see, for example, the phase diagram of staggered mode in figure 4.4c). In the current experiments, small variations in initial curvature, dimensions and angle of attack caused the frequencies of the right and left flags to differ, and therefore the phase between flags was observed to constantly change in the decoupled mode (figure 4.4e).

The relationship between wind speed, flag separation and flapping mode is summarized in figure 4.5. For small separations ($\widetilde{T} < 3.5$), the flags were observed to flap mainly in the anti-phase mode. For the same range of velocities an in-phase motion can also occur. However, the anti-phase mode is energetically favorable and any staggered initial conditions or perturbations in the in-phase mode will lead to anti-phase flapping. As the distance between flags is increased, the range of velocities for which this predominantly anti-phase flapping is present decreases, giving rise to the staggered, in-phase and alternating modes. These appear for the higher wind speeds in the flapping range, while the anti-phase mode remains for the lower velocities. The distribution of staggered, in-phase and alternating modes for the different wind speeds and separation distances is not clearly defined. This

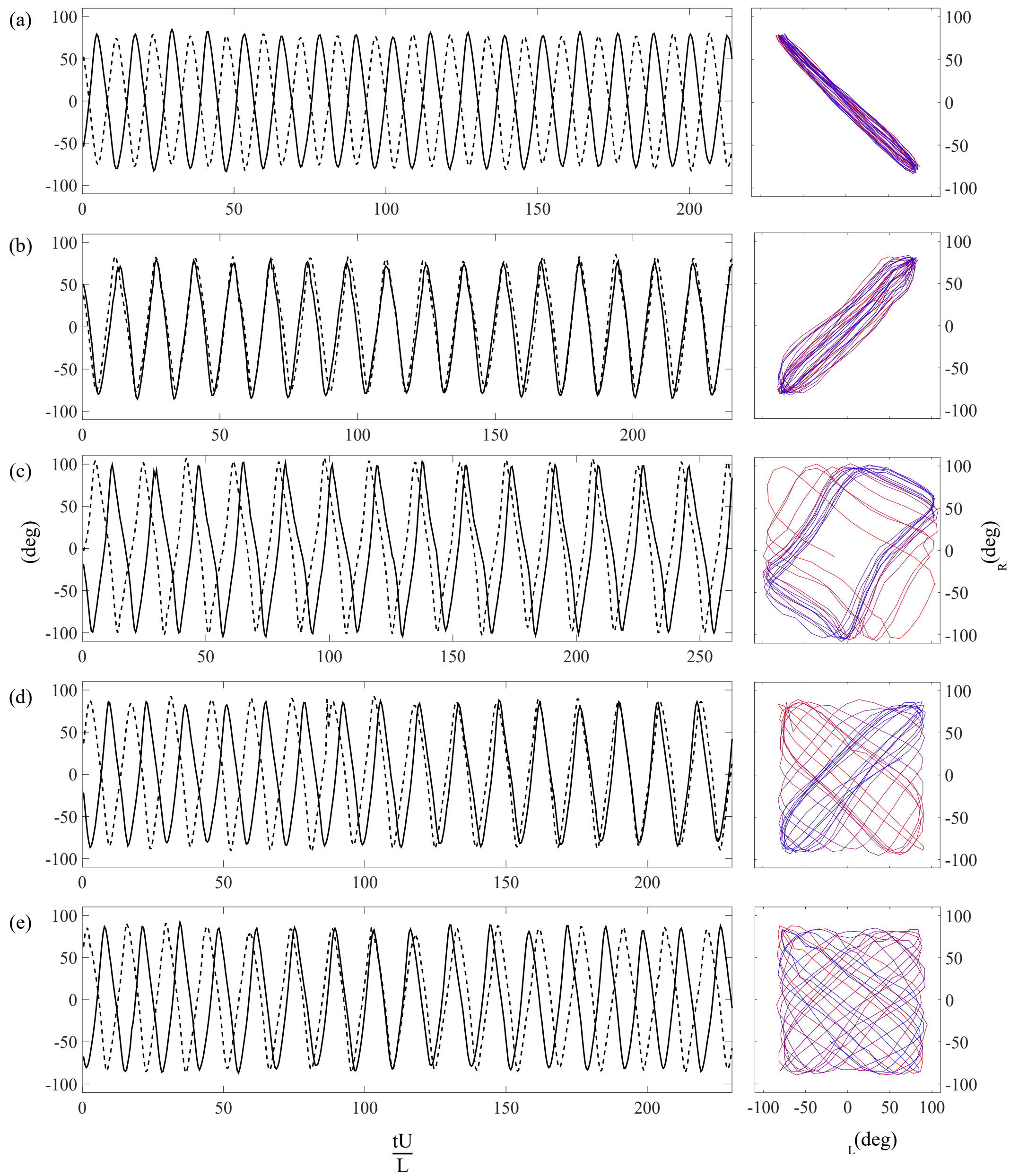

Figure 4.4: Time history of the angle ϕ for the left flag (solid line) and right flag (dashed line) on the left and phase diagram on the right for (a) anti-phase, (b) in-phase, (c) staggered (d) alternating and (e) decoupled modes. Phase diagrams have been colored to represent time, with the curve being initially red and shifting to blue as time advances

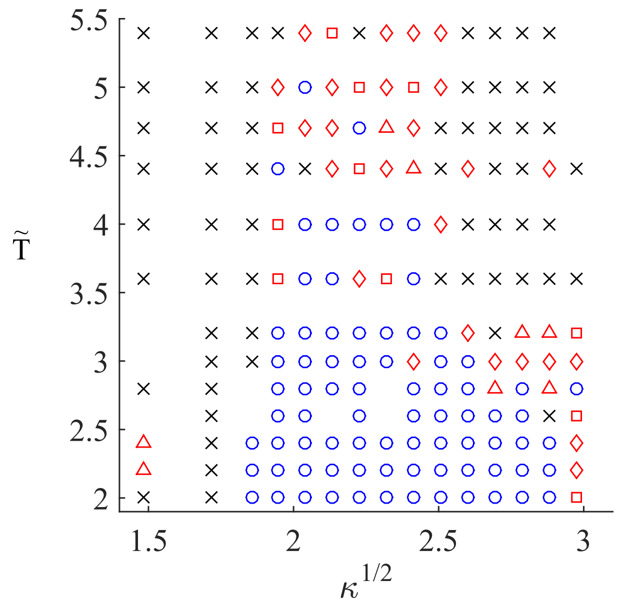

Figure 4.5: Flapping modes as a function of the dimensionless wind speed, $\sqrt{\kappa}$ and flag separation, $\widetilde{T}$: ($\times$) decoupled, ($\circ$) anti-phase, ($\triangle$) in-phase, ($\square$) staggered and ($\diamond$) alternating. Not all possible modes are represented in this figure.

suggests that as the anti-phase flapping becomes less energetically favorable several modes are possible, with different initial conditions giving rise to different modes and perturbations causing the flags to switch from one mode to the other. At a distance of $\widetilde{T} = 5$, the predominantly anti-phase flapping fully disappears. Finally, for large separation distances and high wind speeds the flags enter the decoupled regime, flapping uncoupled.

As wind speed is increased, the chaotic regime emerges. No synchronization was observed between the flags in this regime (see figure 4.6a). For wind speeds over a critical value the flags enter the deflected regime. No clear variations in the critical transition speed from the flapping to the deflected regimes have been observed for the two-flag system with respect to a single flag. For flow speeds immediately over the transition speed the flags deflect towards the outside region, independently of the initial condition (as depicted in figure 4.2c). The oscillating motion of the flags around this outside deflected position is independent, and therefore the flags only interact with each other at the initial stages, when they repel and force the outside deflected position. As flow speed is increased, however, the high fluid damping prevents the flags from changing side and inside (figure 4.2d), outside and asymmetric (one flag inside and one outside) deflected states are possible

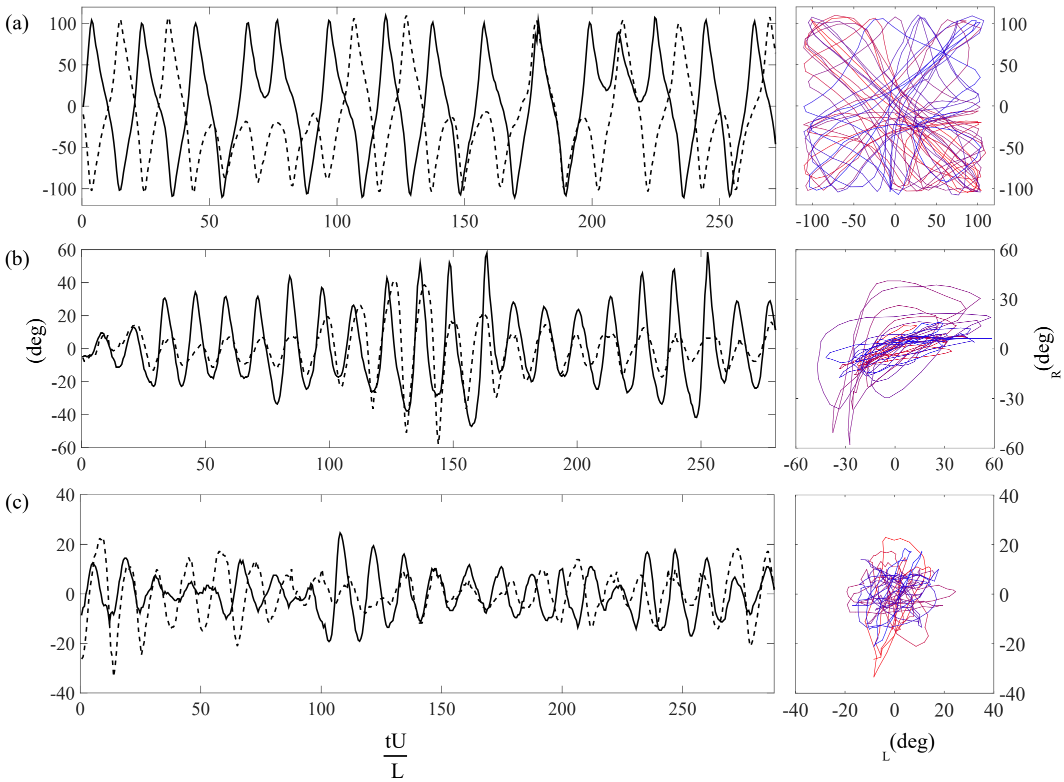

Figure 4.6: Time history of the angle ϕ for the left flag (solid line) and right flag (dashed line) on the left and phase diagram on the right for (a) chaotic, (b) inside-deflected in-phase and (c) inside-deflected decoupled. Phase diagrams have been colored to represent time, with the curve being initially red and shifting to blue as time advances. For the deflected states (b) and (c) the average has been subtracted.

depending on the initial conditions. There is, again, no coupling between outside or asymmetrically deflected flags. However, inside-deflected flags can synchronize in-phase when considering oscillations around the deflected equilibrium (figure 4.6b). As speed is further increased synchronization ceases (figure 4.6c).

Flags with different lengths

Flags that are equal in size have the same vortex shedding frequency, allowing for synchronization of the vortex streets and therefore of the motion of the flags. For flags of different lengths, on the other hand, the vortex shedding frequencies will not be equal. If these frequencies are sufficiently close, the vortex streets can still lock and synchronization will occur. Synchronization will cease, however, for flags that have significantly different lengths and therefore vortex shedding and natural frequencies. To study the effect of the relative length of the flags, a number of tests were performed in which the left flag was kept at a constant length, $L_0 = 0.1\ m$,

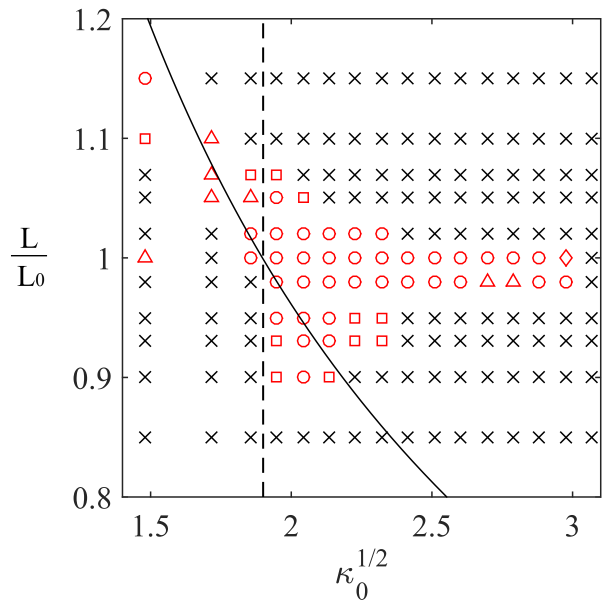

Figure 4.7: Flapping modes as a function of the dimensionless wind speed, $\sqrt{\kappa_0}$ and the flag length ratio, (L/L_0): ($\times$) decoupled, ($\circ$) anti-phase, ($\triangle$) in-phase, ($\square$) staggered and ($\diamond$) alternating. The distance between flags is constant ($T/L_0 = 2.4$). Lines represent the critical value of $\sqrt{\kappa_0}$ at which a single flag of length L_0 (dashed) and L (solid) enter the flapping regime.

while the length of the right flag, L, was varied. The distance between flags was maintained constant at $T/L_0 = 2.4$. The results are plotted in figure 4.7, where the length used for the dimensionless variable κ_0 is that of the left constant flag ($L_0 = 0.1\ m$).

For flags of the same length the results are equal to those reported in Section 4.1. The flags synchronize anti-phase for most of the velocities in the flapping range, although staggered modes are also present. As L is decreased, the range of velocities at which the flags synchronize decreases; at $\frac{L}{L_0} \leq 0.85$ synchronization ceases to occur. Simultaneously, the anti-phase mode becomes less predominant, with the staggered mode being more prevalent. Similarly, as L is increased from the $\frac{L}{L_0} = 1$ value, the range of wind speeds at which the flags synchronize decreases and the anti-phase mode vanishes in favor of in-phase and staggered motions.

Because the variations in aspect ratio are small, the critical value of κ at which both flags enter the flapping regime is approximately equal. Due to the difference in length, however, this corresponds to different values of the dimensional wind speed, meaning that there is a range of wind speeds at which the longer flag is in the flapping

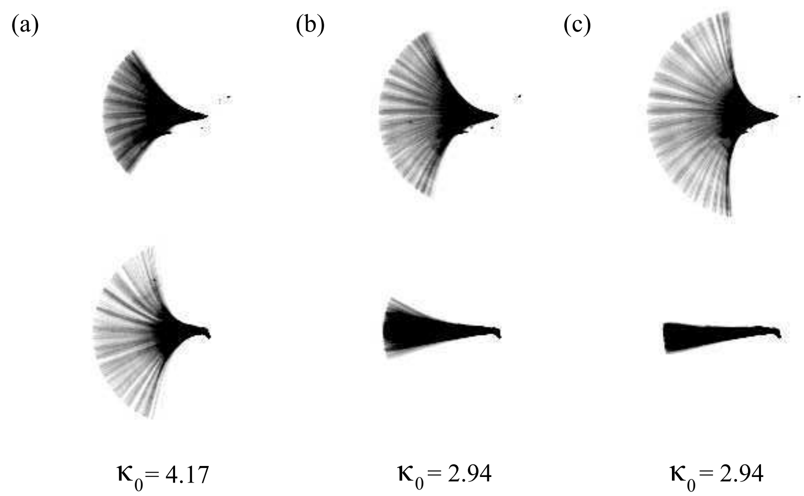

Figure 4.8: Stroboscopic progressions of the motion of two inverted flags of different lengths at a constant separation $T/L_0 = 2.4$. , showing (a) the long flag inducing a flapping motion on the short flag ($L/L_0 = 0.9$), (b) the long flag inducing an oscillating motion on the short flag ($L/L_0 = 1.05$) and (c) the long flag flapping and the short flag oscillating uncoupled ($L/L_0 = 1.15$). The flag of constant length $L_0 = 0.1$ m is depicted at the bottom.

regime while the shorter one is in the straight regime. To identify these regions, the lines corresponding to the critical dimensionless velocity $\kappa_0 = \kappa_{lower}$ for each of the flags, as given by equation (2.15) in Sader et al. (2016b), have been plotted in figure 4.7. The dashed line corresponds to the critical κ for the flag of constant length L_0, while the solid line corresponds to that of the flag of varying length L. The equation slightly overestimates the value of κ_{lower} that was experimentally observed, including the case of a single flag, presumably due to small variations in flow uniformity and initial curvature.

For $\frac{L}{L_0} < 1$, the flag of length L_0 reaches its flapping range at lower flow speeds than the flag of length L. As is evident in figure 4.7, despite the fact that the flag of length L is under its critical κ, synchronization, mostly in an anti-phase mode, still occurs. The flag of length L was observed to flap in these conditions (figure 4.8a), implying that the motion and resulting vortex street of the longer flag is inducing a flapping motion in the shorter flag. For the opposite case, $\frac{L}{L_0} > 1$, a similar behavior was observed: synchronization occurs for wind speeds at which the flag of length L has reached its flapping regime but that of length L_0 has not. In this case, however, the shorter flag does not flap, but oscillates with small amplitude (figure 4.8b). These oscillations are in phase with the flapping motion of the longer flag and are larger than the oscillations that occur when the flags move uncoupled (figure 4.8c). This leads to the conclusion that it is the flow displaced by the flapping flag that impinges on the short flag and causes it to deflect. These two different behaviors (induced flapping and induced oscillations) in a seemingly symmetric problem arise because the distance between flags was maintained at a constant value and, therefore, the relative distance T/L is different in the two cases, with the flags being effectively closer in the $\frac{L}{L_0} > 1$ case.

4.2 Conclusions

This study has experimentally investigated the interaction between two inverted flags that are placed side-by-side in a uniform flow and the resulting coupled motion in the flapping and deflected regimes. It is relevant to the analysis of natural phenomena, such as leaves flapping in the wind, where multiple flags are generally present, as well as to the design of energy harvesting mechanisms, where the arrangement of multiple flags could be exploited to increase energy extraction.

Flags that were placed side-by-side saw an increase in flapping angular amplitude of up to 36% and an increase in frequency of up to 13% with respect to the motion of a single flag. Five different coupled modes of motion were observed in the flapping regime: in-phase, anti-phase, staggered, alternating and decoupled. The anti-phase mode is energetically favorable and predominant for small separations and low wind speeds, while the remaining modes appear for larger separations and high wind speeds. Inside, outside and asymmetric configurations are present in the deflected regime, with the inside configuration being the only one that presents a coupled in-phase motion.

Coupling was observed to occur between flags that had different lengths. However, the range of velocities at which coupling occurred was observed to diminish as the difference in flag lengths increased, with no coupling occurring for differences larger than 15%. Interestingly, the longer flag was observed to induce flapping on the shorter flag when the latter was outside of its flapping range.

A posterior experimental and theoretical analysis has been performed by Kim and Kim (2019) on side-by-side inverted flags at flag distances smaller than those presented in this chapter, complementing these results. For those distances and in the straight regime, Kim and Kim (2019) found that the gap flow pushes the flags to an out-of-phase outwards deflected equilibrium. This causes the flags to lose stability at wind speed values lower than those of a single flag, with the critical wind speed increasing monotonically as the flag distance increases. At wind speeds between this lower critical value and the critical wind speed of a single inverted flag the flapping amplitude was, however, significantly smaller. In addition to the modes introduced here, Kim and Kim (2019) showed the existence of a static attached mode, where the leading edge of both flags is in contact.

An additional computational study of the side-by-side inverted-flag configuration has been implemented by Ryu et al. (2018). Their results show similar modes of motion as described above. Notably, when initialized in an in-phase mode, the flag motion remained in phase for a much wider range of parameters than found in this work. This may be explained by the much lower level of the perturbations present in the numerical framework compared to the experiments, that results in the flag not being perturbed away from the less energetically favorable in-phase mode. Finally, an interesting computational investigation of inverted flags in tandem and staggered configurations is presented in Huang et al. (2018). The readers are referred to the text for further information and details.

Chapter 5

CONCLUDING REMARKS AND FUTURE WORK

The inverted-flag configuration was first proposed as a performance-improving alternative to the conventional flag used in piezoelectric energy harvesters. Other applications have emerged, however, as their study has provided further insights into the configuration. An example is the use of inverted flags as vortex generators to enhance the heat transfer in heat exchangers (Chen et al., 2018; Li et al., 2019; Park et al., 2016; Yu et al., 2018). The study of inverted flags has, additionally, been found to be relevant to the understanding of natural phenomena such as the flutter of leaves in the wind (Fan et al., In press; Zhou et al., 2019), which possess a clamped-free configuration and present varying angles to the flow. The emergence of these applications has generated an increased interest in the inverted-flag configuration, resulting in the development of an extensive literature. The behavior and mechanics of the inverted flag are, nevertheless, not yet fully understood.

The first part of this thesis has researched aspects of the inverted flag's mechanics that are essential to its characterization and had been previously unexplored. Chapter 2 was devoted to inverted flags of very low aspect ratio, which were shown to undergo a saddle-node bifurcation instead of a divergence instability followed by a vortex induced vibration. Chapter 3 focused on the effect of a moderate angle of attack on the dynamics of the flag. Regimes analogous to those existent at zero angle of attack were shown to be present, with the flapping regime being divided into two distinct branches. Chapter 4 delved into the interaction between two inverted flags that are placed in a side-by-side arrangement and highlighted the presence of an energetically favorable symmetric flapping mode among other coupled dynamics.

Several outstanding topics have, however, not been addressed in the current work, which has additionally raised numerous new questions, many of which remain unanswered. Some of these topics are highlighted here. A detailed description of the added mass and flow damping experienced by the flag will undoubtedly aid in the prediction of the lock-off of the flapping regime, as well as the development of a more rigorous theoretical framework for the flag's dynamics. This is, however, an arduous task; many related studies have been performed on vortex induced vibrations of different geometries without a complete answer being available to date. An additional phenomenon that has been only lightly investigated is the vortex formation on the flag's leading edge and the process by which the initial transients give rise to the resulting limit cycle oscillations. The identification of parameters that result in optimal vortex formation may, moreover, be useful in the design and dimensioning of the piezoelectric energy harvesters. In relation to natural phenomena, the use of non-uniform flexibility and porosity in the flag will deliver a more faithful description of leaf-like structures. Its use may also be conductive to increased performance in engineering applications.

The most prominent deficit in the existing literature is the lack of experimental flow visualizations of the fluid surrounding the inverted flag. Up to date, only two such analyses, both of which were performed in water, have been reported. The corresponding flags had an unspecified aspect ratio and $\mu = 4 - 6\ 10^{-3}$ (Kim et al., 2013), and AR=3 and $\mu = 7\ 10^{-3}$ (Yu et al., 2017) and were placed at zero angle of attack. The observation of the vortex dynamics and quantitative analysis of the flow for flags of different aspect ratios, angles of attack and arrangements would provide significant insights into the topics presented in this thesis. In particular, the vortex formation and scale behind flags of low aspect ratios would provide a rationale for the lack of flapping in very low aspect ratio flags. The wake patterns and shedding timing would aid in elucidating the mechanics behind the lower branch of the flapping regime, as well as clarifying the distinction between branches in the AR=2 case. They may be additionally valuable to interpreting the transitions occurring at the marked $\kappa^{1/2} = 1.5$ and $\kappa^{1/2} = 2$ velocities as well as the emergence of the chaotic and deflected regimes. The observation of vortex shedding modes would be particularly relevant in the case of coupled flags, were each coupled dynamical mode is expected to be associated to a different wake pattern.

Overall, the inverted-flag configuration examined throughout this text has been shown to possess striking dynamical characteristics and constitutes an outstanding representation of the complexity of coupled solid-fluid interactions. Although many advances have been made in recent years, its behavior is yet to be fully explained, with the continued investigation of the inverted flag configuration remaining a promising line for future work.

BIBLIOGRAPHY TO PART I

R. Ahmed, F. Mir, and S. Banerjee. A review on energy harvesting approaches for renewable energies from ambient vibrations and acoustic waves using piezoelectricity. *Smart Materials and Structures*, 26(8):085031, 2017.

J. Allen and A. Smits. Energy harvesting eel. *Journal of fluids and structures*, 15 (3–4):629–640, 2001.

J. D. Anderson Jr. *Fundamentals of aerodynamics*. Tata McGraw-Hill Education, 2010.

M. Argentina and L. Mahadevan. Fluid-flow-induced flutter of a flag. *Proceedings of the National Academy of Sciences*, 102(6):1829–1834, 2005.

W. Bollay. A non-linear wing theory and its application to rectangular wings of small aspect ratio. *Z. angew. Math. Mech*, 19(1):21–35, 1939.

Y. Chen, Y. Yu, W. Zhou, D. Peng, and Y. Liu. Heat transfer enhancement of turbulent channel flow using tandem self-oscillating inverted flags. *Physics of Fluids*, 30(7):075108, 2018.

J. Cossé, J. Sader, D. Kim, C. Huertas Cerdeira, and M. Gharib. The effect of aspect ratio and angle of attack on the transition regions of the inverted flag instability. In *Proc. ASME*, 2014.

J. T. Cossé. *On the behavior of pliable plate dynamics in wind: application to vertical axis wind turbines*. PhD thesis, California Institute of Technology, 2014.

E. De Langre. Effects of wind on plants. *Annu. Rev. Fluid Mech.*, 40:141–168, 2008.

D. Dong, W. Chen, and S. Shi. Coupling motion and energy harvesting of two side-by-side flexible plates in a 3d uniform flow. *Applied Sciences*, 6(5):141, 2016.

C. Eloy, R. Lagrange, C. Souilliez, and L. Schouveiler. Aeroelastic instability of cantilevered flexible plates in uniform flow. *Journal of Fluid Mechanics*, 611: 97–106, 2008.

N. Elvin and A. Erturk. *Advances in energy harvesting methods*. Springer Science & Business Media, 2013.

B. Fan, C. Huertas-Cerdeira, J. Cossé, J. E. Sader, and M. Gharib. Effect of morphology on the large-amplitude flapping dynamics of an inverted flag in a uniform flow. *Journal of Fluid Mechanics*, In press.

D. J. Farnell, T. David, and D. Barton. Coupled states of flapping flags. *Journal of Fluids and Structures*, 19(1):29–36, 2004.

H. Glauert. *The elements of aerofoil and airscrew theory*. Cambridge University Press, 1983.

A. Goza, T. Colonius, and J. E. Sader. Global modes and nonlinear analysis of inverted-flag flapping. *Journal of Fluid Mechanics*, 857:312–344, 2018.

P. Gurugubelli and R. Jaiman. Self-induced flapping dynamics of a flexible inverted foil in a uniform flow. *Journal of Fluid Mechanics*, 781:657–694, 2015.

H. Huang, H. Wei, and X.-Y. Lu. Coupling performance of tandem flexible inverted flags in a uniform flow. *Journal of Fluid Mechanics*, 837:461–476, 2018.

F. Huera-Huarte and M. Gharib. Flow-induced vibrations of a side-by-side arrangement of two flexible circular cylinders. *Journal of Fluids and Structures*, 27(3): 354–366, 2011.

C. Huertas-Cerdeira, B. Fan, and M. Gharib. Coupled motion of two side-by-side inverted flags. *Journal of Fluids and Structures*, 76:527–535, 2018.

L.-B. Jia, F. Li, X.-Z. Yin, and X.-Y. Yin. Coupling modes between two flapping filaments. *Journal of Fluid Mechanics*, 581:199–220, 2007.

E. Johnson and J. Jacob. Development and testing of a gust and shear wind tunnel for navs and mavs. In *47th AIAA Aerospace Sciences Meeting Including The New Horizons Forum and Aerospace Exposition*, page 64, 2009.

D. Kim, J. Cossé, C. Huertas Cerdeira, and M. Gharib. Flapping dynamics of an inverted flag. *Journal of Fluid Mechanics*, 736:R1, 2013.

H. Kim and D. Kim. Stability and coupled dynamics of three-dimensional dual inverted flags. *Journal of Fluids and Structures*, 84:18–35, 2019.

A. Kornecki, E. Dowell, and J. O'Brien. On the aeroelastic instability of two-dimensional panels in uniform incompressible flow. *Journal of Sound and Vibration*, 47(2):163–178, 1976.

L. D. Landau and E. M. Lifshitz. *Theory of Elasticity*. Pergamon, Oxford, 1970.

H. Lee, S. Sherrit, L. Tosi, P. Walkemeyer, and T. Colonius. Piezoelectric energy harvesting in internal fluid flow. *Sensors*, 15(10):26039–26062, 2015.

K. Li, S. Wang, Z. Ke, and C.-L. Chen. A novel caudal-fin-inspired hourglass-shaped self-agitator for air-side heat transfer enhancement in plate-fin heat exchanger. *Energy Conversion and Management*, 187:297–315, 2019.

H. Liu, J. Zhong, C. Lee, S.-W. Lee, and L. Lin. A comprehensive review on piezoelectric energy harvesting technology: Materials, mechanisms, and applications. *Applied Physics Reviews*, 5(4):041306, 2018.

Y. Liu, R. So, Y. Lau, and Y. Zhou. Numerical studies of two side-by-side elastic cylinders in a cross-flow. *Journal of Fluids and Structures*, 15(7):1009–1030, 2001.

M. Luhar and H. M. Nepf. Flow-induced reconfiguration of buoyant and flexible aquatic vegetation. *Limnol. Oceanogr.*, 56:2003–2017, 2011.

L. Mateu and F. Moll. Review of energy harvesting techniques and applications for microelectronics (keynote address). In *VLSI Circuits and Systems II*, volume 5837, pages 359–374. International Society for Optics and Photonics, 2005.

S. Orrego, K. Shoele, A. Ruas, K. Doran, B. Caggiano, R. Mittal, and S. H. Kang. Harvesting ambient wind energy with an inverted piezoelectric flag. *Applied Energy*, 194:212–222, 2017.

M. P. Païdoussis. *Fluid-structure interactions: slender structures and axial flow*, volume 1. Academic press, 1998.

J. A. Paradiso and T. Starner. Energy scavenging for mobile and wireless electronics. *IEEE Pervasive computing*, (1):18–27, 2005.

C. Park and P. H. Chou. Ambimax: Autonomous energy harvesting platform for multi-supply wireless sensor nodes. In *2006 3rd annual IEEE communications society on sensor and ad hoc communications and networks*, volume 1, pages 168–177. IEEE, 2006.

S. G. Park, B. Kim, C. B. Chang, J. Ryu, and H. J. Sung. Enhancement of heat transfer by a self-oscillating inverted flag in a poiseuille channel flow. *International Journal of Heat and Mass Transfer*, 96:362–370, 2016.

S. Priya. Advances in energy harvesting using low profile piezoelectric transducers. *Journal of electroceramics*, 19(1):167–184, 2007.

L. Rayleigh. On the instability of jets. *Proceedings of the London mathematical society*, 1(1):4–13, 1878.

J. Ryu, S. G. Park, B. Kim, and H. J. Sung. Flapping dynamics of an inverted flag in a uniform flow. *Journal of Fluids and Structures*, 57:159–169, 2015.

J. Ryu, S. G. Park, and H. J. Sung. Flapping dynamics of inverted flags in a side-by-side arrangement. *International Journal of Heat and Fluid Flow*, 70:131–140, 2018.

J. E. Sader, J. Cossé, D. Kim, B. Fan, and M. Gharib. Large-amplitude flapping of an inverted flag in a uniform steady flow–a vortex-induced vibration. *Journal of Fluid Mechanics*, 793:524–555, 2016a.

J. E. Sader, C. Huertas-Cerdeira, and M. Gharib. Stability of slender inverted flags and rods in uniform steady flow. *Journal of Fluid Mechanics*, 809:873–894, 2016b.

M. Samorani. The wind farm layout optimization problem. In *Handbook of wind power systems*, pages 21–38. Springer, 2013.

M. J. Shelley and J. Zhang. Flapping and bending bodies interacting with fluid flows. *Annual Review of Fluid Mechanics*, 43:449–465, 2011.

K. Shoele and R. Mittal. Energy harvesting by flow-induced flutter in a simple model of an inverted piezoelectric flag. *Journal of Fluid Mechanics*, 790:582–606, 2016.

W. Si-Ying, D. Wen-Gang, and Y. Xie-Zhen. Transition mode of two parallel flags in uniform flow. *Chinese Physics Letters*, 30(11):110502, 2013.

J. Silva-Leon, A. Cioncolini, M. R. Nabawy, A. Revell, and A. Kennaugh. Simultaneous wind and solar energy harvesting with inverted flags. *Applied Energy*, 239:846–858, 2019.

H. A. Sodano, D. J. Inman, and G. Park. A review of power harvesting from vibration using piezoelectric materials. *Shock and Vibration Digest*, 36(3):197–206, 2004.

C. Sun, S. Wang, L. Jia, and X. Yin. Force measurement on coupled flapping flags in uniform flow. *Journal of Fluids and Structures*, 61:339–346, 2016.

S. Taneda. Waving motions of flags. *Journal of the Physical Society of Japan*, 24 (2):392–401, 1968.

C. Tang, N.-S. Liu, and X.-Y. Lu. Dynamics of an inverted flexible plate in a uniform flow. *Physics of Fluids*, 27(7):073601, 2015.

L. Tang, M. P. Païdoussis, and J. Jiang. Cantilevered flexible plates in axial flow: energy transfer and the concept of flutter-mill. *Journal of Sound and Vibration*, 326(1):263–276, 2009.

M. Tavallaeinejad, M. P. Païdoussis, and M. Legrand. Nonlinear static response of low-aspect-ratio inverted flags subjected to a steady flow. *Journal of Fluids and Structures*, 83:413–428, 2018.

G. W. Taylor, J. R. Burns, S. M. Kammann, W. B. Powers, and T. R. Wel. The energy harvesting eel: a small subsurface ocean/river power generator. *Oceanic Engineering, IEEE Journal of*, 26(4):539–547, 2001.

S. Vogel. *Life in moving fluids*. Princeton University Press, 1994.

D. Weihs. Hydromechanics of fish schooling. *Nature*, 241(5387):290–291, 1973.

M. A. Weimer, T. S. Paing, and R. A. Zane. Remote area wind energy harvesting for low-power autonomous sensors. In *2006 37th IEEE Power Electronics Specialists Conference*, pages 1–5. IEEE, 2006.

R. W. Whittlesey, S. Liska, and J. O. Dabiri. Fish schooling as a basis for vertical axis wind turbine farm design. *Bioinspiration & biomimetics*, 5(3):035005, 2010.

C. Williamson and R. Govardhan. Vortex-induced vibrations. *Annu. Rev. Fluid Mech.*, 36:413–455, 2004.

Y. Yu, Y. Liu, and Y. Chen. Vortex dynamics behind a self-oscillating inverted flag placed in a channel flow: Time-resolved particle image velocimetry measurements. *Physics of Fluids*, 29(12):125104, 2017.

Y. Yu, Y. Liu, and Y. Chen. Vortex dynamics and heat transfer behind self-oscillating inverted flags of various lengths in channel flow. *Physics of Fluids*, 30(4):045104, 2018.

Y. Yu, Y. Liu, and X. Amandolese. A review on fluid-induced flag vibrations. *Applied Mechanics Reviews*, 71(1):010801, 2019.

M. Zdravkovich. Flow induced oscillations of two interfering circular cylinders. *Journal of Sound and Vibration*, 101(4):511–521, 1985.

M. M. Zdravkovich. *Flow around Circular Cylinders: Volume 2: Applications*, volume 2. Oxford university press, 2003.

J. Zhang, S. Childress, A. Libchaber, and M. Shelley. Flexible filaments in a flowing soap film as a model for one-dimensional flags in a two-dimensional wind. *Nature*, 408(6814):835–839, 2000.

M. Zhou, Q. Chen, Z. Xu, and W. Wang. Piezoelectric wind energy harvesting device based on the inverted cantilever beam with leaf-inspired extensions. *AIP Advances*, 9(3):035213, 2019.

Y. Zhou, Z. Wang, R. So, S. Xu, and W. Jin. Free vibrations of two side-by-side cylinders in a cross-flow. *Journal of Fluid Mechanics*, 443:197–229, 2001.

L. Zhu and C. S. Peskin. Interaction of two flapping filaments in a flowing soap film. *Physics of Fluids (1994-present)*, 15(7):1954–1960, 2003.

Part II

Flapping propellers

Chapter 6

INTRODUCTION

Autonomous underwater vehicles (AUVs) have received recent attention as a means of performing underwater missions that are unattainable by a human operator due to accessibility constraints, hazardous conditions or operational cost. They have become useful tools for many applications, such as deep water exploration and surveying, ocean sensing, maintenance of offshore oil installations and wind turbines, spill inspection and military operations (Griffiths, 2002; Roper et al., 2011). Because they function in such extreme environments, AUVs necessitate state-of-the-art capabilities. Their propulsion mechanisms must be highly efficient in order to reach long ranges with the limited available power. They are often imposed strict noise constraints to prevent being detected or perturbing their surroundings and require rapid maneuverability to operate in reduced spaces and avoid impact from foreign objects.

The vast majority of existing aquatic vehicles employs traditional screw propellers, which have been optimized for decades to reach propulsive efficiencies up to 70% (Carlton, 2007; Fish, 2013). The propulsion mechanism is currently responsible, however, for the majority of the radiated noise, with much of this noise being caused by cavitation (Carlton, 2007; Fish, 2013). The past decade has seen a rise in the development of bio-inspired propellers, that constitute great candidates for AUV propulsion. Due to their lower velocities, bio-inspired propellers do not generally present cavitation and naturally radiate much lower levels of noise, with their signature being, additionally, harder to identify (Carlton, 2007; Fish, 2013). The propulsive efficiency of swimming animals has been reported to reach values of up to 90% (Fish, 1998; Rohr and Fish, 2004). While existing fish-inspired propellers are far from that value (Techet, 2008; Triantafyllou et al., 2000; Wen et al., 2013) they have the potential to approach it if optimally designed and may result in higher efficiencies than those attainable by screw propellers.

From a biological standpoint, the swimming locomotion of fish is typically classified into two main types according to the body part employed to generate the force: body and caudal fin (BCF) propulsion and median and paired fin (MPF) propulsion (Sfakiotakis et al., 1999). BCF propulsion functions by generating a lateral wave that travels backwards through the animal's body and caudal fin and can be subdivided into separate modes according to the portion of the body that sees a significant wave amplitude. The highest propulsive efficiencies are achieved by thunniform swimmers, that possess a fairly rigid body and present significant lateral motions at the caudal fin and peduncle only. Fish that are more flexible or utilize MPF propulsion are less efficient cruisers but greatly surpass thunniform swimmers in maneuverability Webb (1984); Weihs (1973).

From an engineering perspective the underwater propulsion mechanisms of animals can be classified according to the fluid forces they are based on: drag, lift or acceleration reaction (Fish, 2013; Sfakiotakis et al., 1999). Drag-based propulsion generally involves two strokes. In the power stroke the appendage is bluff and generates a large pressure drag, while in the recovery stroke it streamlines to return to its initial position with minimum forces. Drag forces are generated by paddling animals and some types of MPF swimmers and can be utilized for precise maneuvering. Acceleration reaction forces correspond to the added mass effect and are present in jetting propulsion and undulatory swimming. Lift forces are generated by the relatively stiff caudal fins of thunniform swimmers and cetaceans and result in the highest propulsive efficiency of the three types.

Due to this high cruising efficiency, lift-based caudal-fin propulsion is a particularly promising line of research. As has been hinted in the previous paragraphs, there is, however, a trade-off between long-range propulsive efficiency and maneuverability (Fish, 2002). AUV bodies are typically comprised of rigid cylindrical vessels, because these are resistant to compression at high pressures and compatible with modular construction (Roper et al., 2011). A rigid AUV that is propelled by a lift-based flapping propeller attached to its rear end will possess limited maneuverability if no additional surfaces or mechanisms are present. To overcome this limitation, multiple studies have proposed the use of flexible bodies (Marchese et al., 2014; Su et al., 2014). The focus of this work, however, is the improvement of the maneuverability of AUVs that must maintain a rigid body due to payload limitations. The maneuvering performance of a caudal-fin propeller that can perform large rotations in all three degrees of freedom is investigated, with the prospect that these complex 3D motions will allow to obtain a highly efficient and highly maneuverable single-fin flapping propeller for AUV use.

6.1 Objectives

A fin that is capable of rotation in all three degrees of freedom can follow an infinite number of different trajectories in its motion. The aim of this study is to obtain the best trajectory that generates a specified desired maneuvering force. The number of possible motions can be reduced by considering a family of trajectories that are defined by a finite number of parameters. In this work ten different degrees of freedom will be considered. Because this number is quite large, sweeping over all combinations of parameters is not viable. Employing an optimization algorithm largely reduces the number of tests that need to be performed in order to find an optimum. This optimization has been performed making use of the experimental setup developed by Martin and Gharib (2018). The optimal trajectories obtained for fins of varying properties will be analyzed in the following chapters. Part II of this thesis is organized as follows

- The remainder of Chapter 6 is dedicated to describing the optimization process and experimental setup
- Chapter 7 investigates the optimal trajectory for fins of high aspect ratio
- Chapter 8 examines the effect of adding flexibility to the fin on the optimal trajectory
- Chapter 9 concludes Part II and highlights the most promising directions for future research

6.2 Optimization procedure

Several existing studies have explored the optimization of propeller properties and motion to obtain maximum propulsive force, efficiency, energy, velocity or lift force both in bio-inspired and screw propellers, as well as in flapping wings (Berman and Wang, 2007; Clark et al., 2012; De Margerie et al., 2007; Kato and Liu, 2003; Martin and Gharib, 2018; Milano and Gharib, 2005; Rakotomamonjy et al., 2007; Tuncer and Kaya, 2005). Due to the ease of interfacing, most of these studies were performed computationally, where the evaluation of fitness in each step of the optimization algorithm was assessed through numerical methods. Because fully resolved simulations are expensive for such a large number of evaluations, these studies are limited to optimizing simplified models and a small number of parameters at low Reynolds numbers. Experimental assessment of the fitness of each optimization step eliminates these limitations, albeit adding a level of complexity

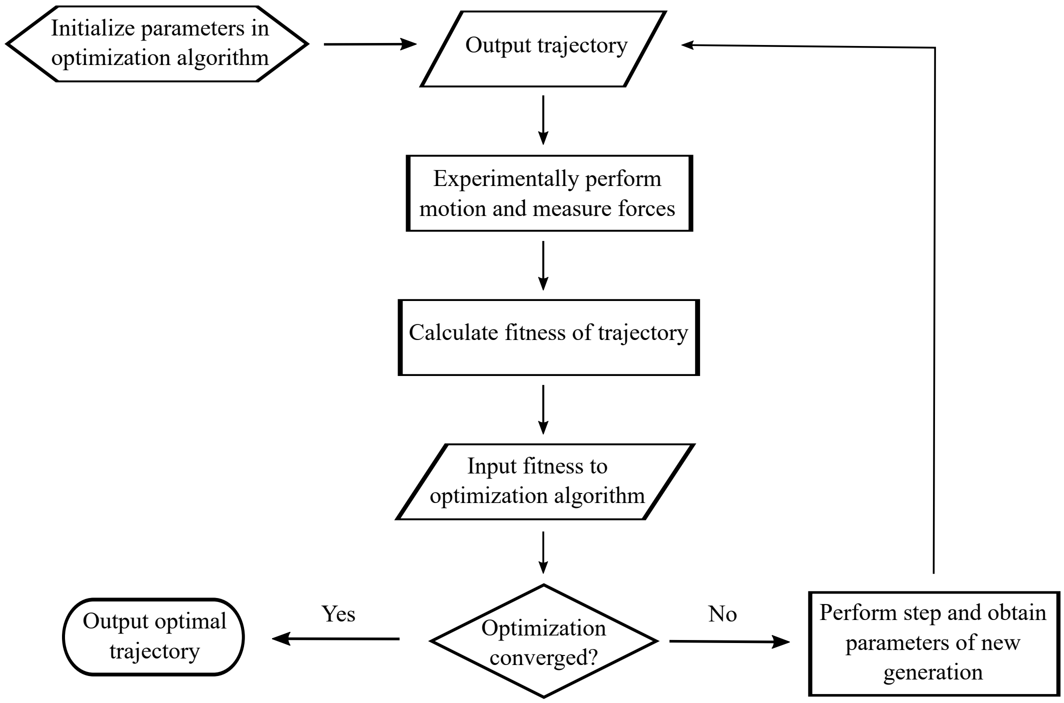

Figure 6.1: Flow chart of optimization process

(Kato and Liu, 2003; Martin and Gharib, 2018; Milano and Gharib, 2005). This experimental assessment is the approach employed in this work, which utilizes the experimental setup developed by Martin and Gharib (2018).

The optimization procedure is described in figure 6.1. Fin trajectories are parametrized employing several variables, including those presented in figure 6.2. Once the optimization algorithm is initialized, it outputs a trajectory whose fitness, as defined in equation 6.2, needs to be assessed. The trajectory is performed utilizing the experimental setup illustrated in figure 6.3 and the forces generated are measured. The fitness is then computed using this data and fed back to the optimization algorithm. If the optimization has converged, the optimal trajectory is output. If it has not converged, the algorithm performs a step in the optimization and outputs a new trajectory whose fitness needs to be assessed. The process is then repeated until and optimum is obtained.

The optimization method selected to perform this procedure is the covariance matrix adaptation evolution strategy (CMAES), which belongs to the broader category of evolution strategies. It is a stochastic method for black-box optimization capable of handling complex non-convex, non-smooth, noisy problems (Hansen, 2006; Hansen and Ostermeier, 2001). Evolution strategies have been successfully employed in many scenarios, including the optimization of fin properties and trajectory of De Margerie et al. (2007); Milano and Gharib (2005); Plucinski et al. (2007) and Clark et al. (2012).

Fin kinematics

The family of trajectories considered is periodic and can be parametrized with the use of ten different variables inspired by the motion of fish fins and insect wings. Their full mathematical description can be found in Martin and Gharib (2018) and Martin (2018). Figure 6.2a illustrates a multiview projection of the three dimensional motion of the fin, with the top portion illustrating the view from the back of the AUV and the bottom portion illustrating the top view. The edge of the fin is highlighted in black, with its center marked with a circle. The trajectory followed by this center point is shown as a black dashed line. To improve the visibility of the figures, the trajectories will be represented throughout this text as the two-dimensional projection, viewed from the back of the AUV, of the path followed by this centerpoint and the position of this highlighted edge. Two such diagrams can be viewed in figures 6.2b and c. The three-dimensionality of these trajectories, evident in the bottom portion of figure 6.2a, should, however, not be overlooked.

Figures 6.2b and c present some of the trajectory's defining parameters. Trajectories can be classified in two main types: figure-eight (figure 6.2b) or ellipse (figure6.2c). The stroke amplitude, ϕ, represents the maximum angular amplitude of motion of the centerpoint. The deviation angle, ψ, characterizes the thickness of its trajectory. The rotation angle determines the rotation of the wing along its z axis, as defined in figure 6.3b. The phase between this rotation and the motion of the centerpoint can also be modified, and is represented by β. The rotation does not necessarily occur at a constant rate, but can be accelerated at the edges of the trajectory. This acceleration is quantified by the rotation acceleration, K_v, that is a measure of the squareness of the rotation signal . The velocity of the centerpoint of the fin can be increased in certain sections of its trajectory, as represented in figure 6.2c. The section to be accelerated is specified by the speed-up code, S, while the speed-up value determines the relative speed of this section with respect to the remaining ones. The camber, λ, represents the asymmetry of the trajectory. Trajectories can, additionally, be performed at varying frequencies, f. The maximum and minimum values for each variable are presented in table 6.1, together with their convergence criteria. The limits on the variables are set according to the physical limitations of the experimental setup.

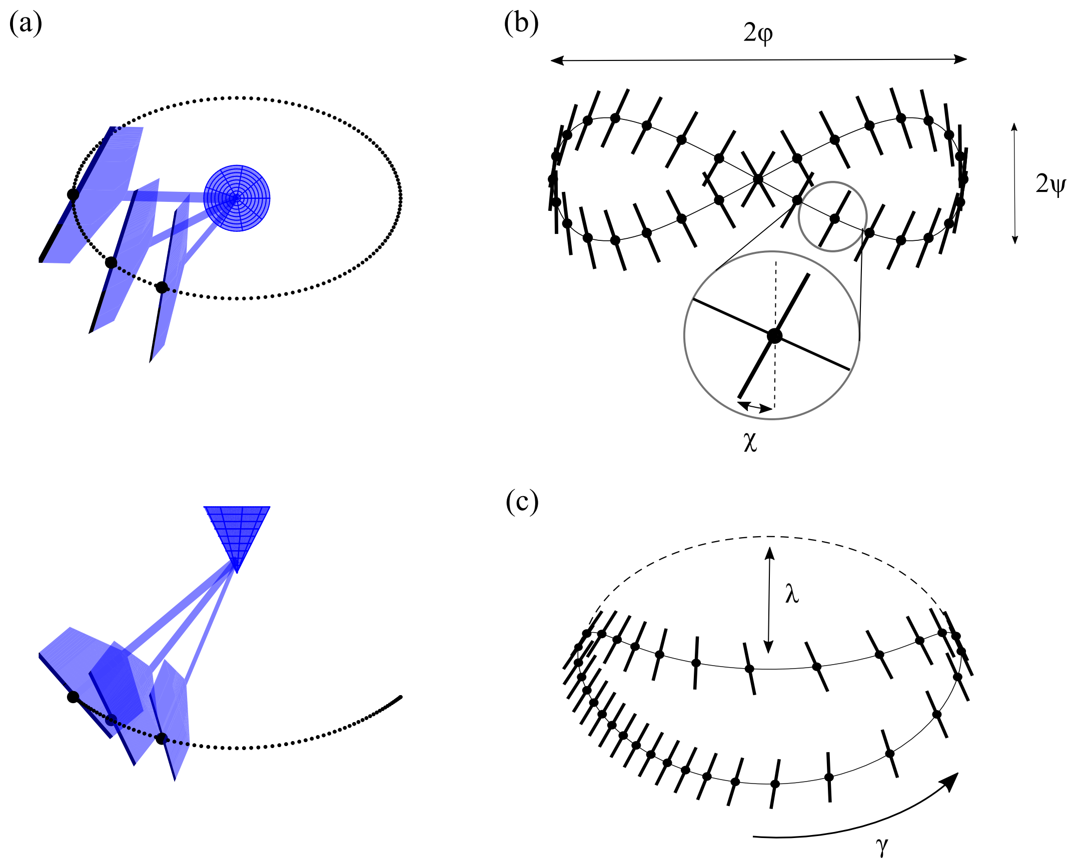

Figure 6.2: Description of fin kinematics. (a) Three-dimensional representation of the fin's motion. Back view is on top and top view is on bottom. The edge of the fin and its centerpoint are marked in black. The trajectory of the centerpoint is represented by a dashed line. The projection of the edge, centerpoint and its trajectory are used for the two-dimensional representations. (b) Definition of Stroke angle, ϕ, deviation angle, ψ, and rotation angle, χ. (c) Definition of camber, λ, and speed-up, γ.

Fitness

The objective of the optimization procedure is to obtain the best trajectory that generates a specified maneuvering force, which has been considered here to be a side force, i.e., a force in the x'-y' plane as defined in figure 6.3a, with x'-y'-z' being the laboratory reference frame. The target value of the force has been set to

$$F_{target} = 17mN$$

which is attainable with the fin geometry and experimental setup employed (Martin and Gharib, 2018). The variable to be minimized is therefore

Parameter	Symbol	Min. value	Max. value	Conv. criterion
Type	—	Figure-eight	Ellipse	Same type
Stroke angle	ϕ	20°	40°	3°
Deviation angle	ψ	0°	20°	3°
Rotation angle	χ	−70°	70°	3°
Rotation phase	β	0	2π	0.4
Rotation acceleration	K_v	0	1	0.2
Speed-up code	S	0	4	1
Speed-up value	γ	1	1.3	0.1
Camber	λ	0	1	0.2
Frequency	f	0.15 Hz	0.2 Hz	0.01 Hz

Table 6.1: Trajectory parameters, with corresponding range and convergence criteria.

$$w = \frac{|F - F_{target}|}{F_{target}}$$

The best trajectory has been defined as the trajectory which maximizes the efficiency

$$\eta = \frac{(\bar{F}_{x'}^2 + \bar{F}_{y'}^2)^{1/2}}{\overline{|F_x|}} \tag{6.1}$$

where x' and y' correspond to the laboratory reference frame and x to the wing reference frame (figure 6.3). This is a geometrical efficiency and represents the proportion of the normal forces generated by the fin that are oriented in the desired direction. It does not make any considerations with respect to the power necessary to generate the trajectory or output by the motion. Because maneuvering only occurs for small time intervals in comparison with cruising and the motion of the vehicle should be fast and well defined at those instants, it is more critical for the system to be able to perform motions in the desired direction exclusively than to do so utilizing little power. The defined efficiency responds to that need. These two objectives (closeness to target force and maximum efficiency) are combined to generate a fitness function given by

$$fit = 0.8\,w + 0.2\,|1 - \eta| \tag{6.2}$$

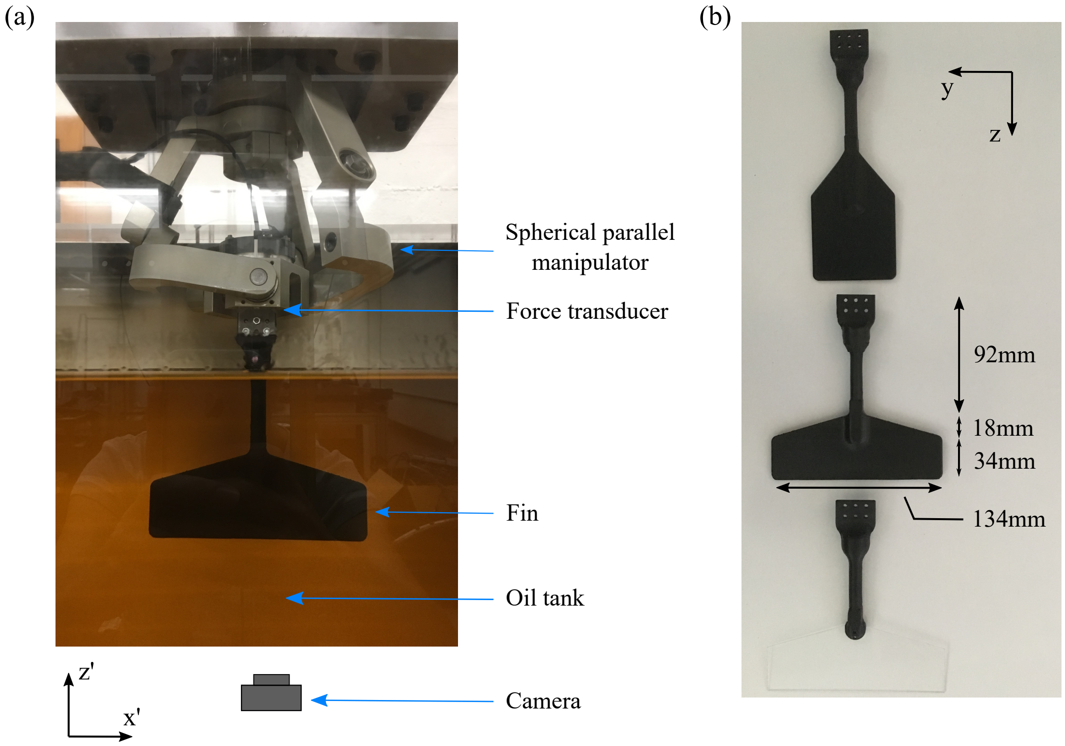

Figure 6.3: (a) Experimental setup, with laboratory frame axis (b) Fins tested with fin reference frame axis. From top to bottom AR=1, AR=4 (rigid) and AR=4 (flexible).

The value of this fitness is to be minimized in the optimization. Because it is more imperative for the force to approach the specified value than to do so efficiently, the proximity to the target force has been weighted more heavily in the fitness function. Martin and Gharib (2018) performed a sensitivity study that considered small variation in the weighting of both components, and concluded that these variations did not significantly impact the optimal trajectory obtained.

Experimental setup

A photograph of the experimental setup can be viewed in figure 6.3a. The motions are performed by a spherical parallel manipulator (SPM), which is an actuated spherical joint that can perform any three-dimensional rotation within a 50° cone (Sudki et al., 2013). The manipulator is set over an oil tank of dimensions 41cm × 50cm × 150cm. The oil (Chevron Superla White Oil #5) has a density of ρ = 835kg/m^3 and a viscosity of $\nu = 1.6\times10^{-5}$m^{2}s^{-1}. The resulting Reynolds numbers, based on the fin length, L_{fin}m and average tip velocity, U_{tip}, vary between $Re = L_{fin}U_{tip}/\nu$=270 – 900. The dimensions of the fins tested are presented in figure

6.3. The top fin was employed in the study of Martin and Gharib (2018) and has an aspect ratio of AR=1. The middle (rigid) and bottom (flexible) fins are employed in the current study and correspond to an aspect ratio of AR=4. All three fins have an equal surface area to allow for a direct comparison. The rigid portion of the fins (black) is 3D printed and the flexible portion (transparent) is cut from polycarbonate plates of density $\rho_s = 1200\text{kg/m}^3$, Young's modulus $E = 2.41$GPa and Poisson ratio $\nu = 0.38$ and varying thickness.

The forces exerted on the plate are measured using a six-axis force transducer (ATI Nano17) located at the center of rotation of the system. They are sampled at 250 Hz and the weight of the fin, taking buoyancy into account, is subtracted from the data in post-processing. Three trials, consisting of at least ten cycles each, are performed for each trajectory. The first three cycles are eliminated to avoid the analysis of initial transients. The data is then averaged to obtain the mean forces at each instant of a single cycle.

Qualitative flow visualization was performed using small air bubbles, which are particularly suited for vortex observation because they are driven into their low-pressure core. The camera is placed below the oil tank (figure 6.3a) and the bubbles are allowed to rise until those with smallest diameter reach the bottom of the fin, at which time the images are acquired. A halogen light, shined through a small slit, was employed to illuminate the tank. This results in a higher illumination at the fin height, but bubbles at multiple heights are visible. The resulting images therefore contain information for different planes, allowing to visualize the three-dimensional structures but impeding quantitative two-dimensional measurements.

Chapter 7

OPTIMAL MANEUVERING TRAJECTORY FOR FINS OF LARGE ASPECT RATIO

Nature's swimmers have evolved to adapt to their surrounding environment and mode of life. Chapter 6 has detailed the difference between large cruisers, who have developed a lift-based locomotive mechanism that results in high propulsive efficiency, and fish that dwell in reefs, who have evolved to use drag-based or combined propulsion methods that result in lower propulsive forces but higher maneuverability in the conditions they encounter. It should be clarified that these drag-based mechanisms result in higher maneuverability at low swimming velocities only. As swimming speed is increased the fin and flow velocity approach each other, and the force generated by the fin is largely reduced (Fish, 2013; Vogel, 1994). Fast swimmers typically employ lift forces to maneuver, resulting, however, in larger turning radii (Fish, 2002; Maddock et al., 1994).

Associated to these environmental and propulsive variations is a difference in body and fin morphology (Webb, 1984). Fish with different modes of life possess different sets of fins, with their shape varying according to their functionality. Low-aspect-ratio oar-type fins are more suited for drag-based paddling (Blake, 1981), while high aspect ratio fins generate lift forces more efficiently (Walker and Westneat, 2002). This improved efficiency is analogous to the reduction of drag in high-aspect-ratio wings and is a consequence of the reduction in the induced drag caused by the tip vortices. For this reason, thunniform swimmers typically possess high-aspect-ratio, lunate-shaped caudal fins (Lighthill, 1969; Sambilay Jr et al., 1990).

To achieve both high maneuverability at low velocities and high efficiency Martin and Gharib (2018) employed the current experimental setup to explore the trajectory to be followed by a fin of AR=1, which lies between those of cruisers and maneuvering specialists and was considered a good compromise for a generalist design. They performed two tests that searched for the most efficient trajectory to generate a side force of F=17mN. The first test corresponded to a fully three-dimensional trajectory. In the second test, the degrees of freedom were limited such that the trajectory of the fin's centerpoint was a straight line. The parameters of the optimal trajectories that resulted are shown in table 7.1. The 2D projection of the trajectories is shown together with the resulting forces in figures 7.1 (fully 3D trajectory) and 7.2 (trajectory limited to a line). For each interval illustrated in these figures, the motion of the fin starts at the point indicated with a diamond. To facilitate comparison, the trajectories have been rotated such that the average force is aligned with the x' direction. It must be noted that these figures have been extracted from Martin and Gharib (2018) and the notation and orientation is not fully consistent with the one employed in throughout the remaining of this text.

The trajectory that resulted from the fully three-dimensional optimization follows a paddling strategy. In the upstroke (figure 7.1a) the fin is oriented as perpendicular as possible to the x' direction, while its motion aligns as much as possible with that direction, generating a large drag force that is aligned with x'. In the downstroke (figure 7.1b) the fin aligns with the x' direction, minimizing the forces generated. The trajectory that resulted from the limited optimization is shown in figure 7.2 and seems to follow a lift-generating strategy. The fin is oriented at an angle to the direction of its motion, and the $F_{x'}$ force is positive during 82% of the cycle. It is interesting to note that the efficiency of the trajectory that is limited to a line ($\eta = 0.413$) is higher than the efficiency of the fully three-dimensional trajectory ($\eta = 364$), despite it being a subset of the latter. This highlights one of the limitations of this procedure: there is no guarantee that the optimum obtained will be a global optimum. It will represent, nonetheless, a good general strategy that achieves the desired force and constitutes an optimal configuration if considering small variations around it.

The results of Martin and Gharib (2018) demonstrate the feasibility of an AUV design that retains a rigid body and utilizes a caudal fin for both propulsion and maneuvering. The low aspect ratio of the fin selected as a compromise in their study will result, however, in reduced propulsive efficiency with respect to that achievable by higher aspect ratios. The importance of the degrees of freedom of a fish fin in its performance has been emphasized in the literature (Lauder and Drucker, 2004). While it is unlikely that the three-degree-of-freedom mechanism employed here will significantly improve the propulsive efficiency with respect to fish locomotion, it is probable that it could result in improved maneuverability. The approach of the current study is, therefore, to retain nature's thunniform design, and in particular the high aspect ratio of the fin, for high cruising efficiency and explore the ability of the mechanism to produce turning forces by performing motions that are, perhaps, not available to fish due to more restrictive physical constraints. In this chapter,

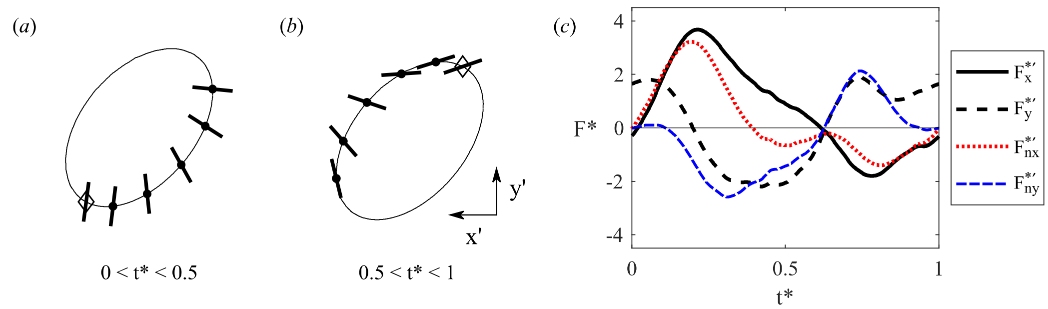

Figure 7.1: The forward stroke (a) and the backwards stroke (b) of the rotated optimal trajectory for generating side-force. The diamond corresponds to the position of the fin at the start of each stroke. The corresponding $F{*_x}'$, $F{*_y}'$, $F{*_{n_x}}'$ and $F{*_{n_x}}'$ (c) show the instantaneous phase averaged forces over a single cycle as a function of $t*$. Extracted from Martin and Gharib (2018) DOI:10.1088/1748-3190/aaefa5

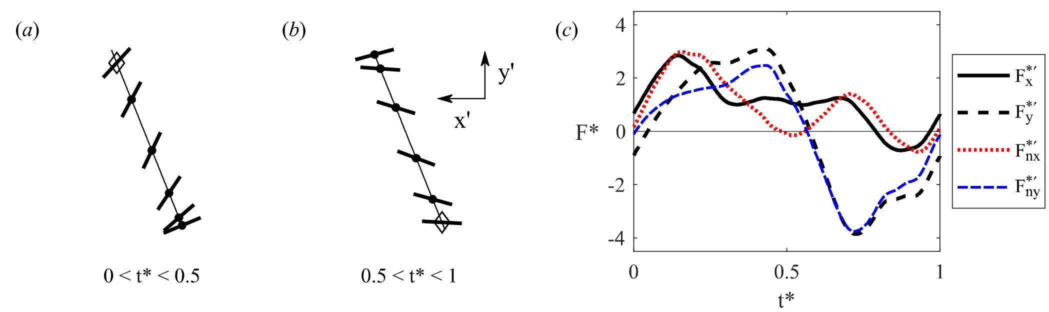

Figure 7.2: The upward stroke (a) and the downward stroke (b) of the rotated optimal trajectory for generating side-force when the trajectory is limited to a line. The diamond corresponds to the position of the fin at the start of each stroke. The corresponding $F{*_x}'$, $F{*_y}'$, $F{*_{n_x}}'$ and $F{*_{n_x}}'$ (c) show the instantaneous phase averaged forces over a single cycle as a function of $t*$.Extracted from Martin and Gharib (2018) DOI:10.1088/1748-3190/aaefa5

the optimal trajectory for a fin of aspect ratio AR=4, which is in the lower limit for the caudal fin of thunniform swimmers, will be analyzed, with the ambition of converging on a design that is not only agile but also possesses propulsive efficiencies close to those of nature.

7.1 Results

Optimal trajectory for a fin of AR=4

The optimal trajectory, as defined by equation 6.1, followed by a fin of AR=4 to generate a side force of $F_{target} = 17$mN was searched using the optimization procedure described in chapter 6. The resulting parameters are presented in table 7.1. The two-dimensional projection of the corresponding trajectory is illustrated in figure 7.3. It is divided into four segments to avoid cluttering; their temporal order is counterclockwise (I-IV). These do not correspond to equal time intervals but have rather been divided according to separate characteristic maneuvers. For simplicity of comparison, the trajectories have been rotated such that the resulting force is in the x' direction. This resulting force is plotted in figure 7.3b, together with the modulus of the forces normal and tangential to the fin (in the x and y axis represented in figure 6.3b, respectively). The forces have been non-dimensionalized with the target force $\tilde{F} = F/F_{target}$, such that the integral of $\tilde{F_{x'}}$ over a cycle is approximately equal to one, and the time has been non-dimensionalized with the period of the motion $\tilde{t} = tf$. Figure 7.3c displays the normal velocities of the two edges of the fin (blue and red, corresponding to blue and red points in figure 7.3a) and the centerpoint (black), non-dimensionalized with the average tip velocity U_{tip} over the period. The intervals corresponding to each segment I-IV of the trajectory are marked by vertical lines in this plot, as well as figure 7.3b. Unlike the trajectories obtained by Martin and Gharib (2018) for a fin of AR=1, that corresponded to paddling and lift-based mechanisms, the strategy and force generating mechanisms of the trajectory are no longer evident. As will be clarified below, several different mechanisms are combined within the single trajectory to generate the optimal strategy.

The first consideration that should be made in order to interpret the resulting trajectory is related to the wing's geometry. Wings of low aspect ratio will generate large forces when rotated around their x and y axis, as shown in figure 6.3b. This is a result of the fin and arm lengths being large compared to the other dimensions, producing substantial velocities at the wing tip that will generate large forces. Rotations around the z axis, on the other hand, will result in smaller velocities and forces. In the case of a fin of large aspect ratio, however, the width of the fin is also large, and rotations around its z axis will generate significant velocities at the edges, resulting in considerable forces. A substantial portion of the forces produced by the fin of AR=4 are generated by rotation around its z-axis. A fin that rotates around its centerpoint, however, will generate no net force. In the optimal trajectory, the motion of the centerpoint and the rotation around the fin's z axis are combined

Parameter	Symbol	AR=1 3D	AR=1 Line	AR=4 3D	AR=4 Line
Type	—	Ellipse	—	Ellipse	—
Stroke angle	ϕ	27.9°	28.3°	36.0°	36°
Deviation angle	ψ	15.7°	0°	19.9°	0°
Rotation angle	χ	63°	44.1°	−70°	−48.5°
Rotation phase	β	4.4	3.2	0	6.1
Rotation acceleration	K_v	0.2	0.1	0.2	0.5
Speed-up code	S	0	2	2	1
Speed-up value	γ	1	1.2	1	1.2
Camber	λ	0.1	0	0.4	0
Frequency	f	0.19 Hz	0.19 Hz	0.19 Hz	0.2Hz
Force	$F_{x'}$	16.95mN	16.97mN	17.07mN	16.89mN
Efficiency	η	0.364	0.413	0.829	0.555

Table 7.1: Parameters of optimal trajectories for rigid fins. Data for the fins of AR=1 has been extracted from Martin and Gharib (2018).

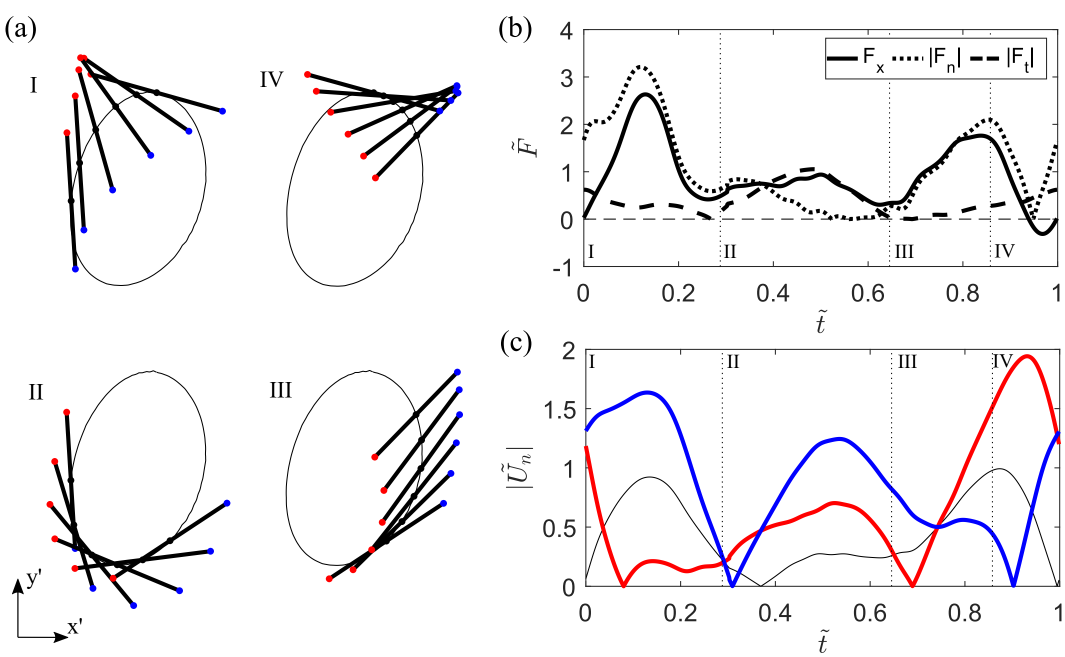

Figure 7.3: (a) Optimal trajectory for a rigid fin of AR=4, where the sequence is I-IV. (b) Resulting side force, $F_{x'}$, normal force and tangential force. (c) Normal velocity of fin edges and centerpoint, with the colors corresponding to the points in (a)

to modify the overall center of rotation, that moves towards one of the fin's edges. This is evident in segments I and IV of the trajectory, illustrated in figure 7.3. It is emphasized in figure 7.3c. During segment I of the trajectory, the velocity of the red edge decreases to zero and plateaus at a low value, while the velocity of the blue edge reaches its maximum. The fin rotates around the red edge, generating forces that are oriented in the desired direction. In segment IV of the trajectory, on the other hand, the fin rotates around the blue edge, generating forces that are still in the desired direction. This two-step rotation allows the fin to undergo large rotations around its z axis while always producing favorable forces. Segment III of the trajectory represents the opposite case; the rotation around the fin's z axis has been combined with the curvature of the centerpoint's trajectory such that practically no normal force is generated by the rotation. The motion of the fin throughout the different segments as well as the resulting fluid forces are described in detail in the following paragraphs.

The mechanism responsible for the generation of momentum during the rotation in segment I can be inferred from the geometry of the trajectory and the fin's velocity, shown in figures 7.3a and b, respectively. Because the angle swept is large and the fin is oriented perpendicularly to its motion, the possible responsible forces are either form drag or acceleration reaction. The velocity of the blue and red edges is practically constant throughout a significant part of segment I, which is inconsistent with an acceleration reaction being responsible for the large normal force. Additionally, the velocity of the blue edge decreases rapidly in the second half, which results in an added mass force in the negative x' direction. The large positive peak in $F_{x'}$ is therefore caused by a form drag force. This is further supported by the observation that the peak force and maximum velocity coincide in time. As the fin aligns its normal with the x' direction, a larger proportion of the normal force is in the desired direction, resulting in $F_{x'}$ and $|F_n|$ overlapping at the end of this rotation.

Throughout segment II of the trajectory, the fin performs a rotation such that it is positioned practically tangent to the trajectory of its centerpoint at all times, resulting in a normal force that approaches zero (figure 7.3b). The tangential force, on the other hand, sees a significant increase in this segment and is responsible for most of the force in the x' direction. Because the normal force is present in the denominator of the efficiency (equation 6.1), the presence of a force in the x' direction when the normal force is small significantly increases the value of the efficiency. Surprisingly, the tangential force is not caused by the friction drag generated by the motion of the plate, which produces a force in the negative x' direction (figure 7.3). The mechanism creating this positive tangential force is not evident, but may be related to the fin's inertia, the non-stagnant flow the fin encounters as a result of the previous stroke and unsteady mechanisms involving the vortex dynamics, which are rich in this motion. A visualization of the flow structures can be viewed in figure 7.4.

Segment III of the trajectory corresponds to a power stroke, with the main contributor to the force in the x' direction being the normal force. The motion of the fin is practically perpendicular to the force generated, which indicates that it corresponds to a lift mechanism. The value of the force follows a similar trend to that of the velocity of the fin's centerpoint, which is an indicator of a velocity-dependent force such as lift. Flow visualization (figure 7.4) reveals a vortex forming at the fin's leading edge (blue edge), which is shed towards the end of the segment.

The beginning of segment IV is characterized by a decrease in the normal force experienced by the fin, caused by the competing action of a drag force and an acceleration reaction force. The clockwise rotation of the fin generates a drag force that has a component in the positive x' and negative y' direction. Figure 7.3c, shows, however, a deceleration in the motion of the centerpoint, combined with a decrease in velocity of the blue edge that is followed by an acceleration in the opposite direction and a small increase in the velocity of the red edge followed by a deceleration. This overall deceleration results in an added mass that will generate an opposing acceleration reaction force, in the negative x' and positive y' direction, over most of the fin. As the fin crosses the horizontal position, the sign of the x' component of the normal is reversed, resulting in a negative contribution to the $F_{x'}$ force. The subsequent acceleration of the wing in the opposite rotation direction (deceleration of the red edge and acceleration of the blue edge) at the end of segment IV causes the $F_{x'}$ force to return to the positive values. The added mass force is dominant up to the time at which the velocity stagnates, which corresponds to the initial stage of segment I. An inflection point can be observed in the curve of the normal force at this point. The full cycle is then repeated to generate an overall force in the $F_{x'}$ direction.

These observations provide an outline of the general characteristics of the fin's motion and the forces produced. They do not, however, account for more complex unsteady fluid phenomena such as the shedding of vorticity and dynamics of the vortices. Unsteady flow phenomena such as delayed stall and wake capture are fundamental to the performance of insect flight (Dickinson et al., 1999), and are

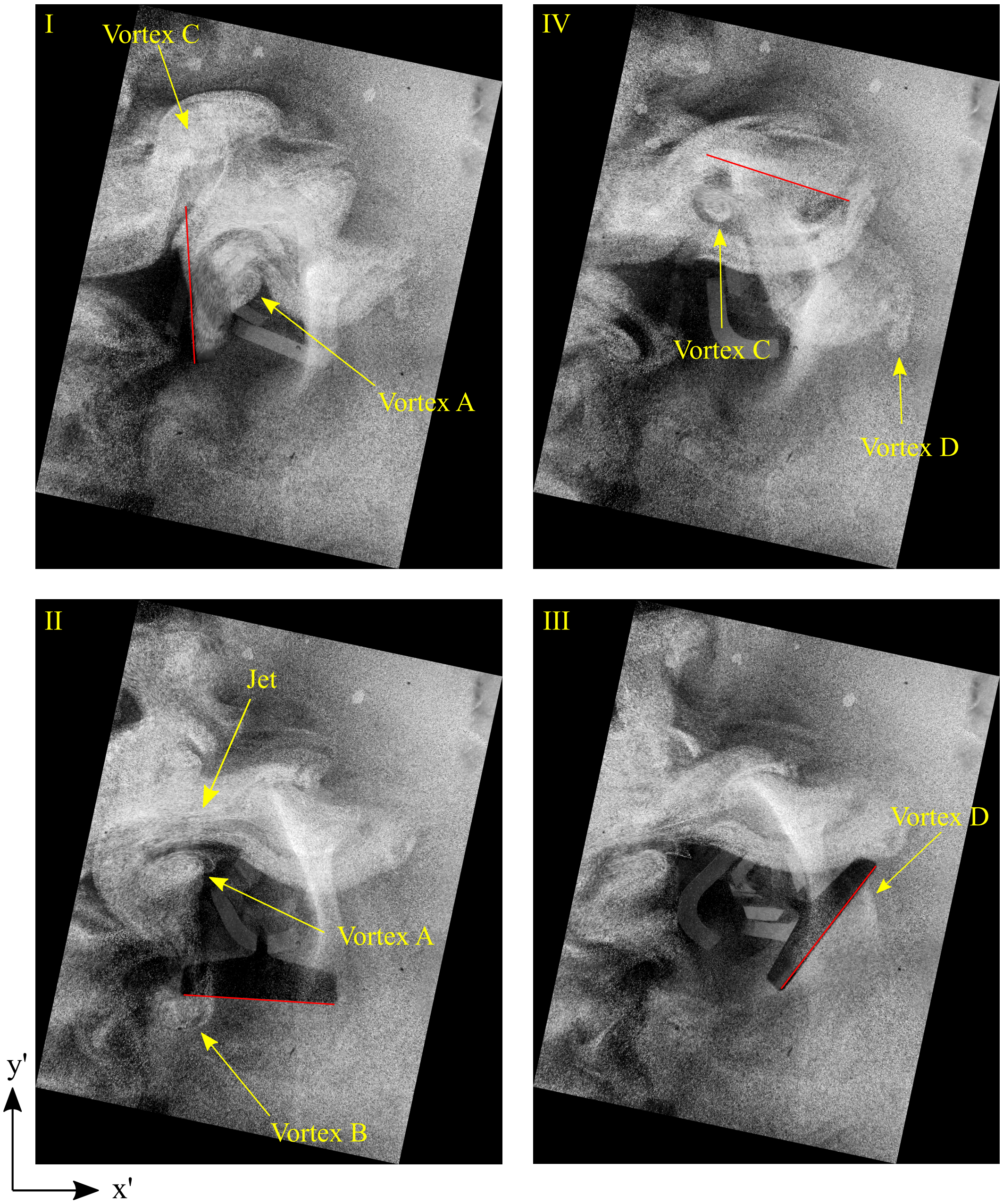

Figure 7.4: Flow visualization of the optimal trajectory obtained for a rigid fin of AR=4. The edge of the fin is highlighted in red.

likely to play an important role in this complex three dimensional fin motion. Although these vortices are not the major providers of force, their presence does alter the forces exerted on the fin and may be responsible for the optimality of the trajectory over other similar trajectories. Due to the complexity of the trajectory, a comprehensive and quantitative analysis of these effects would require three-dimensional velocimetry, which is beyond the scope of this work. Qualitative flow visualization has been performed, however, to highlight the general features of the flow. Four images are presented in figure 7.4, each corresponding to the plate in one of the four segments of its motion. In a similar manner to figure 7.3a, the temporal evolution in this figure is counterclockwise.

A leading edge vortex (vortex A, figure 7.4 I) is formed during the large rotation of segment I, where the leading edge corresponds to the blue edge in figure 7.3a. This vortex detaches close to the end of the rotation and rolls over the fin's upper surface. It is shed over the opposite red edge of the fin at the beginning of segment II. A high-velocity jet is generated in the negative x' direction (figure 7.4 II). Its velocity is imparted by the fin's motion both in segment I and segment III of the trajectory. After its detachment, vortex A moves in the negative x' direction together with this jet. A second vortex is formed in the proximity of the leading edge (blue edge) at the beginning of segment II (vortex B, figure 7.4 II). It moves along the bottom surface of the fin and is shed at the red trailing edge, continuing in a downwards (negative y') motion. A third vortex (vortex D, figure 7.4 III) starts forming at the fin's leading edge at the beginning of segment III and is shed at towards the end of the segment. The shed vortex tube can be observed in figure 7.4 IV. It is interesting to note that the motion of the fin in segment III induces a flow with velocity in the positive y' direction, which is encountered by the fin in its downward motion in segment I and enhances the drag force produced. An additional leading edge vortex (vortex C, figure 7.4 IV) is generated at the bottom surface leading edge (red edge) of the fin during the rotation in segment IV. A second vortex, not pictured here, is formed at the top surface at the end of this rotation. Both of these vortices are shed at the red edge as the fin's displacement direction shifts and move upwards (in the positive y' direction) as a vortex pair. Although a simplified description has been provided, as is visible in these images the vortex dynamics of the motion are quite complex, with components in all three dimensions and vorticity being generated in the top and bottom edges of the fin in addition to the blue and red leading edges.

Effect of three-dimensionality and large rotation

The benefits of employing a mechanism that allows for large rotations and three-dimensional motion to generate maneuvering forces with a high aspect ratio fin is now analyzed. The trajectory parameters that are characteristic of this type of motion are the deviation angle, ψ, and the rotation angle, χ, as described in figure 6.2b. Due to physical constraints, the values of both of these variables are very limited in the motions achievable by the caudal finds of thunniform swimmers. The values of these parameters for the optimal trajectory can be found in table 7.1, while the limits on these variables set for this optimization can be viewed in table 6.1. Notably, both the deviation angle and the rotation angle of the optimal trajectory are both at their maximum absolute values (ψ=20°, $\chi = -70°$), which highlights the importance of the parameters in performing efficient maneuvering motions and explains the absence of such a trajectory in nature.

In order to further consider the effect of the trajectory's three-dimensionality, the optimization algorithm was employed to obtain the optimal trajectory that generates a side force of $F_{x'} = 17mN$ considering only the family of trajectories whose centerpoint motion is limited to a straight line. This is performed by setting the values of the deviation angle and camber to zero. The parameters of the resulting optimal trajectory are shown in table 7.1. The average force obtained approaches reasonably well the target force. The efficiency of the trajectory is, however, significantly lower than that of the fully three-dimensional case, being comparable to that obtained by Martin and Gharib (2018) for a fin of AR=1.

The trajectory's two-dimensional projection is shown in figure 7.5a, where the starting point of the fin at each of the two segments is marked with a square. The corresponding forces and velocities have been plotted in figures 7.5b and c, respectively, in a similar manner to figure 7.3. The trajectory has been rotated such that the average force is in the x' direction. In a similar manner to a paddling motion, the trajectory followed by the fin is divided into a power stroke (segment I) and a recovery stroke (segment II). The majority of the favorable force is generated during the power stoke, while the recovery stroke is limited to reducing the forces generated.

Using a similar argument to that of the three-dimensional trajectory, the principal mechanism responsible for the large normal force in the power stroke can be determined to be drag: while the plate is decelerating in the second half of the stroke, the force is still in the positive x' direction. It follows closely, additionally, the curve of

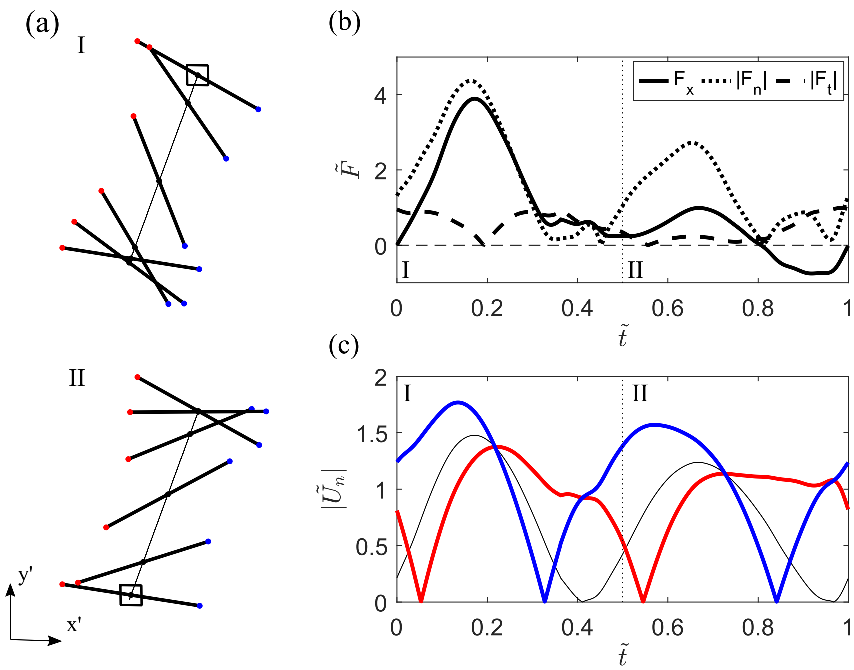

Figure 7.5: (a) Optimal trajectory for a rigid fin of AR=4 when its centerpoint motion is constrained to a line, where the initial position is marked by a square (b) Resulting side force, $F_{x'}$, normal force and tangential force. (c) Normal velocity of fin edges and centerpoint, with the colors corresponding to the points in (a)

the centerpoint velocity. In this constrained case, there is no possibility of combining the centerpoint motion and fin rotation around its z axis to produce favorable large drag-producing turns; although the velocity of the red edge decreases to zero, which must always be the case, it does not remain at a low value. The forces in this stroke are generated, in their majority, by the rotation around the fin's y axis, as represented in figure 6.3, and the parameters of the trajectory have converged accordingly to maximize the force in this power stroke. The speed up value, $\gamma = 1.2$, is high, with the speed code being S=1, which corresponds to a speed up in the power stroke. This results in a peak force that is higher than that of the three-dimensional case. The rotation acceleration, $K_v = 0.5$, is higher than in the three-dimensional case, which results in the fin's rotation being concentrated at the edges of the trajectory, while only small rotations occur at the center. Notably, significant tangential forces are present during the rotation of the fin at the edges of the trajectory and are responsible for a large proportion of the force in the x' direction in those intervals. The origin of this tangential force is not clearly distinguishable, but may be related to inertial effects and vortex dynamics, which are known to be a significant factor in the rotation at stroke reversal for insect flight (Dickinson et al., 1999). While the forces generated at stroke reversal of the optimal trajectory are favorable at the end of the power stroke, they are detrimental at the end of the recovery stroke. During the recovery stroke, the force in the x' direction is small, with the majority of the normal force being oriented in the y' direction. The normal force in the recovery stroke, in a similar manner to the power stroke, is mostly a result of form drag.

It is interesting to note that the rotation angle of this optimal trajectory, $\chi = -48.5°$, is still high in comparison to the rotations achievable by the caudal fins of thunniform swimmers. It therefore constitutes an improvement with respect to the traditional bio-mimetic maneuvering fin motions. Despite this fact, the efficiency is significantly lower than that of the fully three-dimensional case.

7.2 Conclusions

The optimal trajectory that generates a side force of $F_{x'} = 17mN$ for a fin of aspect ratio AR=4 has been obtained utilizing an experimental optimization procedure. The optimum obtained possesses a high deviation angle (i.e., high three-dimensionality) and high rotation angle, which are achievable by the current mechanism but not by the caudal fin of fish due to mechanical constraints. This trajectory results in a remarkably high efficiency, which is twice as large as the optimal trajectory obtained by Martin and Gharib (2018) for a fin of AR=1.

The optimal trajectory uses the combination of four different maneuvers to generate forces efficiently. In the first segment of the trajectory, the plate combines the motion of its centerpoint with the rotation around its z axis to produce an overall rotation that results in a high favorable drag force. In the second segment, the fin moves practically tangentially to the trajectory of its centerpoint, reducing the normal force but generating a tangential force with a component in the x' direction. In the third segment the fin employs a lift mechanism to generate a second high $F_{x'}$ peak. The final fourth segment corresponds to a rotation, where the fin does not generate significant favorable forces but decelerates to its initial position without producing detrimental effects.

A second optimization, where the trajectory of the centerpoint was limited to a line, was performed and a paddling-type strategy was recovered. The sharp decrease in efficiency highlighted the importance of three-dimensionality in generating an efficient turning maneuver for fins of high aspect ratio. Because the propulsive efficiency of lift-based flapping propellers has been shown to be higher for fins of large aspect ratio, the utilization of a mechanism that allows for these high rotations and high three-dimensionality in the fin’s motion, and can therefore generate side forces efficiently for large aspect ratio fins, is a promising candidate for an unmanned underwater vehicle that requires both high propulsive efficiency and high maneuverability.

Chapter 8

EFFECT OF FIN FLEXIBILITY ON THE OPTIMAL TRAJECTORY

The structure that reinforces the caudal fin of fish is generally comprised by a set of fin rays, that can be bony or cartilaginous and support a softer collagenous membrane (Lauder, 2000; Lingham-Soliar, 2005). Both the fin rays and the membrane are compliant, with the Young's modulus of bony rays being of the order of 1GPa and that of the membrane of 0.3–1 MPa (Lauder and Madden, 2007). Flexibility is a common feature in the propelling surfaces of most animals (Lucas et al., 2014) and results in significant deformations occurring with the propeller motion. The effect of flexibility on the propulsive characteristics of lift-producing caudal fins and wings has been studied extensively, with variable results being reported.

Many of these studies have focused on the simplified problem of heaving and pitching motions of airfoils. An experimental investigation by Prempraneerach et al. (2003) reported an increase of up to 36% in efficiency with a small decrease in thrust for airfoils with chordwise flexibility performing combined heaving and pitching motions. Heathcote et al. (2008) observed an increase in both efficiency and thrust for small values of spanwise flexibility in the heaving motion of a wing of AR=3, while larger compliances resulted in detrimental effects. Simplified theoretical models typically make use of flat plate geometries and inviscid fluid formulations. Katz and Weihs (1978) analyzed the performance of a plate whose leading edge performed a harmonic oscillation, and found increases of up to 20% in efficiency when chordwise flexibility was introduced, with small decreases in thrust. More recent results of a plate in pitching (Alben, 2008) and heaving (Michelin and Llewellyn Smith, 2009) motion found a series of peaks at which the thrust production increased, with regions where the chordwise flexibility produced higher efficiencies. Numerical studies have reached similar conclusions. Liu and Bose (1997) observed a decrease in propulsive efficiency with passive spanwise flexibility, but reported an increase with carefully controlled flexibility, and Zhu (2007) reported an increase in efficiency with chordwise flexibility, while spanwise flexibility was always detrimental when considering motions in a heavy fluid. Overall, these studies have established the benefits of utilizing propellers within specific optimal flexibility ranges. Deviations from these optimal compliance values, however, commonly resulted in reduced performance.

The effect of compliance on the maneuverability of these fins has received, on the other hand, little attention. Kim and Gharib (2011a) and Kim and Gharib (2011b) investigated the thrust performance of flexible fins for drag-based paddling propulsion, which provides some insight into the behavior of flexible fins performing drag-based maneuvering. They reported a markedly different vortex formation process for an impulsively translating flexible fin compared to that of rigid fins, both flat and curved. These differences resulted in a smaller initial force peak for the flexible fin, which was able, however, to maintain a larger force after this initial peak due to slower vortex development.

These results have highlighted the potential of employing a compliant fin to improve the thrust and propulsive efficiency of a lift-based flapping propeller. Because the maneuvering capabilities of a fin are dependent on rapid, large forces the ability to utilize such a fin for fast turning is yet to be determined. The objective of this chapter is, therefore, to research the effect of fin flexibility in the optimal three-dimensional trajectory that generates a maneuvering side force, with the view of a mechanism that utilizes the same fin for propulsion and maneuvering purposes, such as the one considered here.

8.1 Results

The optimal trajectory, as defined by equation 6.1, followed by a fin of AR=4 and varying flexibility to generate a side force of $F_{target} = 17$mN was searched using the optimization procedure described in Chapter 6. The fins had a rigid arm and a flexible main surface made of polycarbonate (see figure 6.3b), with thicknesses of $h_1 = 0.762$ mm, $h_2 = 0.508$ mm and $h_3 = 0.254$ mm which constitute flexural rigidities of $D_1 = 0.1$ Pa m^3, $D_2 = 0.03$ Pa m^3 and $D_3 = 0.004$ Pa m^3, respectively. The parameters of the resulting optimal trajectories are presented in table 8.1, together with those obtained for the rigid fin of Chapter 7. The similarity between the trajectories is remarkable, and emphasizes the effectiveness of the identified strategy. The four segments or maneuvers described in detail in Chapter 7 are employed by all four fins. The flexible fins, however, were observed to deform in their motion (figure 8.2), generating differences in the forces produced and their direction. Due to this deformation, the position of the surface of flexible fins cannot be easily obtained at every instant, requiring three-dimensional tracking of the structure, which has not been performed in the current work. The motion of

Parameter	Symbol	Rigid	h=0.76mm	h=0.51mm	h=0.25mm
Type	—	Ellipse	Ellipse	Ellipse	Ellipse
Stroke angle	ϕ	36.0°	38.3°	33.5°	39.6°
Deviation angle	ψ	19.9°	20°	20°	14.6°
Rotation angle	χ	−70°	−70°	−70°	−70°
Rotation phase	β	0	0	0	0.2
Rotation acceleration	K_v	0.2	0	0.2	0.1
Speed-up code	S	2	3	3	0
Speed-up value	γ	1	1	1.1	1.2
Camber	λ	0.4	0.4	0	0.3
Frequency	f	0.19 Hz	0.18Hz	0.2Hz	0.2Hz
Force	$F_{x'}$	17.07mN	17.24mN	17.13mN	17.14mN
Efficiency	η	0.829	0.739	0.700	0.605

Table 8.1: Parameters of optimal trajectories for flexible fins.

these fins disregarding their deformation is very similar to that represented in figure 7.3 for the rigid fin, and has therefore not been included here.

The force diagrams, on the other hand, see significant differences and are represented in figure 8.1. For an approximate correspondence between instantaneous force and fin motion the reader is referred to figure 7.3. In the case of a flexible plate, the normal and tangential vectors vary along the plate's surface and are dependent on its deformation, which is not known a priori. The normal and tangential directions have been defined in this chapter as the normal and tangential directions of a rigid fin with the same rotation values as the flexible fin. Because the deformations are relatively small, this approximation provides a good representation of the directionality of the forces. A clarification should be made, however, about the efficiency. Since the definition of efficiency includes the value of the normal force in the denominator, it does not represent the exact same ratio for rigid and flexible plates. Due to the small deflections the differences are small enough, however, that a reasonable comparison may still be made.

The trajectory obtained for the stiffest of the flexible fins ($h_1 = 0.762$ mm), is almost identical to that obtained for the rigid fin. Although slight variations are present in stroke angle, rotation acceleration and frequency, these are within the

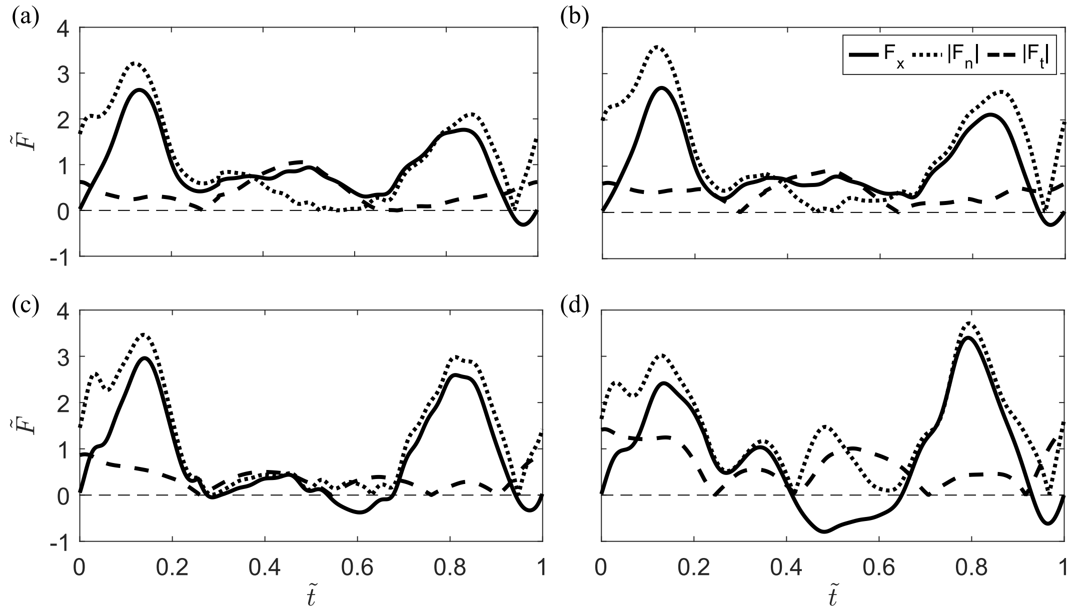

Figure 8.1: Forces generated during the optimal trajectory of the (a) rigid fin and flexible fins of thickness (b)h=0.76mm (c)h=0.51mm and (d) h=0.25mm

convergence criteria established for the optimization (table 6.1). It is interesting to note that, despite moving at a lower frequency and only small variations in stroke angle, the trajectory for the flexible plate has converged to a slightly higher force than that of the rigid plate. Because the target force has been set to $F_{x'} = 17mN$, this does not imply that the rigid plate is not capable of generating such forces, but it does highlight the ability of the flexible plate to produce high enough forces in its motion. The efficiency of the trajectory obtained by the flexible fin, $\eta = 0.74$, is, however, lower than that of the rigid plate $\eta = 0.83$, albeit moderately so. The cause of this reduction in efficiency is visible in the force measurements presented in figure 8.1, where figure 8.1(a) corresponds to the rigid fin and 8.1(b) to the least flexible case. The curve of the $F_{x'}$ force is similar between both cases, with the peak corresponding to segment III of the trajectory being slightly sharper in the flexible fin to compensate for a slightly lower value in segment II. The normal force, on the other hand, sees more significant variations. The flexible fin presents higher normal force values both in section I and III of the trajectory. This implies that the deflection of the plate causes a smaller proportion of the normal force to be in the desired x' direction during these two power motions. Because the averaged $F_{x'}$ force is approximately equal, the flexible fin will require the production of a higher normal force, which results in a lower efficiency.

The optimal trajectory corresponding to the fin of middle flexural rigidity (h_2 = 0.508mm) produces a lower efficiency, η = 0.70, than that of both rigid and stiffer flexible fins. In this case, however, the decay in efficiency is not produced in segments I and III, with the proportion of the normal force that is directed in the x' direction being similar to that of the rigid plate (figure 8.1c). While most of the normal force at the start of segment II is directed in the x' direction, no surge in tangential force occurs once the normal force decays. This may be due to the deformation of the fin, that generates a curvature on its surface. This curvature modifies the force direction and affects the formation and shedding of vortices, which play an important role in the force generation during this segment. The lack of a tangential force constitutes a detrimental effect on itself, because, as specified in Chapter 7, a tangential force with an x' component has a significant positive impact on the efficiency. In addition to this reduced tangential force, the direction of the small generated forces is detrimental, producing a net force in the negative x' direction at the end of segment II (starting approximately when the fin is located at the major axis of the ellipse) and beginning of segment III. The decrease in both normal and tangential forces in segment II of the trajectory is associated to the increase in the trajectory's frequency. Because the overall force must remain at $17mN$, the forces in the other segments, which are mostly drag-based, must increase. This is achieved by utilizing a higher velocity. There is, in particular, a substantial increase in the peak force produced in segment III, that may be additionally related to release of stored strain energy in the deformed fin. Overall, the efficiency decrease is not sharp, and the fin is capable of generating the required force. If such a degree of flexibility is largely beneficial to the propulsive efficiency of the system, it may constitute a reasonable compromise.

As the rigidity of the fin is decreased, the efficiency drops further, with the most compliant fin presenting an efficiency of η = 0.61. At this h_3 = 0.254 mm, the values of the optimal parameters start to deviate substantially from those of the rigid fin. Although the general strategy remains equal to that of the rigid case, the forces generated are considerably disparate. A second peak in normal force, directed along the x' axis, appears after segment I of the trajectory and may be produced by the release of strain energy accumulated during the power stroke of segment I. Throughout, considerable tangential forces are generated, no doubt due to the higher curvature of the deformed fin, that increases the cross-sectional surface when the fin undergoes tangential motions and modifies the force direction when it undergoes normal motions. An effect similar to that present in the fin of thickness

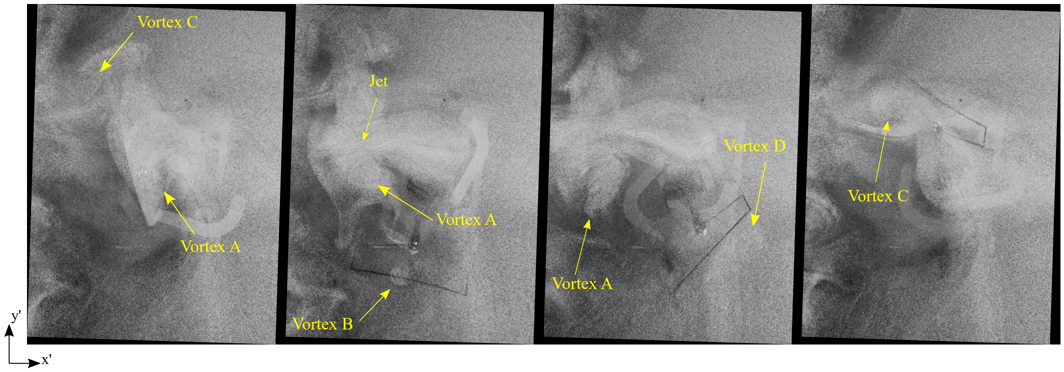

Figure 8.2: Visualization of the fin deflection and flow patterns during the optimal trajectory for a flexible fin of thickness h=0.25mm

h_2 = 0.508mm is present, where $F_{x'}$ becomes negative in segment II. The length of this negative interval, as well as the minimum force are largely increased. The peak force generated in segment III increases commensurately, with the average force being maintained at $F_{x'} = 17.14mN$. Although this optimal trajectory is capable of generating the desired force, the use of this higher flexibility generates larger forces in undesired directions, which reduce the efficiency and may pose a complication when performing maneuvering motions. Despite this larger decrease, the efficiency of this trajectory is still significantly higher than that obtained for a rigid plate when its centerpoint motion was limited to a line, evaluated in Chapter 7, further emphasizing the critical importance of employing three-dimensional motions and large rotations when attempting to generate side forces with a flexible fin.

Qualitative flow visualization was performed on the flexible fins, and showed a similar vortex structure to that present in the optimal motion of the rigid fin. The timing of vortex formation and shedding, as well as subsequent vortex dynamics display variations. Images of the visualization for the most flexible fin (h_3 = 0.254 mm) are presented in figure 8.2, where the deformation of the fin is also visible. Despite presenting the smallest opposition of all three cases, the deformations of this fin are still modest. The vortices present in these images are similar to those of the rigid case. A leading edge vortex (vortex A) is generated during segment I and is later shed over the fin's trailing edge. A second leading edge vortex (vortex B) is generated at the start of segment II. In this case, however, it detaches close to the fin's leading edge and does not follow a downwards motion. The markedly different behavior of this vortex may be a significant contributor to the detrimental forces generated in segment II of the flexible fin's motion. A third large vortex (vortex D) is generated during segment III and is shed at the start of the large rotation in segment IV. A final vortex (vortex C) is generated in this rotation and follows an upwards motion after detachment. A similar high-velocity jet is generated and moves in the negative x' direction.

8.2 Conclusions

Flexible fins have been proven in the literature to improve the thrust performance of flapping propellers for specific fin compliance values. The effect of adding a degree of flexibility to the fin on the maneuvering performance of a three-degree of rotation mechanism was investigated. The optimal trajectory for fins of three different flexibilities was obtained, with all three cases being remarkably similar to that of a rigid fin.

The flexible fins were capable of generating the target side force, $F_{x'}$, but did so with lower efficiency than the rigid fin. While the stiffer fins saw a smaller reduction in efficiency, the efficiency decreased as fin flexibility increased. It may, therefore, be possible to find a compromise value of the fin compliance where the propulsive efficiency is benefited from flexibility without largely reducing the maneuvering efficiency. Reductions in the efficiency of the flexible plates are a result of a combination of factors related to the deformation of the plate, including the modification of the force directionality and value, modification of the vortex formation processes and modification of the timing between fluid and fin dynamics.

Chapter 9

CONCLUDING REMARKS AND FUTURE WORK

Flapping propellers have received recent attention as a quiet and efficient alternative to traditional screw propellers for use in AUVs. Part II of this thesis has focused on the study of the maneuverability properties of a caudal-fin-type propeller that can perform large rotations in all three degrees of freedom. Employing an experimental optimization procedure, the parameters of the optimal trajectory that generates a specified side force have been obtained, with optimality being defined as maximum geometrical efficiency. Chapter 7 has considered the effect of aspect ratio on the resulting optimal trajectory. A fin of AR=4, that corresponds to the efficient lift-producing fins of thunniform swimmers, was considered. The resulting optimal trajectory presented and efficiency double of that of the optimal trajectory for a fin of AR=1 and is dependent on the use of high three-dimensionality and large rotations, which explains its absence in nature. The effect of introducing a degree of compliance on the fin's performance was evaluated in Chapter 8 and shown to be detrimental to the maneuverability efficiency, although the target force was achieved.

These results demonstrate the potential of employing a caudal-fin inspired propeller for the maneuvering of AUVs. A considerable amount of research, however, remains to be performed to fully characterize the performance of such a mechanism. In terms of the obtained results, a full understanding of the optimal trajectory would require a quantitative measurement of the flow and vortex features employing techniques such as 3D PIV, as well as the tracking of the fin deformation in the flexible case. Because a global optimum is not guaranteed, it would be beneficial to perform several repetitions of the optimization procedure with varying initial conditions. This is especially the case for the flexible fins, whose optimization was initiated at the optimal trajectory for the rigid fin. Although the strategy followed by the rigid fin is extremely efficient, causing the fast convergence of the flexible fins, it may be the case that a completely different strategy could result in an improved performance in the flexible case. In addition to the aspect ratio, the morphology of the fin has been proven to be an important factor in the performance of animal locomotion; experiments that consider the effect of the fin's shape will undoubtedly yield interesting results.

Several additional aspects related to the performance of the system when attached to the underwater vehicle have not been considered. The current experiments have been performed in an oil tank and correspond to the maneuverability of the AUV at rest. In most cases, however, the vehicle will need to perform maneuvers when it is in motion. The implementation of similar experiments in the presence of a co-flow are therefore an important step towards the development of a fully functional mechanism. In this direction, the interaction of the AUV body with the fin should be considered, both in terms of the modifications it produces in the incoming flow and its inertia and corresponding added mass when generating turns. Combining these two steps, the final objective would be to test a full AUV that is free to move within the tank. This final step is vital to the evaluation of the maneuvering performance, because, even though the average force in the y' direction is zero by definition, the composition of rotations during the maneuver may still provoke a final overall turn in an undesired direction. Considering a different measure of efficiency in the performance of the optimization may also be conductive to a reduction of these detrimental turns.

In conclusion, this research has shown the effectiveness of introducing high three-dimensionality and high rotations in the maneuvering performance of a high-aspect-ratio caudal-fin type propeller. Because high-aspect-ratio propellers are known to result in higher propulsive efficiencies, the mechanism investigated in this work shows promise as an efficient and quiet combined maneuvering and propulsive system for AUV use, that eliminates the need for additional surfaces or mechanisms and allows the utilization of a rigid main body.

BIBLIOGRAPHY TO PART II

S. Alben. Optimal flexibility of a flapping appendage in an inviscid fluid. *Journal of Fluid Mechanics*, 614:355–380, 2008.

G. J. Berman and Z. J. Wang. Energy-minimizing kinematics in hovering insect flight. *Journal of Fluid Mechanics*, 582:153–168, 2007.

R. Blake. Influence of pectoral fin shape on thrust and drag in labriform locomotion. *Journal of Zoology*, 194(1):53–66, 1981.

J. Carlton. *Marine propellers and propulsion*. Butterworth-Heinemann, 2007.

A. J. Clark, J. M. Moore, J. Wang, X. Tan, and P. K. McKinley. Evolutionary design and experimental validation of a flexible caudal fin for robotic fish. In *Artificial Life Conference Proceedings 12*, pages 325–332. MIT Press, 2012.

E. De Margerie, J. Mouret, S. Doncieux, and J. Meyer. Artificial evolution of the morphology and kinematics in a flapping-wing mini-uav. *Bioinspiration & biomimetics*, 2(4):65, 2007.

M. H. Dickinson, F.-O. Lehmann, and S. P. Sane. Wing rotation and the aerodynamic basis of insect flight. *Science*, 284(5422):1954–1960, 1999.

F. E. Fish. Comparative kinematics and hydrodynamics of odontocete cetaceans: morphological and ecological correlates with swimming performance. *Journal of Experimental Biology*, 201(20):2867–2877, 1998.

F. E. Fish. Balancing requirements for stability and maneuverability in cetaceans. *Integrative and Comparative Biology*, 42(1):85–93, 2002.

F. E. Fish. Advantages of natural propulsive systems. *Marine Technology Society Journal*, 47(5):37–44, 2013.

G. Griffiths. *Technology and applications of autonomous underwater vehicles*, volume 2. CRC Press, 2002.

N. Hansen. The cma evolution strategy: a comparing review. In *Towards a new evolutionary computation*, pages 75–102. Springer, 2006.

N. Hansen and A. Ostermeier. Completely derandomized self-adaptation in evolution strategies. *Evolutionary computation*, 9(2):159–195, 2001.

S. Heathcote, Z. Wang, and I. Gursul. Effect of spanwise flexibility on flapping wing propulsion. *Journal of Fluids and Structures*, 24(2):183–199, 2008.

N. Kato and H. Liu. Optimization of motion of a mechanical pectoral fin. *JSME International Journal Series C Mechanical Systems, Machine Elements and Manufacturing*, 46(4):1356–1362, 2003.

J. Katz and D. Weihs. Hydrodynamic propulsion by large amplitude oscillation of an airfoil with chordwise flexibility. *Journal of Fluid Mechanics*, 88(3):485–497, 1978.

D. Kim and M. Gharib. Characteristics of vortex formation and thrust performance in drag-based paddling propulsion. *Journal of Experimental Biology*, 214(13): 2283–2291, 2011a.

D. Kim and M. Gharib. Flexibility effects on vortex formation of translating plates. *Journal of Fluid Mechanics*, 677:255–271, 2011b.

G. V. Lauder. Function of the caudal fin during locomotion in fishes: kinematics, flow visualization, and evolutionary patterns. *American Zoologist*, 40(1):101–122, 2000.

G. V. Lauder and E. G. Drucker. Morphology and experimental hydrodynamics of fish fin control surfaces. *IEEE journal of oceanic engineering*, 29(3):556–571, 2004.

G. V. Lauder and P. G. Madden. Fish locomotion: kinematics and hydrodynamics of flexible foil-like fins. *Experiments in Fluids*, 43(5):641–653, 2007.

M. Lighthill. Hydromechanics of aquatic animal propulsion. *Annual review of fluid mechanics*, 1(1):413–446, 1969.

T. Lingham-Soliar. Caudal fin in the white shark, carcharodon carcharias (lamnidae): a dynamic propeller for fast, efficient swimming. *Journal of Morphology*, 264 (2):233–252, 2005.

P. Liu and N. Bose. Propulsive performance from oscillating propulsors with spanwise flexibility. *Proceedings of the Royal Society of London. Series A: Mathematical, Physical and Engineering Sciences*, 453(1963):1763–1770, 1997.

K. N. Lucas, N. Johnson, W. T. Beaulieu, E. Cathcart, G. Tirrell, S. P. Colin, B. J. Gemmell, J. O. Dabiri, and J. H. Costello. Bending rules for animal propulsion. *Nature communications*, 5:3293, 2014.

L. Maddock, Q. Bone, and J. M. Rayner. *The Mechanics and Physiology of Animal Swimming*. Cambridge University Press, 1994.

A. D. Marchese, C. D. Onal, and D. Rus. Autonomous soft robotic fish capable of escape maneuvers using fluidic elastomer actuators. *Soft Robotics*, 1(1):75–87, 2014.

N. Martin and M. Gharib. Experimental trajectory optimization of a flapping fin propulsor using an evolutionary strategy. *Bioinspiration & biomimetics*, 14(1): 016010, 2018.

N. K.-H. Martin. *Analysis of flapping propulsion: comparison, characterization, and optimization*. PhD thesis, California Institute of Technology, 2018.

S. Michelin and S. G. Llewellyn Smith. Resonance and propulsion performance of a heaving flexible wing. *Physics of Fluids*, 21(7):071902, 2009.

M. Milano and M. Gharib. Uncovering the physics of flapping flat plates with artificial evolution. *Journal of Fluid Mechanics*, 534:403–409, 2005.

M. M. Plucinski, Y. L. Young, and Z. Liu. Optimization of a self-twisting composite marine propeller using genetic algorithms. In *16th International conference on composite materials, Kyoto, Japan*, 2007.

P. Prempraneerach, F. Hover, and M. S. Triantafyllou. The effect of chordwise flexibility on the thrust and efficiency of a flapping foil. *Proceedings Unmanned, Untethered Submersible Technology*, 2003.

T. Rakotomamonjy, M. Ouladsine, and T. L. Moing. Modelization and kinematics optimization for a flapping-wing microair vehicle. *Journal of Aircraft*, 44(1): 217–231, 2007.

J. J. Rohr and F. E. Fish. Strouhal numbers and optimization of swimming by odontocete cetaceans. *Journal of Experimental Biology*, 207(10):1633–1642, 2004.

D. Roper, S. Sharma, R. Sutton, and P. Culverhouse. A review of developments towards biologically inspired propulsion systems for autonomous underwater vehicles. *Proceedings of the Institution of Mechanical Engineers, Part M: Journal of Engineering for the Maritime Environment*, 225(2):77–96, 2011.

V. C. Sambilay Jr et al. Interrelationships between swimming speed, caudal fin aspect ratio and body length of fishes. *Fishbyte*, 8(3):16–20, 1990.

M. Sfakiotakis, D. M. Lane, and J. B. C. Davies. Review of fish swimming modes for aquatic locomotion. *IEEE Journal of oceanic engineering*, 24(2):237–252, 1999.

Z. Su, J. Yu, M. Tan, and J. Zhang. Implementing flexible and fast turning maneuvers of a multijoint robotic fish. *IEEE/ASME Transactions on Mechatronics*, 19(1): 329–338, 2014.

B. Sudki, M. Lauria, and F. Noca. Marine propulsor based on a three-degree-of-freedom actuated spherical joint. In *Proceedings of the 3rd International Symposium on Marine Propulsors*, pages 481–485, 2013.

A. H. Techet. Propulsive performance of biologically inspired flapping foils at high Reynolds numbers. *Journal of Experimental Biology*, 211(2):274–279, 2008.

M. S. Triantafyllou, G. Triantafyllou, and D. Yue. Hydrodynamics of fishlike swimming. *Annual review of fluid mechanics*, 32(1):33–53, 2000.

I. H. Tuncer and M. Kaya. Optimization of flapping airfoils for maximum thrust and propulsive efficiency. *AIAA journal*, 43(11):2329–2336, 2005.

S. Vogel. *Life in moving fluids*. Princeton University Press, 1994.

J. A. Walker and M. W. Westneat. Performance limits of labriform propulsion and correlates with fin shape and motion. *Journal of Experimental Biology*, 205(2): 177–187, 2002.

P. W. Webb. Form and function in fish swimming. *Scientific American*, 251(1): 72–83, 1984.

L. Wen, T. Wang, G. Wu, and J. Liang. Quantitative thrust efficiency of a self-propulsive robotic fish: Experimental method and hydrodynamic investigation. *IEEE/ASME Transactions on Mechatronics*, 18(3):1027–1038, 2013.

Q. Zhu. Numerical simulation of a flapping foil with chordwise or spanwise flexibility. *AIAA journal*, 45(10):2448–2457, 2007.

Appendix A

EXPERIMENTAL MEASUREMENTS OF INVERTED FLAGS OF AR=2 AT MODERATE ANGLES OF ATTACK

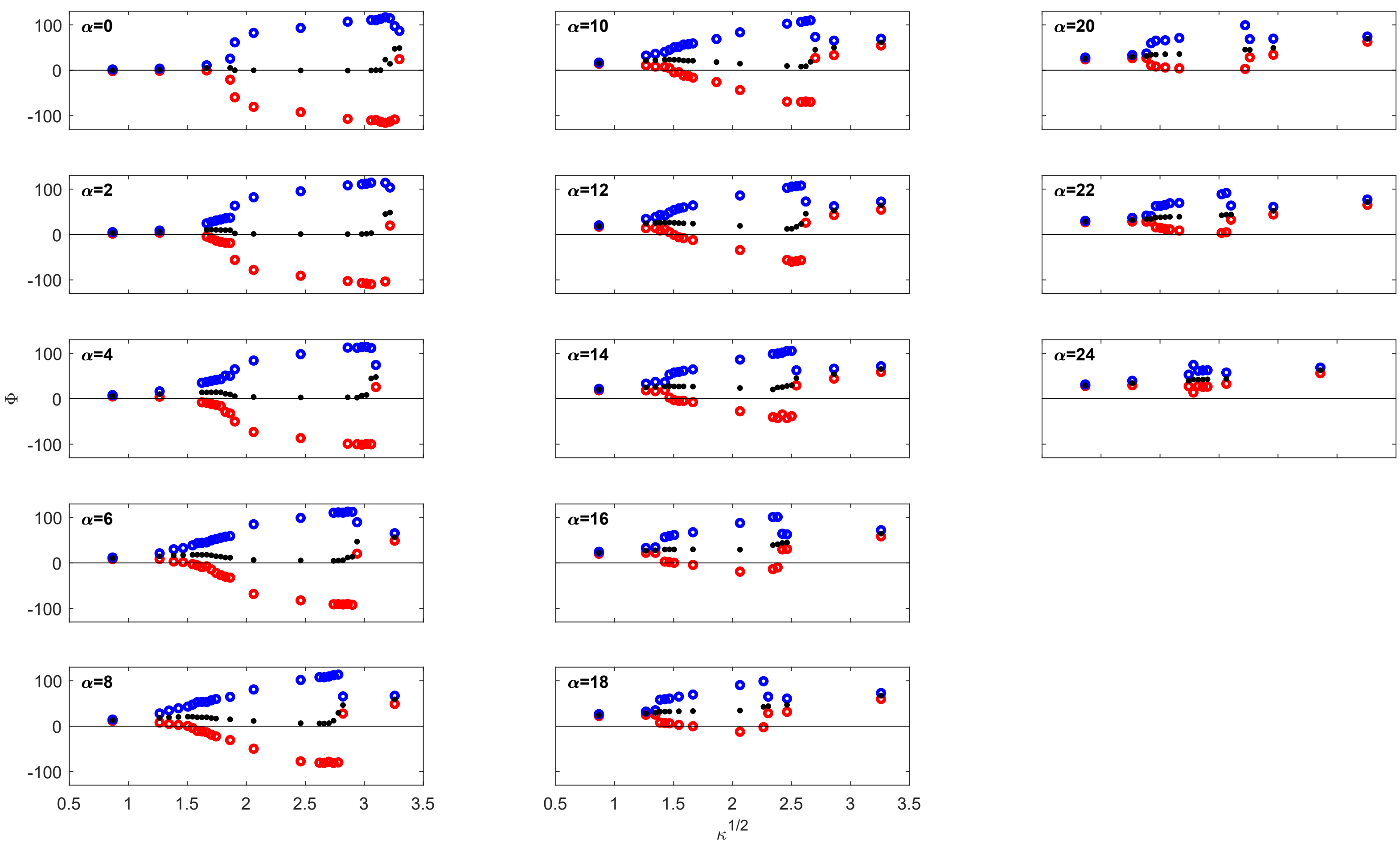

Figure A.1: Maximum (○), minimum (○) and mean (●) deflection angle, Φ, for an inverted flag of AR=2 and μ = 2.76 as a function of non-dimensional flow velocity, κ, and angle of attack, α

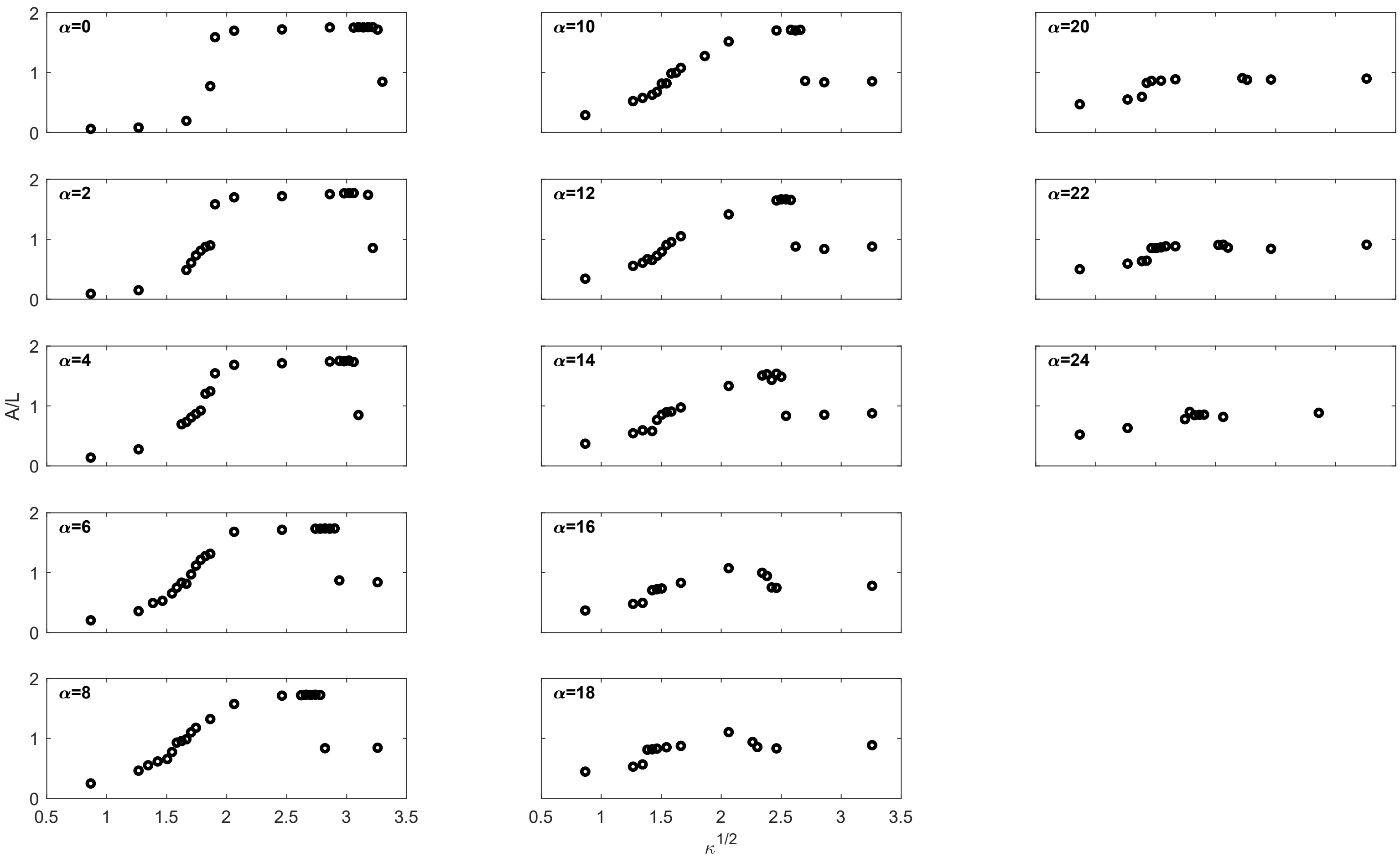

Figure A.2: Maximum cross section, A', for an inverted flag of AR=2 and $\mu = 2.76$ as a function of non-dimensional flow velocity, κ, and angle of attack, α

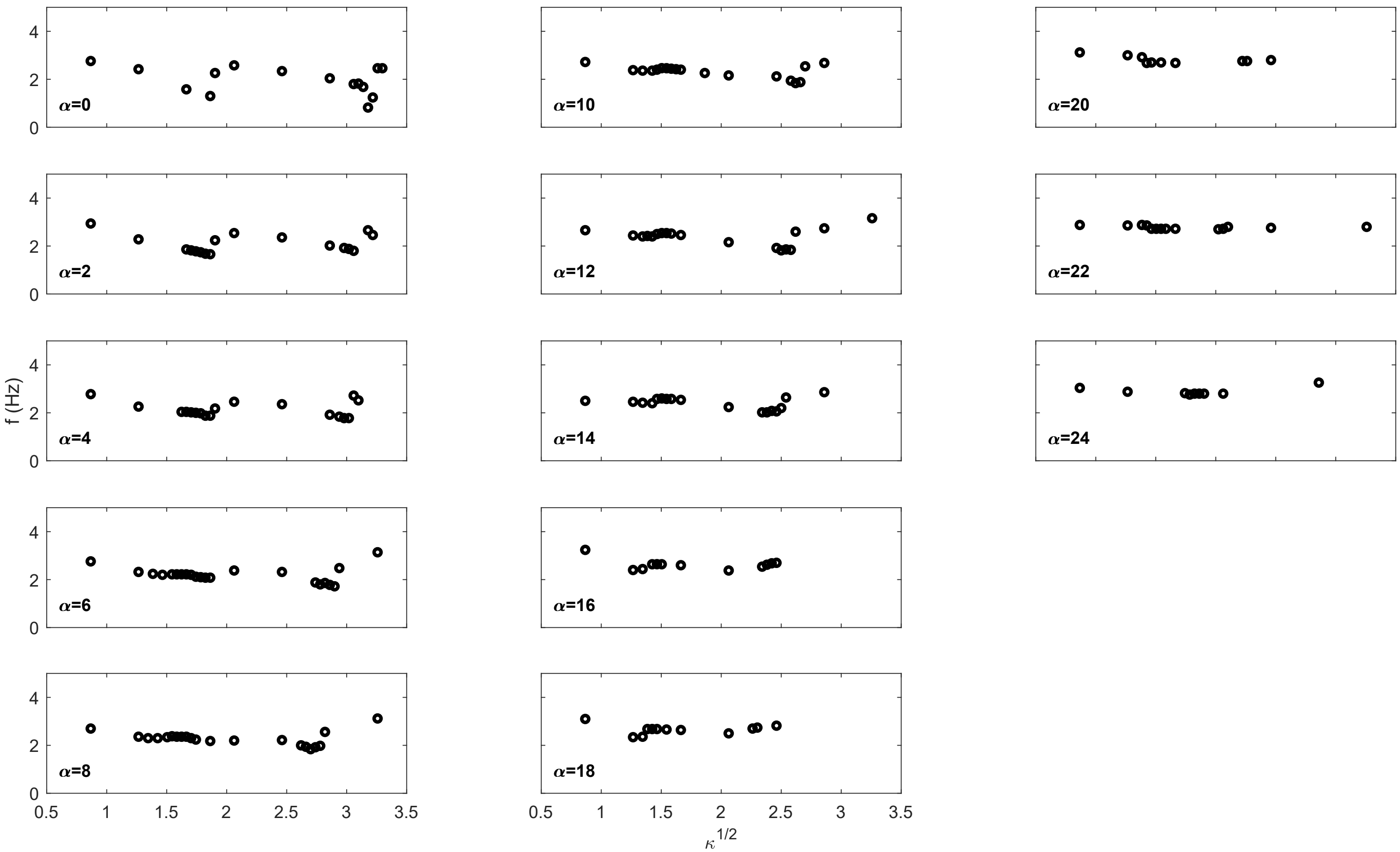

Figure A.3: Frequency of motion, f, for an inverted flag of AR=2 and $\mu = 2.76$ as a function of non-dimensional flow velocity, κ, and angle of attack, α

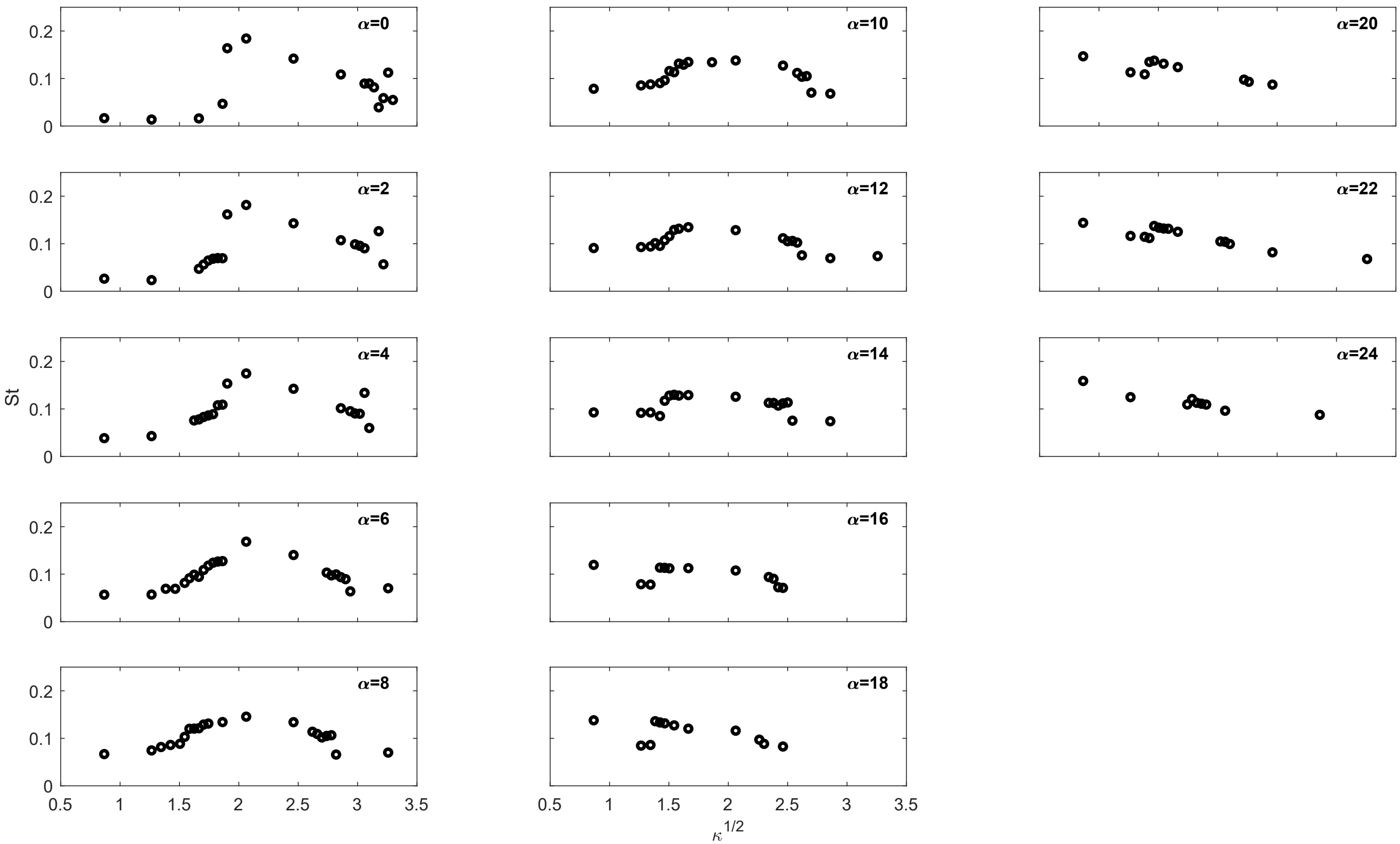

Figure A.4: Strouhal number, $St = fA'/U$, for an inverted flag of AR=2 and $\mu = 2.76$ as a function of non-dimensional flow velocity, κ, and angle of attack, α

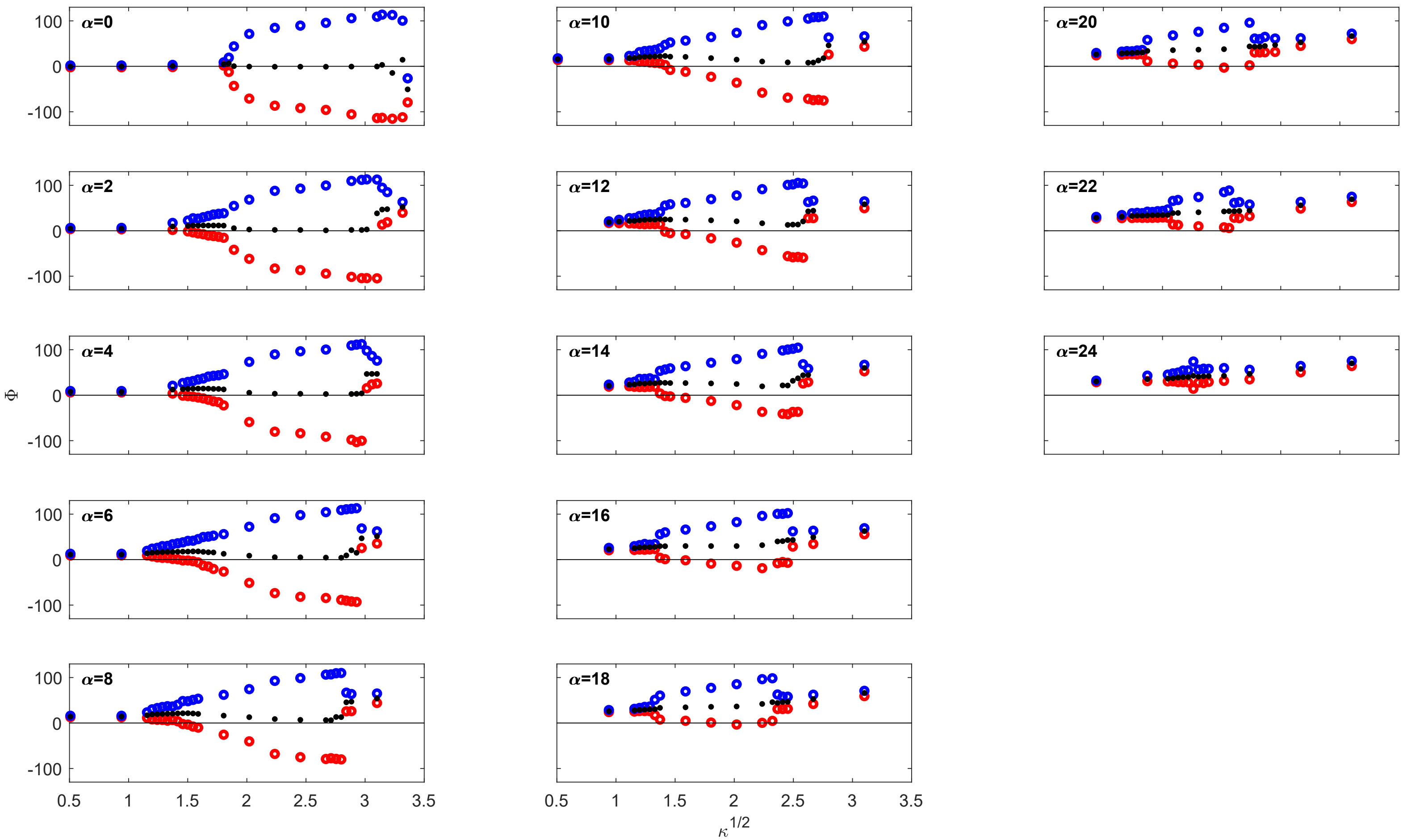

Figure A.5: Maximum (○), minimum (○) and mean (●) deflection angle, Φ, for an inverted flag of AR=2 and $\mu = 2.62$ as a function of non-dimensional flow velocity, κ, and angle of attack, α

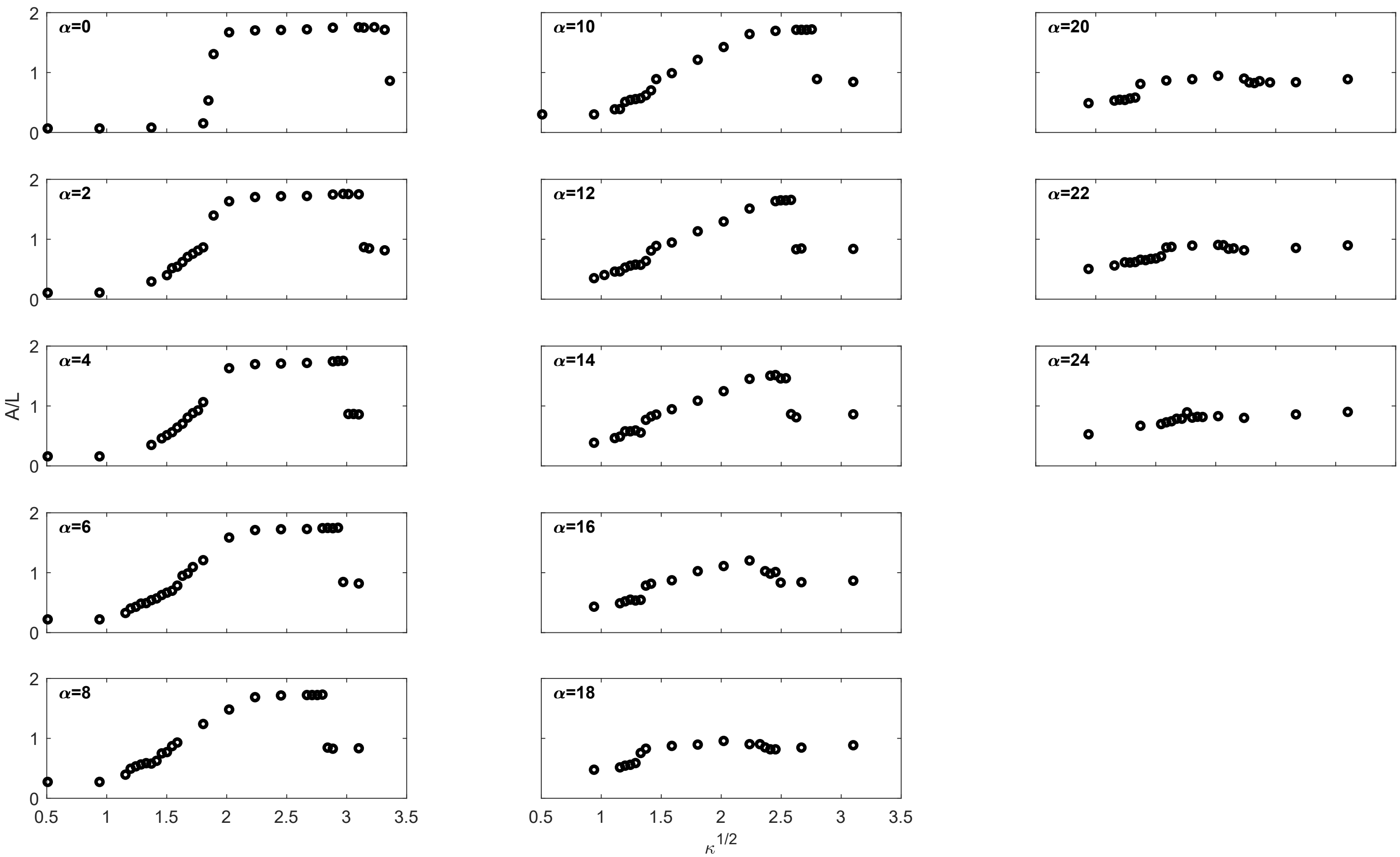

Figure A.6: Maximum cross section, A', for an inverted flag of AR=2 and $\mu = 2.62$ as a function of non-dimensional flow velocity, κ, and angle of attack, α

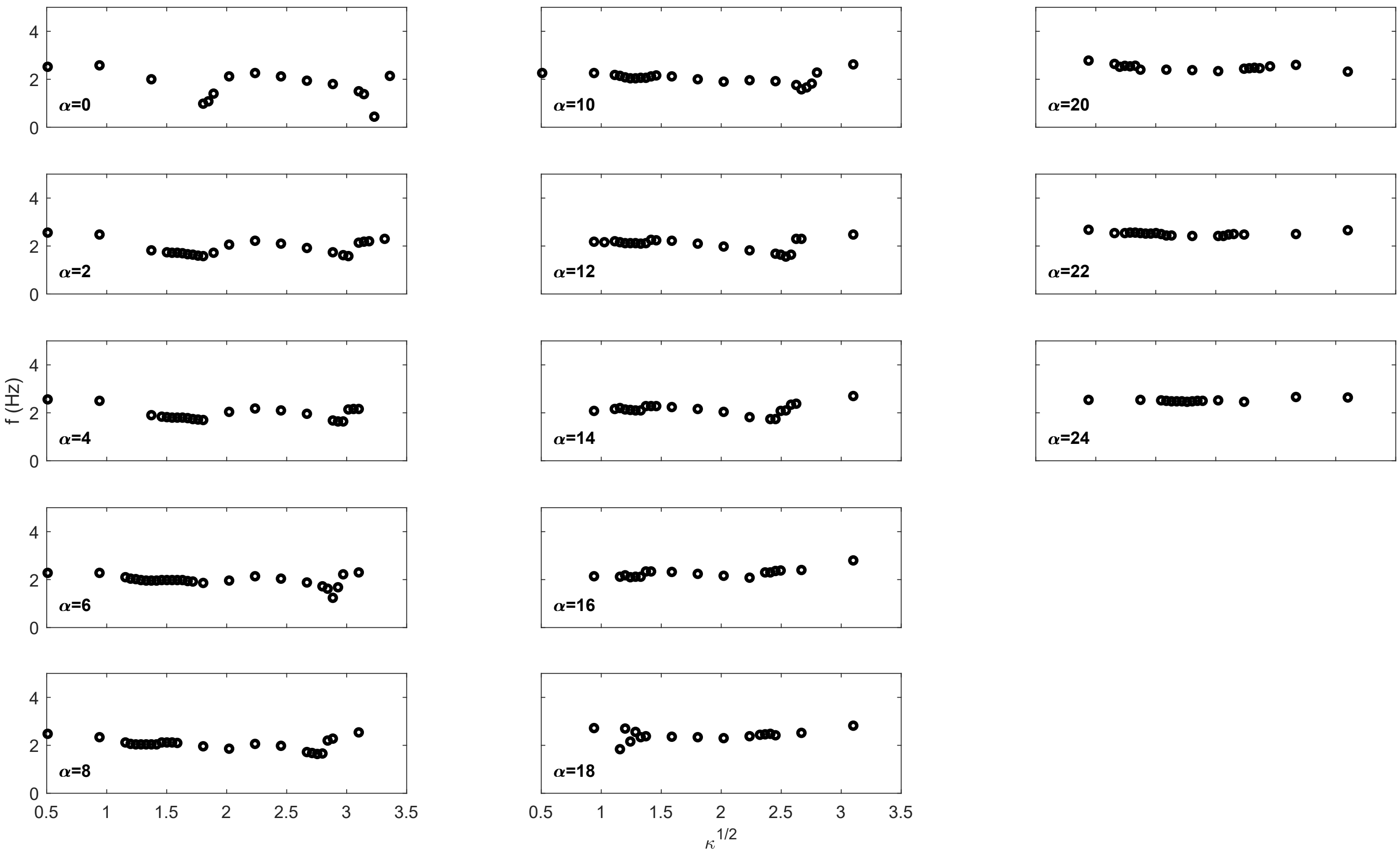

Figure A.7: Frequency of motion, f, for an inverted flag of AR=2 and $\mu = 2.62$ as a function of non-dimensional flow velocity, κ, and angle of attack, α

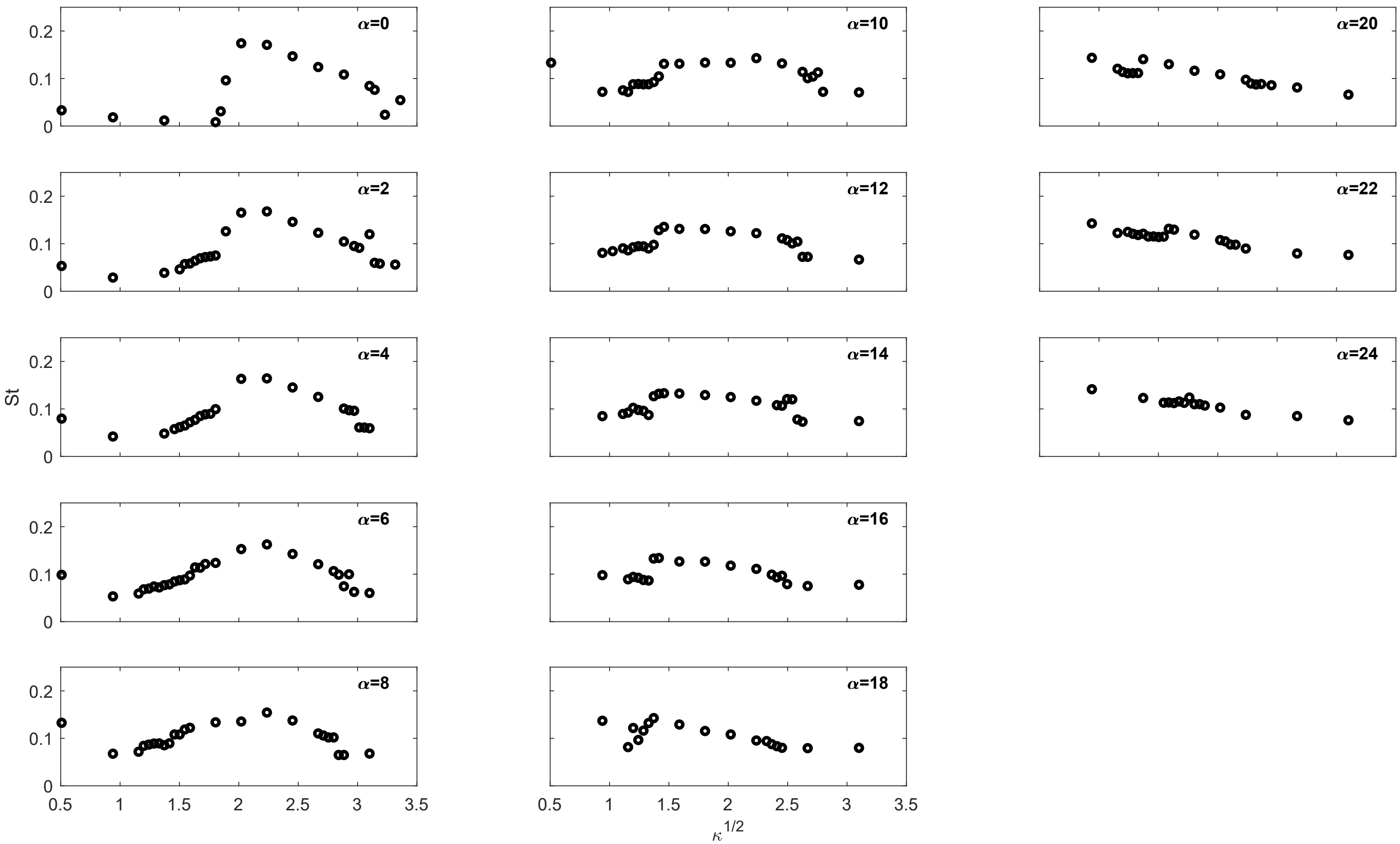

Figure A.8: Strouhal number, $St = fA'/U$, for an inverted flag of AR=2 and $\mu = 2.62$ as a function of non-dimensional flow velocity, κ, and angle of attack, α

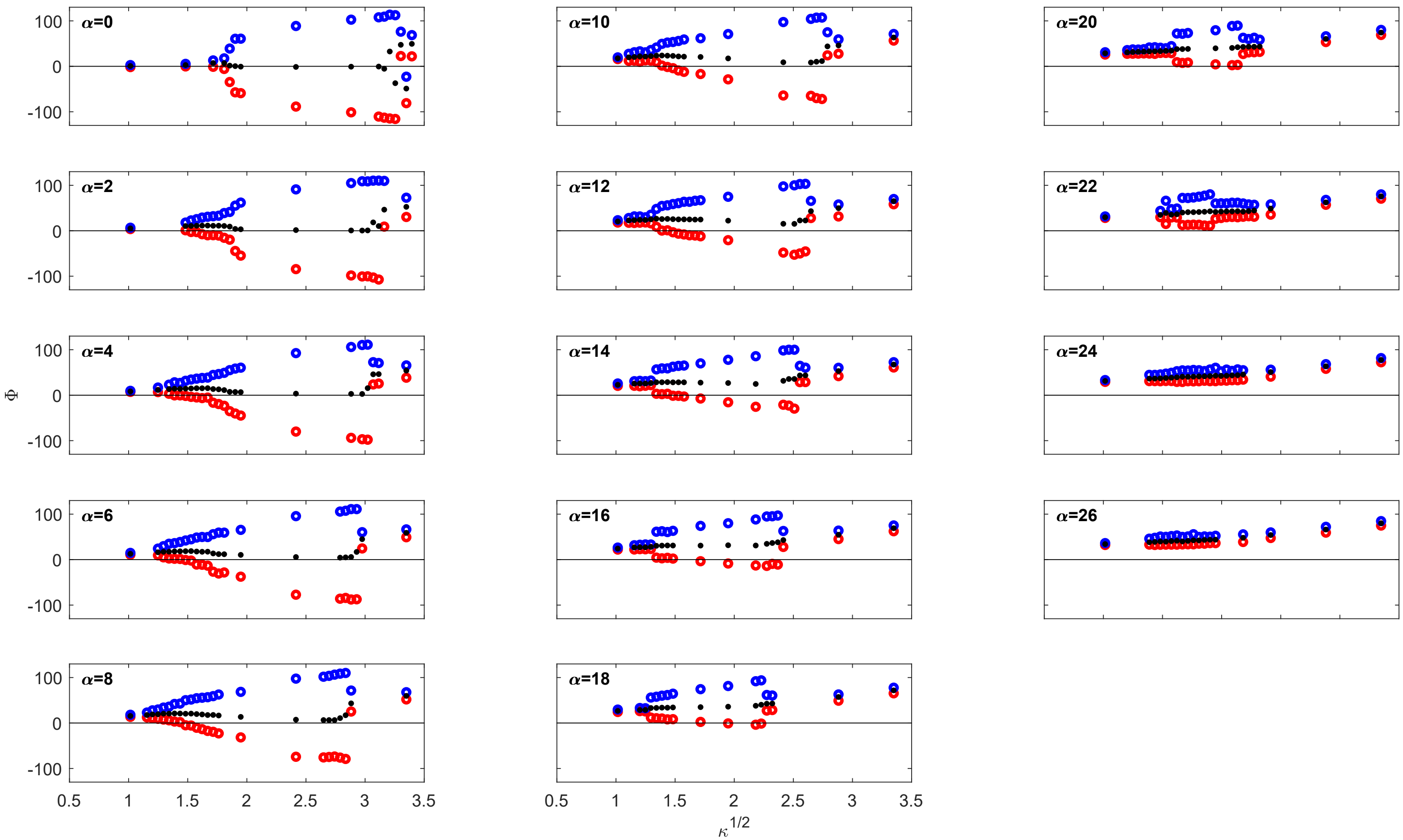

Figure A.9: Maximum ($\circ$), minimum ($\circ$) and mean ($\bullet$) deflection angle, Φ, for an inverted flag of AR=2 and $\mu = 2.49$ as a function of non-dimensional flow velocity, κ, and angle of attack, α

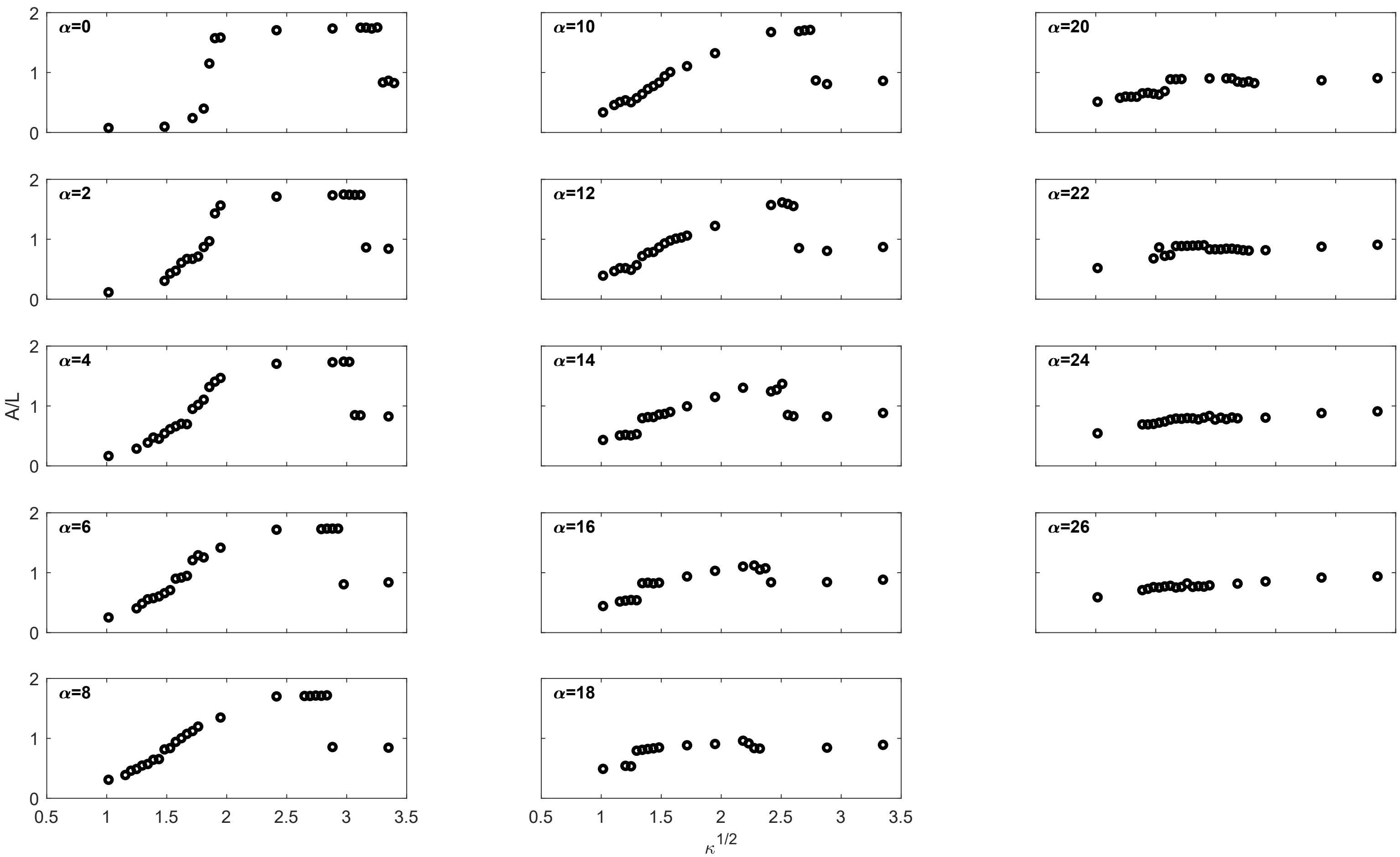

Figure A.10: Maximum cross section, A', for an inverted flag of AR=2 and μ = 2.49 as a function of non-dimensional flow velocity, κ, and angle of attack, α

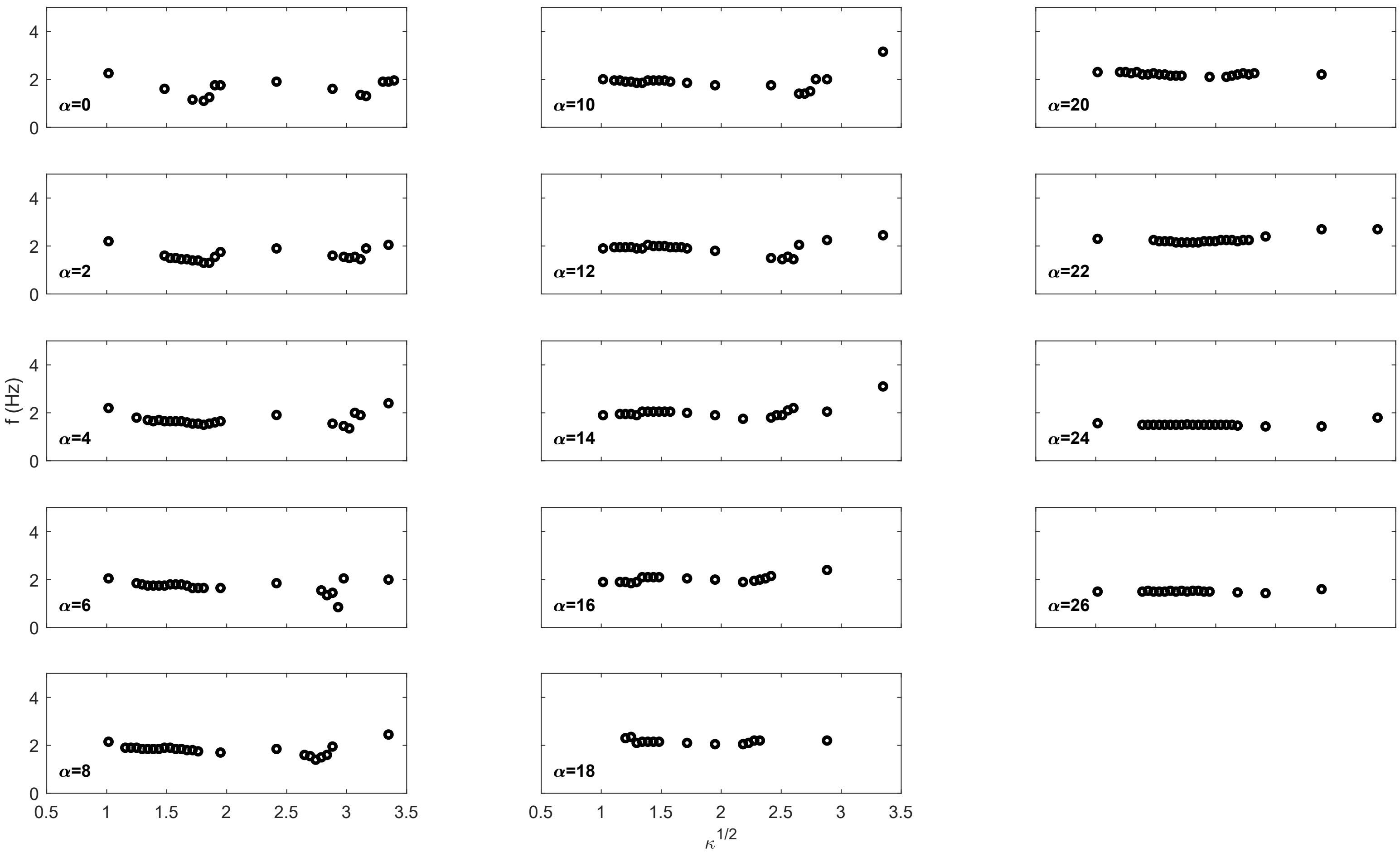

Figure A.11: Frequency of motion, f, for an inverted flag of AR=2 and $\mu = 2.49$ as a function of non-dimensional flow velocity, κ, and angle of attack, α

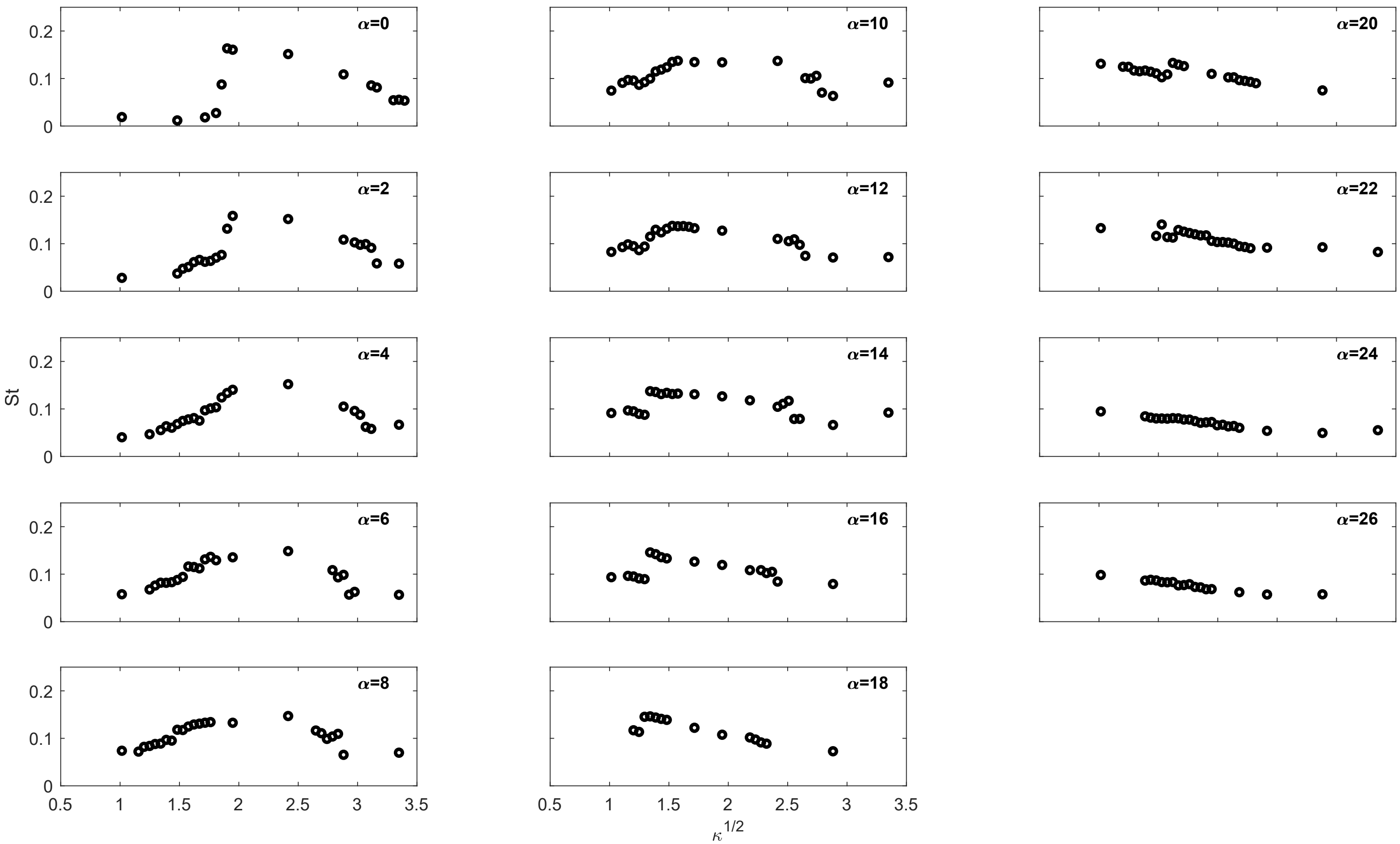

Figure A.12: Strouhal number, $St = fA'/U$, for an inverted flag of AR=2 and $\mu = 2.49$ as a function of non-dimensional flow velocity, κ, and angle of attack, α